

ZZ PRODUCTION IN PROTON-PROTON COLLISIONS AT
 $\sqrt{s} = 13$ TeV IN FOUR-LEPTON EVENTS USING THE
CMS DETECTOR AT THE CERN LHC

by

Nathaniel Woods

A dissertation submitted in partial fulfillment of
the requirements for the degree of

Doctor of Philosophy
(Physics)

at the
UNIVERSITY OF WISCONSIN – MADISON
2017

Defended on X October 2017

Dissertation approved by the following members of the Final Oral Committee:

Wesley Smith · Bjorn Wiik Professor of Physics
Sridhara Dasu · Professor of Physics
Matthew Herndon · Professor of Physics
Someone · Professor of Physics
Someone · Professor of Something

Abstract

Acknowledgements

Contents

Abstract	i
Acknowledgements	ii
Contents	iii
List of Figures	viii
List of Tables	xii
1 The Standard Model	1
1.1 Introduction	1
1.2 Matter and Force	2
1.3 Electroweak Symmetry Breaking and the Higgs Boson	8
1.4 Diboson and Multiboson Physics	11
1.4.1 Vector Boson Scattering	14
1.5 Limitations and Possible Extensions	15
1.5.1 Anomalous Gauge Couplings	16
1.6 Proton-Proton Collisions	18
1.7 Topics Covered In This Thesis	20
2 ZZ Phenomenology and Previous Results	21
2.1 Nonresonant ZZ/Z γ^* Production and Decay	22

2.1.1	Vector Boson Scattering	24
2.1.2	Prior Measurements	25
2.2	Resonant $ZZ^*/Z\gamma^*$ Production	28
2.2.1	Z Boson Decays to Four Leptons	29
2.2.2	Higgs Boson Production	29
2.2.2.1	Prior Measurements	30
2.3	Anomalous Gauge Couplings	32
2.3.1	Previous Limits	34
2.4	Background Processes	35
3	The CMS Experiment and the CERN LHC	37
3.1	The CERN Large Hadron Collider	38
3.1.1	Accelerator Chain, Layout, and Detectors	39
3.1.2	Operating Parameters	42
3.1.2.1	Design	43
3.1.2.2	Run I	44
3.1.2.3	Run II	45
3.2	The Compact Muon Solenoid Detector	46
3.2.1	Terminology and Geometry	48
3.2.2	Magnet and Inner Tracking System	49
3.2.2.1	Pixel Detector	51
3.2.2.2	Strip Tracker	52
3.2.3	Electromagnetic Calorimeter	52
3.2.4	Hadronic Calorimeter	54
3.2.5	Muon Spectrometer	56
3.2.5.1	Drift Tubes	58

3.2.5.2	Cathode Strip Chambers	58
3.2.5.3	Resistive Plate Chambers	60
3.2.6	Data Acquisition and Trigger	60
3.2.6.1	Level-1 Trigger	61
3.2.6.2	High-Level Trigger	63
3.2.7	Luminosity Determination	65
4	Simulation	67
4.1	Monte Carlo Event Generation	67
4.1.1	Matrix Element and Hard Process Generation	68
4.1.2	Parton Shower, Hadronization, and Underlying Event	69
4.1.3	Pileup Simulation	69
4.2	Detector Simulation	69
5	Object Reconstruction and Selection	70
5.1	Track Reconstruction and Vertex Identification	71
5.2	Particle Flow Reconstruction	73
5.2.1	PF Candidates	74
5.2.1.1	Muons	75
5.2.1.2	Electrons and Prompt Photons	75
5.2.1.3	Charged and Neutral Hadrons	76
5.2.2	Jets	76
5.2.3	Missing Transverse Energy	79
5.3	Object Identification and Selection	79
5.3.1	Electrons	80
5.3.2	Muons	82
5.3.3	Final State Photon Radiation	83

5.3.4	Jets	83
5.3.5	Misidentified Objects	84
5.4	ZZ Candidate and Event Selection	84
5.4.1	Z/γ^* Candidate Selection	86
5.4.2	ZZ Candidate Selection	86
5.4.3	Dijet and VBS Signal Selection	87
6	Analysis Strategy	88
6.1	Background Estimation	88
6.2	Systematic Uncertainties	91
6.3	Fiducial and Total Cross Section Calculation	93
6.3.1	Signal Strength Extraction	96
6.3.2	$Z \rightarrow 4\ell$ Branching Fraction	96
6.4	Differential Cross Sections	97
6.4.1	Unfolding	98
6.4.2	Uncertainties	99
6.5	VBS Signal Extraction	99
6.6	Anomalous Gauge Coupling Searches	101
7	Results	103
7.1	Four-Lepton Yield and Distributions	104
7.1.1	Full Spectrum	104
7.1.2	$Z \rightarrow 4\ell$ Resonance	104
7.1.3	Higgs Resonance	106
7.1.4	ZZ Production	107
7.2	ZZ Fiducial and Total Cross Section	111
7.2.1	$Z \rightarrow 4\ell$ Branching Fraction	115

7.3	Differential Cross Sections	119
7.4	Vector Boson Scattering	122
7.5	Anomalous Coupling Limits	122
8	Conclusions	140
8.1	Summary	140
8.2	Outlook	140
	Bibliography	141

List of Figures

1.1	Triple gauge boson coupling vertex	11
1.2	Quartic gauge boson coupling vertex	12
1.3	Higgs couplings to the gauge bosons	12
1.4	Higgs self couplings	13
1.5	Tree level Feynman diagrams for diboson production in fermion-anti-fermion collisions	14
1.6	Gluon-gluon fusion box diagram for general diboson production . . .	14
1.7	Unitarity violation in vector boson scattering without a Higgs boson	15
1.8	Neutral anomalous gauge coupling vertices	16
1.9	Neutral anomalous triple gauge coupling vertex	17
1.10	Parton distribution functions	19
2.1	Leading order $ZZ \rightarrow 4\ell$ production	23
2.2	Next-to-leading order $ZZ \rightarrow 4\ell$ production	23
2.3	Gluon-gluon fusion box diagram for $ZZ \rightarrow 4\ell$ production	24
2.4	Vector boson scattering diagrams	26
2.5	Feynman diagram for $Z \rightarrow 4\ell$ production	29
2.6	Higgs production mechanisms	31
2.7	Higgs boson SM cross section and branching ratio, as a function of m_H	32

2.8	Enhancements in p_T^Z and p_T^μ resulting from nonzero aTGCs	33
2.9	Lepton angular correlations resulting from nonzero aTGCs	34
2.10	Example background diagrams	36
3.1	LHC dipole schematic	40
3.2	LHC accelerator and experiment layout	41
3.3	Integrated luminosity delivered to CMS in each LHC run period . .	45
3.4	CMS cutout schematic	47
3.5	Inner tracker layout	50
3.6	Tracker material budget in radiation lengths	51
3.7	ECAL geometry	53
3.8	HCAL geometry	55
3.9	Total material budget in nuclear interaction lengths	56
3.10	Muon system geometry	57
3.11	Trigger data flow	64
6.1	Misidentification rates for electrons and muons	90
7.1	Full four-lepton mass spectrum	105
7.2	Mass of all Z/γ^* candidates in the full spectrum selection	106
7.3	Mass of Z_1 candidates in the full spectrum selection	107
7.4	Scatter plot of m_{Z_2} vs. m_{Z_1} for data events in the full spectrum selection	108
7.5	Four-lepton mass in the $Z \rightarrow 4\ell$ selection	109
7.6	Scatter plot of m_{Z_2} vs. m_{Z_1} for data events in the $Z \rightarrow 4\ell$ selection .	110
7.7	Four-lepton mass spectrum around the Higgs resonance	111
7.8	Mass of Z_1 candidates in events near the Higgs resonance	112
7.9	Mass of Z_2 candidates in events near the Higgs resonance	113
7.10	Scatter plot of m_{Z_2} vs. m_{Z_1} for data events near the Higgs resonance	114

7.11	Four-lepton mass spectrum for events with both Z candidates on-shell	115
7.12	Mass of all Z/γ^* candidates in the on-shell selection	116
7.13	Jet multiplicity	117
7.14	Transverse momentum of the leading and subleading jets	118
7.15	Pseudorapidity of the leading and subleading jets	118
7.16	Dijet invariant mass	119
7.17	Dijet pseudorapidity separation	120
7.18	Total ZZ cross section as a function of center-of-mass energy	121
7.19	Normalized differential ZZ cross section as a function of four-lepton invariant mass	123
7.20	Normalized differential ZZ cross section as a function of four-lepton system p_T	124
7.21	Normalized differential ZZ cross section as a function of Z boson candidate p_T	125
7.22	Normalized differential ZZ cross section as a function of leading lepton p_T	126
7.23	Normalized differential ZZ cross section as a function of ΔR between the Z bosons	127
7.24	Normalized differential ZZ cross section as a function of $\Delta\phi$ between the Z bosons	128
7.25	Normalized differential ZZ cross section as a function of jet multiplicity	129
7.26	Normalized differential ZZ cross section as a function of dijet invariant mass	130
7.27	Normalized differential ZZ cross section as a function of dijet pseudorapidity separation	131

7.28	Normalized differential ZZ cross sections as functions of leading and subleading jet transverse momentum	132
7.29	Normalized differential ZZ cross sections as functions of leading and subleading jet pseudorapidity	133
7.30	Normalized differential four-lepton cross section as a function of four-lepton invariant mass with loosened Z mass cuts	134
7.31	VBS signal extraction GBDT output	135
7.32	ZZ invariant mass distribution with example aTGC working points .	136
7.33	Asymptotic one- and two-dimensional aTGC limits at 95% confidence level	137
7.34	One-dimensional aTGC limits as a function of the maximum ZZ invariant mass used in the calculation	138
7.35	ZZ invariant mass distribution for dijet events, with example aQGC working points	139

List of Tables

1.1	Particle content of the standard model	3
3.1	LHC beam parameters	44
6.1	Systematic uncertainties on the total yield	93
6.2	Fiducial phase space definitions	95

7.1	Expected and observed yields for $Z \rightarrow 4\ell$ production.	105
7.2	Expected and observed yields for Higgs boson production.	108
7.3	Expected and observed yields for doubly-resonant ZZ production. . . .	110

0 Chapter 1

1 The Standard Model

2 1.1 Introduction

3 The standard model (SM) is a set of several related theories that together describe
4 matter and its interactions at a fundamental level. The SM is a remarkable theory,
5 making detailed predictions on a wide range of topics that have matched data within
6 the precision of essentially every experiment over roughly four decades. It is arguably
7 the best-confirmed theory in the history of science despite making some of the boldest,
8 broadest, and most precise predictions. There are a few known phenomena that the
9 SM does not cover, but it is generally believed to be self-consistent; future advances
10 will likely add to it, explain its free parameters, or find some deeper underlying
11 structure, not contradict it.

12 The following sections give a general overview of the SM and related topics that
13 serve as background material for the four-lepton processes described in more detail
14 in subsequent chapters. This includes discussions of the particle content of the SM
15 and the gauge structure that leads to particle interactions, the spontaneous symmetry
16 breaking mechanism that leads to the specific structure of the electroweak sector of the

17 SM, diboson processes, and the SM’s limitations and how they might be addressed.
 18 Some details are also given about the proton-proton interactions used to probe particle
 19 interactions at high energies. More complete information may be found in a number
 20 of texts, including Refs. [1–5]. Everything that follows uses units such that $c = \hbar = 1$,
 21 where c is the speed of light and \hbar is the reduced Planck’s constant $\hbar = h/2\pi$.

22 1.2 Matter and Force

23 In the SM, matter is made of fermions (particles with half-integer spin; all SM fun-
 24 damental fermions have spin $\frac{1}{2}$) which interact by exchanging gauge bosons (integer
 25 spin; spin 1 for the SM force carriers). Table 1.1 lists the fundamental particles and
 26 some of their properties. With the exception of the neutral bosons, all particles have
 27 a corresponding antiparticle which is the same except that all its quantum numbers
 28 have opposite sign. The fermions come in two categories, leptons and quarks. All the
 29 quarks and half the lepton types carry electric charge and are therefore subject to in-
 30 teractions through the electromagnetic force, described by quantum electrodynamics
 31 (QED). In a QED interaction, two charged particles exchange a photon, which carries
 32 the momentum transferred from one to the other. The photon is a spin-1 gauge boson
 33 that is massless and electrically neutral itself, explaining why electromagnetic forces
 34 are long-range.

35 There are six types of quarks which fall into three “generations:” up and down (u
 36 and d , first generation); charm and strange (c and s , second generation); and top and
 37 bottom (t and b)¹. Quark masses increase with each successive generation. Up-type
 38 quarks (u, c, t) have electric charge $+2/3$ (in units of the positron charge e) while
 39 down-type quarks have $-1/3$. Quarks are the building blocks of hadron, including

¹Top and bottom quarks are sometimes called truth and beauty by more romantic particle physicists.

Table 1.1: The particles of the standard model, and some of their properties. All fermions have a corresponding antiparticle with opposite sign for all quantum numbers. Quarks and leptons are grouped by generation. Note that the listed T^3 applies only to left-handed fermions; right-handed fermions have $T^3 = 0$ and do not couple to the W^\pm (right-handed neutrinos, if they exist, do not couple to the Z either).

Particle	Mass (GeV)	Charge (e)	T^3	Gauge couplings
Scalar boson (spin 0)				
H	125	0		W^\pm, Z
Fermion (spin 1/2)				
u	0.023	+2/3	+1/2	g, γ, Z, W^\pm
d	0.048	-1/3	-1/2	g, γ, Z, W^\pm
e	5.11×10^{-4}	-1	+1/2	γ, Z, W^\pm
ν_e	$< 2.2 \times 10^{-9}$	0	-1/2	Z, W^\pm
c	1.28	+2/3	+1/2	g, γ, Z, W^\pm
s	0.95	-1/3	-1/2	g, γ, Z, W^\pm
μ	0.105	-1	+1/2	γ, Z, W^\pm
ν_μ	$< 1.7 \times 10^{-4}$	0	-1/2	Z, W^\pm
t	172	+2/3	+1/2	g, γ, Z, W^\pm
b	4.2	-1/3	-1/2	g, γ, Z, W^\pm
τ	1.77	-1	+1/2	γ, Z, W^\pm
ν_τ	< 0.018	0	-1/2	Z, W^\pm
Vector boson (spin 1)				
g	0	0	0	g
γ	0	0	0	W^\pm
Z	91.2	0	0	W^\pm
W^\pm	80.4	± 1	± 1	γ, Z, W^\pm

40 $q\bar{q}'$ bound states called mesons and $qq'q''/\bar{q}\bar{q}'\bar{q}''$ bound states called baryons, of which
 41 protons (uud) and neutrons (udd) are the most familiar. Top quarks are too heavy to
 42 form bound states; they decay too quickly. Hadrons are bound by the strong nuclear
 43 force, described by the theory of quantum chromodynamics (QCD).

44 The mediator for the strong force is the gluon, which like the photon is a massless
 45 spin-1 gauge boson. The analog of electric charge is color charge, a notion originally
 46 introduced to explain how identical quarks could exist in the symmetric bound state
 47 of a hadron despite the Fermi exclusion principle [1]. Unlike electric charge, there
 48 are three types of color charge, typically called red, green, and blue, though these
 49 names are arbitrary². The analogy with color comes primarily from the heuristic
 50 that natural states must be “colorless,” i.e. a hadron may have equal parts color
 51 and corresponding anticolor as in a meson, but it may also be “white,” containing
 52 red, blue, and green in equal measures as in a baryon. This property, known as
 53 confinement, is why a free quark has never been observed, and is not expected to be
 54 found, and why the strong interaction is short-range even though gluons are massless.
 55 It is also why, for example, $qq\bar{q}$ bound states are not seen in nature.

56 Confinement arises from the structure of QCD interactions and gluons themselves.
 57 Among fermions, only quarks interact through the strong force, but gluons also carry
 58 color charge and interact with each other. Because gluons self-interact, have no
 59 distinct antiparticle, and are massless, they can split and radiate infinitely. The
 60 resulting soft gluon interactions around quarks lead to an anti-screening effect that
 61 causes the strength of the strong force to change as a function of the distance between
 62 interacting quarks, with close quarks interacting less strongly as far as a single gluon
 63 exchange is concerned. As quark separation gets larger, the potential energy of strong
 64 interactions rises rapidly, until it is energetically favorable for the gluon connecting

²Negative color charges are typically called antired, antigreen and antiblue, but sometimes cyan, magenta, and yellow, to continue the analogy with visible colors.

65 them to split into a $q\bar{q}$ pair that screens them and effectively breaks off the interaction.
66 A single colored particle will thus cause more colored particles to be produced from
67 vacuum until only colorless bound states remain, enforcing confinement. This process
68 is known as hadronization, and causes single quarks or gluons leaving a hard scattering
69 interaction to produce “jets” of many hadrons, each carrying a fraction of the original
70 parton momentum, that enter the detector in a conical shower. Conversely, close-
71 range QCD is relatively feeble, leading to “asymptotic freedom,” the property of
72 partons within hadrons that they may be considered independent in high-energy
73 collisions, because their interactions are weak enough that bound state effects may
74 be neglected (see Section 1.6).

75 Leptons may be electrically charged or neutral, and come in three generations,
76 each containing one lepton of each type, a charged lepton and a corresponding neu-
77 trino. In order of charged lepton mass, the generations are the electron and its
78 neutrino (e and ν_e), muon and its neutrino (μ and ν_μ), and tau and its neutrino (τ
79 and ν_τ). Taus decay quickly, with a mean lifetime of 2.9×10^{-13} s in their rest frame;
80 muons also decay, but their lifetime ($2.2 \mu\text{s}$) is long compared to other time scales in-
81 volved in particle collider experiments, so they are considered stable particles for the
82 purposes of this work. Neutrinos are known to have mass [6–8], and the masses are
83 known to be small but they have not been measured. All leptons and quarks interact
84 via the weak nuclear force, which is best known for causing the nuclear beta decay
85 reaction $n \rightarrow p + e^- + \bar{\nu}_e$. Neutrinos are notable for coupling to the rest of the SM only
86 through weak interactions, making them difficult to detect in practice. Detectors at
87 particle colliders make no attempt to detect neutrinos, and their involvement in the
88 process is inferred only through the apparent momentum imbalance resulting from
89 their absence.

90 The weak force operates through two mechanisms, charged-current and neutral-

91 current interactions. Neutral-current interactions proceed through exchange of a Z
 92 boson, an electrically neutral spin-1 mediator, and are analogous to electromagnetic
 93 interactions except for two important differences. Unlike the γ , the Z has mass—in
 94 fact, one of the largest known masses at 91 GeV—giving it longitudinal polarization
 95 modes and limiting the range of the force because it decays with a halflife on
 96 the order of 10^{-25} s. Also unlike QED, weak interactions do not respect parity (P)
 97 symmetry. The Z boson couples more strongly to left-handed fermions (those with
 98 helicity opposite their direction of motion) and right-handed antifermions than to
 99 their opposite-spin counterparts. The degree of asymmetry varies by fermion type;
 100 notably, the Z does not couple at all to right-handed neutrinos. Neutral-current in-
 101 teractions are still symmetric under combined charge conjugation and parity (CP)
 102 transformations.

103 Charged-current interaction proceed through exchange of an electrically charged
 104 boson, the W^\pm , which has a mass around 80 GeV. Leptons couple to W^- bosons in
 105 $\ell^-, \bar{\nu}_\ell$ pairs (W^+ bosons likewise with their antiparticles), causing μ and τ decays.
 106 Lepton flavor is conserved in the sense that charged leptons couple to the W only
 107 in conjunction with the (anti-)neutrino from the same generation, so the total lepton
 108 number $N_\ell = n_{\ell^-} - n_{\ell^+} + n_{\nu_\ell} - n_{\bar{\nu}_\ell}$, where n_X is the number of X particles in existence,
 109 is conserved separately for $\ell \in (e, \mu, \tau)$. Flavor conservation does not hold for quarks
 110 undergoing charged weak interactions. An up-type quark always couples to the W
 111 in conjunction with a down-type quark, as it must to obey conservation of electric
 112 and color charge. The pairings are in general described by a unitary 3×3 matrix
 113 known as the Cabibbo-Kobayashi-Maskawa (CKM) matrix which defines the inter-
 114 generational mixing. This mixing allows heavy quarks to decay to lighter ones, and
 115 is thus responsible for the decay of hadrons that do not contain the q̄q pair necessary
 116 for strong or electromagnetic decays.

117 Charged-current interactions also do not respect parity symmetry, and in fact are
 118 maximally parity violating: the W couples only to left-handed fermions and right-
 119 handed antifermions. Because neutrinos interact only through the weak force³, and
 120 the Z also couples only to left-handed neutrinos, this implies that it is not clear if
 121 right-handed neutrinos even exist. If they do, they have no way to interact with other
 122 matter and they are not part of the SM. Unlike neutral-current interactions, charged-
 123 current interactions violate CP symmetry. CP violation was first observed in neutral
 124 kaon mixing before the theory of the weak force was fully worked out [9]. After
 125 flavor-changing charged currents were formalized it was realized that CP violation
 126 could arise from a complex phase in the CKM matrix, which arises in models with at
 127 least three generations of quarks⁴ [10]. CP violation was subsequently confirmed by
 128 observation in a number of meson decays [11–16].

129 The quantum number analogous to electric charge and color charge for the weak
 130 interaction is the three-component weak isospin T^i , which is typically defined such
 131 that the measured component is T^3 . Left-handed fermions have $|T| = \frac{1}{2}$, the W^\pm
 132 has $|T| = \pm 1$, and all other particles have $|T| = 0$. Weak isospin is conserved in
 133 all electromagnetic, strong, and fermion-fermion weak interactions, but is not con-
 134 served in general. Electric charge is always conserved, and is related to the measured
 135 component of the weak isospin by the weak hypercharge Y , which is

$$Y = 2(Q - T^3), \quad (1.1)$$

136 where Q is the electric charge. This connection between the electromagnetic and
 137 weak forces, and the parallels between the weak neutral-current interaction and QED
 138 hint at the intriguing possibility that the two forces could be unified under a single

³Aside from gravity, presumably, but this interaction is not experimentally accessible and is not covered by the standard model.

⁴At the time, only the first two generations were known, so the observed CP asymmetry was taken as an early indication of the existence of top and bottom quarks.

139 theory, but important differences—in particular, boson mass—must be explained.
 140 The mechanism for this is called electroweak symmetry breaking.

141 **1.3 Electroweak Symmetry Breaking and the
 142 Higgs Boson**

143 The structures of the fundamental forces arise from symmetries in the underlying
 144 fields, specifically gauge invariance of the relevant terms in the SM Lagrangian. The
 145 full phenomenology of QCD, for example, arises from the $SU(3)$ symmetry of in-
 146 variance under local color phase transformations, and the fact the the symmetry is
 147 non-Abelian (i.e. the transformation operators do not commute). Charges are the
 148 generators of the relevant symmetry group, the conserved currents of Noether's first
 149 theorem [17]. A full treatment of the SM's symmetry group structure and its connec-
 150 tions to the theory's phenomenology is aesthetically pleasing but beyond the scope of
 151 an experimentalist's thesis. It is discussed in a number of books, including Refs. [2, 4,
 152 5, 18]. The relevant point here is that the weak force arises from an $SU(2)$ symmetry
 153 generated by the weak isospin T , and the electromagnetic force from a $U(1)$ sym-
 154 metry generated by the electric charge Q , so a unified electroweak force should obey
 155 an $SU(2)_L \times U(1)$ symmetry, where the L indicates that only left-handed fermions
 156 transform under the $SU(2)$ symmetry. The resulting unified electroweak theory is
 157 known as the Glashow-Weinberg-Salam (GWS) model [19–21].

158 An unbroken $SU(2)_L \times U(1)$ symmetry implies four massless vector gauge fields:
 159 a triplet $W_\mu^i (i \in 1, 2, 3)$ which couple to fields with weak isospin (but only for left-
 160 handed particles), and a singlet B_μ which couples to weak hypercharge currents. This
 161 looks like the weak and electromagnetic forces discussed above, except that the weak
 162 gauge fields are massless and all three weak bosons are maximally P-violating. The

163 gauge bosons can be given mass if the underlying symmetry is somehow broken in the
 164 theory's vacuum state. Symmetry breaking occurs via the Higgs mechanism⁵ [22–24],
 165 which introduces an isospin doublet of complex scalar fields

$$\phi = \begin{pmatrix} \phi^+ \\ \phi^0 \end{pmatrix}, \quad (1.2)$$

166 with a Lagrangian of the form

$$\mathcal{L}_H = (D_\mu \phi)^\dagger (D^\mu \phi) + \mu^2 \phi^\dagger \phi - \lambda^2 (\phi^\dagger \phi)^2 \quad (1.3)$$

167 where μ and λ are nonzero real numbers, D_μ is the covariant derivative invariant
 168 under $SU(2)_L \times U(1)_Y$,

$$D_\mu = \partial_\mu + igT_i W_\mu^i + i\frac{g'Y}{2}B_\mu, \quad (1.4)$$

169 and g and g' are the W_μ^i and B_μ coupling strengths. Because the potential in Eq. (1.3)
 170 is not minimized at 0, for small excitations around the vacuum expectation value
 171 (VEV) $v = \frac{\mu}{2\lambda} = 246$ GeV, in appropriately chosen coordinates, the doublet of com-
 172 plex scalar fields is reduced to

$$\phi = \frac{1}{\sqrt{2}} \begin{pmatrix} 0 \\ v + h(x) \end{pmatrix}. \quad (1.5)$$

173 Substituting Eq. (1.5) into Eq. (1.3) introduces mixing terms between the W_μ^i ,
 174 B_μ , and h fields. The new Lagrangian has mass eigenstates

$$\begin{aligned} W_\mu^\pm &= \frac{1}{\sqrt{2}} (W_\mu^1 \mp W_\mu^2) \\ Z_\mu &= \frac{gW_\mu^3 - g'B_\mu}{\sqrt{g^2 + g'^2}} = W_\mu^3 \cos \theta_W - B_\mu \sin \theta_W \\ A_\mu &= \frac{g'W_\mu^3 + gB_\mu}{\sqrt{g^2 + g'^2}} = W_\mu^3 \cos \theta_W + B_\mu \sin \theta_W \end{aligned} \quad (1.6)$$

⁵The Higgs mechanism is also called the Englert-Brout-Higgs-Guralnik-Hagen-Kibble mechanism to acknowledge more of the theorists who developed it, with Anderson and 't Hooft sometimes included as well.

175 where θ_W is the Weinberg electroweak mixing angle

$$\tan \theta_W = \frac{g'}{g}. \quad (1.7)$$

176 The newly defined fields are the gauge fields for the weak and electromagnetic forces,

177 with boson masses

$$\begin{aligned} m_W &= \frac{1}{2} v g \\ m_Z &= \frac{1}{2} v \sqrt{g^2 + g'^2} \\ m_A = m_\gamma &= 0. \end{aligned} \quad (1.8)$$

178 It is now clear that

$$\cos \theta_W = \frac{m_W}{m_Z}. \quad (1.9)$$

179 The original Higgs doublet in Eq. (1.2) had four degrees of freedom (two complex
180 scalars), of which only one remains in the final Higgs field $H = h - v$, which is now
181 a physical field with a corresponding massive scalar boson. The other three became
182 the longitudinal polarization modes of the vector bosons.

183 Electroweak symmetry breaking thus explains the observed structure of the elec-
184 tromagnetic and weak forces. Three bosons become massive, while one stays mass-
185 less. Because the photon is massless, the theory retains the $U(1)_{EM}$ gauge symmetry
186 observed in electromagnetic interactions and electric charge is conserved, while the
187 $SU(2)$ symmetry is broken and its generator T^i is not. The W^\pm bosons still couple
188 only to left-handed fermions, while the Z couples right- and left-handed fermions but
189 not equally. The nonzero VEV even gives a convenient mechanism for generation of
190 fermion masses in Yukawa couplings with Lagrangian terms of the form

$$\mathcal{L}_{m_f} = \sqrt{2} \frac{m_f}{v} (\bar{f}_L f_R + \bar{f}_R f_L). \quad (1.10)$$

191 It also controls off-diagonal terms in the Lagrangian that cause interactions between
192 the electroweak bosons, the primary focus of this research.

193 1.4 Diboson and Multiboson Physics

194 In addition to the previously discussed boson mass terms introduced into the SM
 195 Lagrangian by electroweak symmetry breaking, boson interaction terms appear for
 196 trilinear gauge boson couplings

$$\begin{aligned} \mathcal{L}_{WWV} = & -ig \left[(W_{\mu\nu}^+ W^{-\mu} - W^{+\mu} W_{\mu\nu}) (A^\nu \sin \theta_W - Z^\nu \cos \theta_W) \right. \\ & \left. + W_\nu^- W_\mu^+ (A^{\mu\nu} \sin \theta_W - Z^{\mu\nu} \cos \theta_W) \right], \end{aligned} \quad (1.11)$$

197 which results in the vertices shown in fig 1.1; quartic gauge couplings

$$\begin{aligned} \mathcal{L}_{WWVV} = & -\frac{g^2}{4} \left\{ \left[2W_\mu^+ W^{-\mu} + (A_\mu \sin \theta_W - Z_\mu \cos \theta_W)^2 \right]^2 \right. \\ & - [W_\mu^+ W_\nu^- + W_\nu^+ W_\mu^- \\ & \left. + (A_\mu \sin \theta_W - Z_\mu \cos \theta_W) (A_\nu \sin \theta_W - Z_\nu \cos \theta_W)]^2 \right\}, \end{aligned} \quad (1.12)$$

198 (Fig. 1.2); Higgs couplings to the massive vector bosons

$$\mathcal{L}_{HV} = \left(gm_W H + \frac{g^2}{4} H^2 \right) \left(W_\mu^+ W^{-\mu} + \frac{Z_\mu Z^\mu}{2 \cos^2 \theta_W} \right), \quad (1.13)$$

199 (Fig. 1.3); and Higgs self-interactions

$$\mathcal{L}_{HH} = -\frac{gm_H^2}{4m_W} H^3 - \frac{g^2 m_H^2}{32m_W^2} H^4, \quad (1.14)$$

200 (Fig. 1.4).

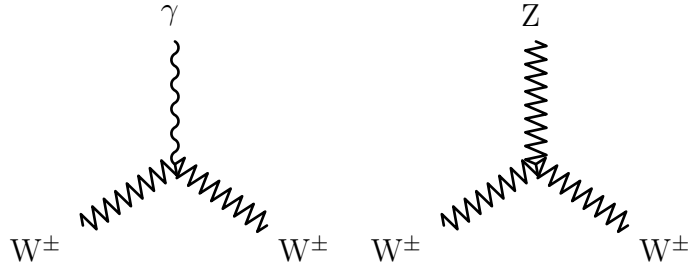


Figure 1.1: Vertex for the trilinear gauge boson couplings allowed at tree level in the SM.

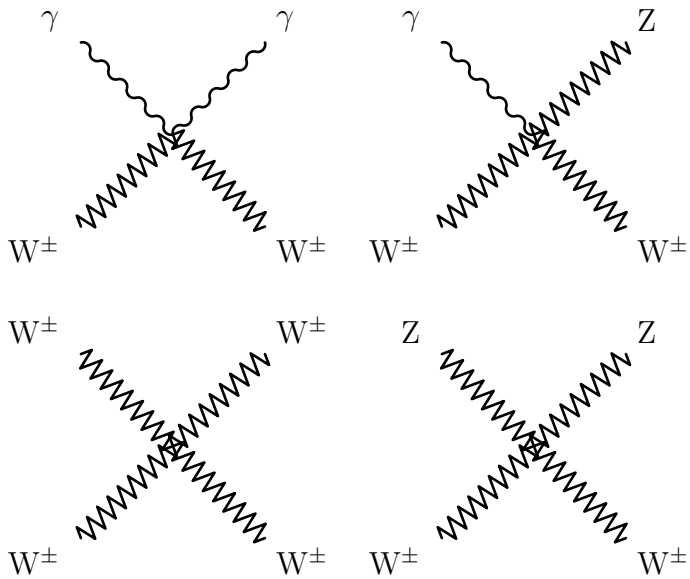


Figure 1.2: Vertices for the quartic gauge boson couplings allowed at tree level in the SM.

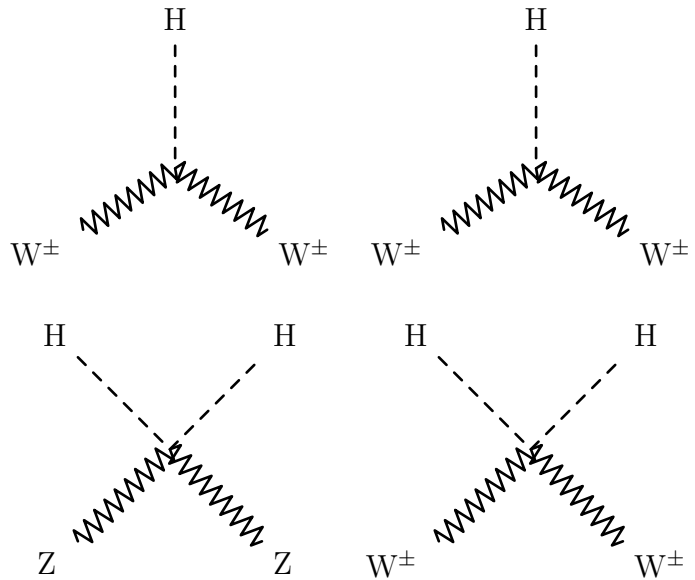


Figure 1.3: Vertices for Higgs boson couplings to gauge bosons allowed at tree level in the SM.

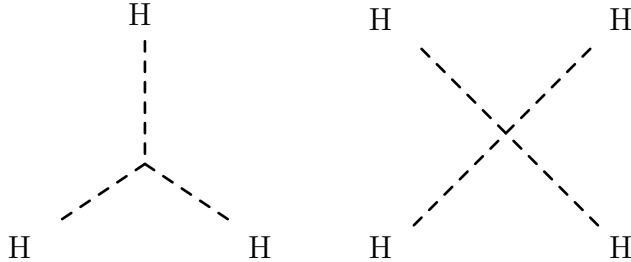


Figure 1.4: Higgs boson trilinear and quartic self-coupling vertices.

201 The structure of the interactions shown in Figs. 1.1–1.4 depends on the details
 202 of the GWS model and spontaneous symmetry breaking, making multiboson interac-
 203 tions excellent probes of the SM electroweak and Higgs sectors. One can confirm the
 204 basic validity of the Higgs mechanism by observation of a Higgs boson, and its inter-
 205 actions with the massive gauge bosons can be probed in decays to ZZ^* and $W^\pm W^\mp$,
 206 which were in fact used in its discovery (see Section 2.2.2.1). The SM makes a num-
 207 ber of other testable predictions about the behavior of the electroweak bosons, the
 208 most easily testable of which are the multiboson production cross sections, i.e. the
 209 rates at which particle collisions result in final states with two or more electroweak
 210 gauge bosons. The tree-level diagrams for general diboson production in fermion-
 211 antifermion collisions ($ff \rightarrow VV$) are shown in Fig. 1.5. The cross section for such
 212 a process will be strongly dependent on the gauge bosons' couplings to fermions, in
 213 the first diagram in Fig. 1.5, and their couplings to other gauge bosons in the second
 214 (which does not contribute at all for neutral gauge bosons in the SM). Diboson pro-
 215 duction in gg collisions does not occur at tree level but may proceed through a quark
 216 loop as in the so-called box diagram of Fig. 1.6.

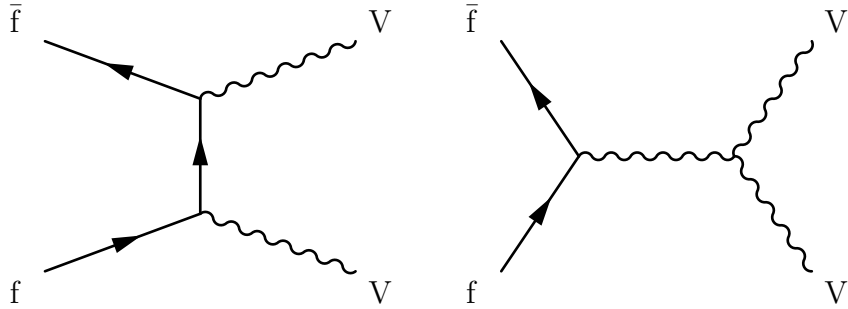


Figure 1.5: Tree-level Feynman diagrams for diboson production in fermion-anti-fermion collisions. The second diagram does not contribute for neutral gauge bosons in the SM.

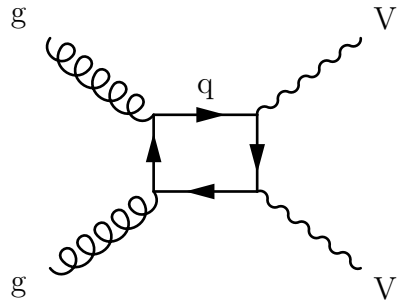


Figure 1.6: Leading order ‘box’ diagram for diboson production through a quark loop in a gluon-gluon fusion event.

²¹⁷ 1.4.1 Vector Boson Scattering

²¹⁸ Quasielastic vector boson scattering (VBS) interactions ($VV \rightarrow VV$) are sensitive
²¹⁹ to a number of features of the SM electroweak sector. If only the vector bosons
²²⁰ are considered, the scattering amplitude for the process grows quadratically with the
²²¹ center-of-mass energy, violating unitarity [25]. The addition of diagrams involving the
²²² Higgs boson enter with opposite sign and restore unitarity, as shown in Fig. 1.7. The
²²³ VBS cross section is therefore sensitive to both the four-point gauge boson couplings
²²⁴ of Fig. 1.2 and the structure of the Higgs field, and can be used to distinguish the
²²⁵ SM from models without a Higgs boson and models with multiple particles that play
²²⁶ its role.

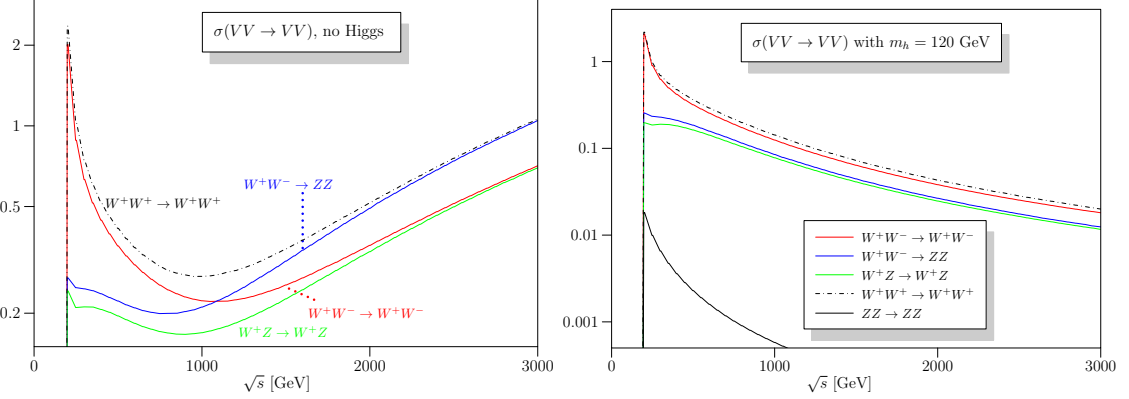


Figure 1.7: $VV \rightarrow VV$ scattering cross sections as a function of center-of-mass energy for the SM with no Higgs boson (left) and a Higgs boson with $m_H = 120$ GeV (right), reproduced from Ref. [25]. The model with no Higgs violates unitarity.

227 1.5 Limitations and Possible Extensions

228 As noted above, the SM is believed to be fully self-consistent, but it has several notable
 229 omissions. It makes no mention of gravity, which is too weak to be probed at the level
 230 of individual particles at energies available in today’s collider experiments—or any
 231 collider experiment in the foreseeable future. Neutrinos in the SM are massless, but
 232 they are found experimentally to oscillate between the three flavors in flight, which
 233 implies that the flavor eigenstates are not mass eigenstates, and thus that they have
 234 mass. Dark matter is also not described. Some consider the SM to be “ad hoc” in
 235 the sense that the fermion masses, and a number of other parameters—19 in all—
 236 are completely unconstrained, and a more aesthetically satisfying theory would make
 237 predictions for all of them.

238 A number of theories have been proposed which modify or extend the SM, adding
 239 new symmetry groups, unifying the existing ones further, adding new particles, etc.
 240 A fourth generation of fermions would be a simple extension, but the fourth neutrino
 241 would have to have a mass more than half the Z boson mass to have escaped detection
 242 so far, which would be surprising given the small masses of the first three. Super-

243 symmetric models, for example, posit a symmetry between bosons and fermions, such
 244 that each particle would have a “superpartner” with the opposite spin statistics. De-
 245 spite extensive searches, no evidence of such models has been found. Another simple
 246 extension would be a new force, with mediator gauge bosons analogous to the W and
 247 Z above the masses accessible at existing colliders. This, and several other possible
 248 extensions to the SM, would appear in practice as small deviations from the expected
 249 couplings of the gauge bosons.

250 1.5.1 Anomalous Gauge Couplings

251 Such deviations from standard model interactions are called anomalous gauge cou-
 252 plings (aGC), and may involve anomalous trilinear (aTGC) or quartic (aQGC) ver-
 253 tices. Of particular interest here are the anomalous neutral couplings, which corre-
 254 spond to the vertices shown in Fig. 1.8. These interactions are forbidden in the SM.
 255 Their existence would increase the cross section for diboson production, and affect
 256 the cross section for $ZZ \rightarrow ZZ$ scattering, changing the requirements on the Higgs
 257 field needed to preserve unitarity.

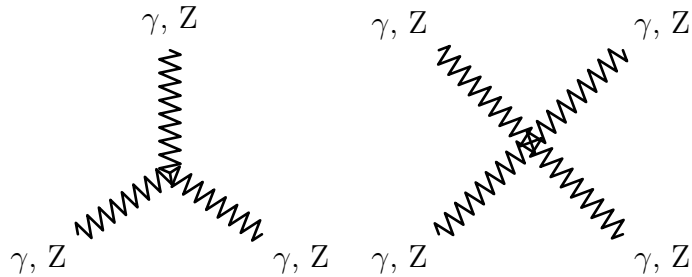


Figure 1.8: Fully-neutral gauge coupling vertices, for aTGCs (left) and aQGCs (right). These are forbidden in the SM.

258 Several theoretical frameworks exist for describing aGCs. For aTGCs, we use the
 259 effective Lagrangian approach described in Ref. [26–28]. In this parameterization, a
 260 ZZV coupling (where V may be Z or γ) has a vertex function corresponding to the

261 vertex shown in Fig. 1.9 of the form

$$\Gamma_V^{\alpha,\beta,\delta}(q_1, q_2, P) = i \frac{\hat{s} - m_V^2}{m_Z^2} (f_4^V (P^\alpha g^{\delta\beta} + P^\beta g^{\delta\alpha}) + f_5^V \varepsilon^{\delta\alpha\beta\lambda} (q_1 - q_2)_\lambda), \quad (1.15)$$

262 where \hat{s} is the center of mass energy squared, $g^{\mu\nu}$ is the Minkowski metric and $\varepsilon^{\alpha\beta\gamma\delta}$ is
263 the fully antisymmetric tensor with $\varepsilon^{0123} = 1$. Neutral aTGCs are then described by
264 two parameters $f_4^{\gamma,Z}$ associated to CP-odd terms and two parameters $f_5^{\gamma,Z}$ associated
265 to CP-even terms.⁶ The effective Lagrangians in use here are taken to be low-energy
266 approximations invalid had high energy, and are not unitary at high $\sqrt{\hat{s}}$. In some
267 previous literature, unitarity is enforced with a generalized dipole form factor [28, 29],
268 such that the vertex factor takes an energy dependence,

$$f_i^V(\hat{s}) = \frac{f_{i,0}^V}{(1 + \hat{s}/\Lambda^2)^n}, \quad (1.16)$$

269 where Λ is the energy scale of the new physics process. No such form factor is applied
270 in this work, to avoid adding unnecessary model dependence, so Λ is taken to be much
271 larger than the energies accessible in the experiment and no form factor is applied.

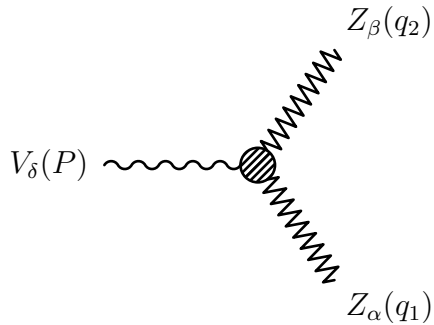


Figure 1.9: An anomalous neutral triple gauge coupling vertex, with momentum labels corresponding to Eq. (1.15).

272 For aQGCs, we adopt an effective field theory approach [30] which parameterizes
273 the effects of new physics as a set of field operators [31]. The operators are chosen to

⁶There are, of course, analogous terms for all anomalous VVV couplings, where V may be any of the electroweak bosons, but only the ZZZ and ZZ γ terms are relevant to this work.

274 be dimension-8, because this is the lowest dimension that can yield neutral quartic
 275 couplings, and the lowest dimension that can produce a theory with aQGCs but no
 276 aTGCs. Out of the large class of operators which control aQGCs in general, ZZ VBS
 277 is sensitive to five,

$$\begin{aligned}\mathcal{L}_{T0} &= \frac{f_{T0}}{\Lambda^4} \text{Tr} \left[\hat{W}_{\mu\nu} \hat{W}^{\mu\nu} \right] \times \text{Tr} \left[\hat{W}_{\alpha\beta} \hat{W}^{\alpha\beta} \right] \\ \mathcal{L}_{T1} &= \frac{f_{T1}}{\Lambda^4} \text{Tr} \left[\hat{W}_{\alpha\nu} \hat{W}^{\mu\beta} \right] \times \text{Tr} \left[\hat{W}_{\mu\beta} \hat{W}^{\alpha\nu} \right] \\ \mathcal{L}_{T2} &= \frac{f_{T2}}{\Lambda^4} \text{Tr} \left[\hat{W}_{\alpha\mu} \hat{W}^{\mu\beta} \right] \times \text{Tr} \left[\hat{W}_{\beta\nu} \hat{W}^{\nu\alpha} \right] \\ \mathcal{L}_{T8} &= \frac{f_{T8}}{\Lambda^4} B_{\mu\nu} B^{\mu\nu} B_{\alpha\beta} B^{\alpha\beta} \\ \mathcal{L}_{T9} &= \frac{f_{T9}}{\Lambda^4} B_{\alpha\mu} B^{\mu\beta} B_{\beta\nu} B^{\nu\alpha},\end{aligned}\tag{1.17}$$

278 where

$$\hat{W}_{\mu\nu} = \sum_j W_{\mu\nu}^j \frac{\sigma^j}{2},\tag{1.18}$$

279 and $\Lambda \gg \sqrt{\hat{s}}$ is again the scale of the new physics causing the change in the effective
 280 couplings.

281 1.6 Proton-Proton Collisions

282 Our experimental probe of all these interactions is proton-proton collisions. As dis-
 283 cussed above, protons are bound states of three quarks (uud), known as the valence
 284 quarks, held together by virtual gluon exchange. The proton constituents, quarks and
 285 gluons, are collectively called partons. The gluons carry roughly half the total proton
 286 momentum [2]. Because the number of gluons is not conserved, and they self-interact,
 287 the gluon structure of the proton is constantly evolving, and gluons produce virtual
 288 q \bar{q} “sea quark” pairs which annihilate again on time scales of order $t_{virt} \sim 1/\Delta E$ [3].
 289 A sufficiently energetic color-charged particle colliding with a proton may therefore

290 interact with any kind of quark or with a gluon, and interesting physics in a pp col-
 291 lision may be initiated by $q\bar{q}$, $q\bar{q}$, qg , or gg scattering. A particle that scatters with
 292 a proton of energy P has a probability of interacting with a parton of a given type
 293 with momentum xP given by the parton distribution function (PDF) $f(x, Q^2)$, where
 294 Q is the momentum transfer of the interaction. Heuristically, the PDF is a function
 295 of Q because it sets the wavelength of the mediating gauge boson and thus the scale
 296 on which the interaction can resolve constituent partons. PDFs are nonperturbative
 297 and cannot be calculated from theory, and are built from fits to experimental data
 298 from fixed-target and symmetric $e^\pm p$ deep inelastic scattering (DIS) data, and from
 299 hadron collider data [32]. The most recent PDFs from the NNPDF collaboration are
 300 shown in Fig 1.10.

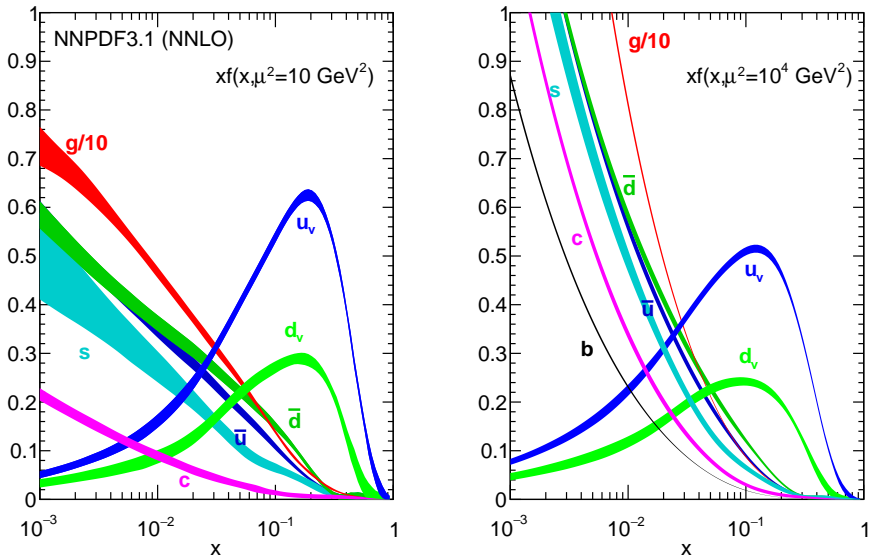


Figure 1.10: Parton distribution functions from NNPDF3.1, reproduced from Ref. [32], which used μ for the momentum transfer denoted Q in the text.

301 As mentioned previously, the rate at which a scattering process occurs is called its
 302 cross section σ , typically given in barns, a unit of area $b = 10^{-24} \text{ cm}^2$. The number

303 of collisions is characterized by the luminosity \mathcal{L} such that the rate of events with
 304 final state X will be given by

$$\frac{dN_X}{dt} = \sigma(pp \rightarrow X) \mathcal{L} \quad (1.19)$$

305 as described in more detail in Section 3.1. If the initial protons each have momen-
 306 tum P and collide head on, such that their center-of-mass energy is $\sqrt{s} = 2P$, the
 307 interacting partons will have total energy $\sqrt{\hat{s}} = \sqrt{2x_1x_2}P$ where x_1 and x_2 are the
 308 fraction of its proton's momentum each incoming parton carried. The cross section
 309 is given by

$$\sigma(pp \rightarrow X) = \sum_{p_1, p_2 \in q, \bar{q}, g} C_{p_1, p_2} \int dx_1 dx_2 f_{p_1}(x_1, Q^2) f_{p_2}(x_2, Q^2) \sigma_{\text{ME}}(p_1 + p_2 \rightarrow X), \quad (1.20)$$

310 where σ_{ME} is the matrix-level cross section for the bare partons to scatter
 311 to final state X and C_{p_1, p_2} is a combinatoric factor based on the number of possible
 312 color combinations that varies based on the initial state particles p_1 and p_2 . This
 313 factorization into perturbative hard process physics and the nonperturbative PDF
 314 greatly simplifies calculations.

315 1.7 Topics Covered In This Thesis

₀ Chapter 2

₁ ZZ Phenomenology and Previous ₂ Results

₃ Four-lepton final states originate primarily from three physics processes: nonresonant
 ₄ diboson production, resonant Higgs boson production, and resonant single-Z produc-
 ₅ tion. Multi-Z triboson production (WZZ and ZZZ) occurs at negligible rates [33, 34].
 ₆ Single-Z triboson production (WWZ) [34, 35] and $t\bar{t}Z$ production result in final states
 ₇ with four prompt leptons, but are considered background (see Section 2.4). The three
 ₈ signal processes can be distinguished by kinematics, but all involve the Z boson.

₉ The Z was first observed in 1973 when the Gargamelle bubble chamber experi-
 ₁₀ ment at CERN recorded an elastic muon antineutrino-electron ($\bar{\nu}_\mu + e^- \rightarrow \bar{\nu}_\mu + e^-$)
 ₁₁ scattering event [36]. Direct observation in leptonic decays came roughly a decade
 ₁₂ later, from the UA1 experiment, also at CERN [37]. Clean e^+e^- collisions at LEP and
 ₁₃ SLAC, where the center-of-mass energy could be adjusted to produce Z bosons copi-
 ₁₄ ously, allowed its properties—and a number of other parameters of the electroweak
 ₁₅ theory—to be measured with per-mille precision or better [38]. Of particular impor-

16 tance to this study, the Z mass is

$$m_Z = 91.1876 \pm 0.0021 \text{ GeV}, \quad (2.1)$$

17 its full width is

$$\Gamma_Z = 2.4952 \pm 0.0023 \text{ GeV}, \quad (2.2)$$

18 its width in leptonic decays is

$$\Gamma_Z(\ell^+ \ell^-) = 83.984 \pm 0.086 \text{ MeV}, \quad (2.3)$$

19 and it decays to a pair of charged leptons 3.3658% of the time for each lepton fla-
20 vor [39].

21 **2.1 Nonresonant ZZ/Z γ^* Production and Decay**

22 Leading-order ZZ production is q \bar{q} -initiated and proceeds through t -channel quark
23 exchange, as shown in Fig. 2.1. At next-to-leading order (NLO; several representative
24 diagrams are shown in Fig. 2.2), may have a gluon in the initial state and may have
25 a quark or gluon in the final state which hadronizes and appears experimentally as
26 a jet. Next-to-next-to-leading order (NNLO) adds gluon-gluon fusion box diagrams
27 (Fig. 2.3), as well as q \bar{q} -initiated production with two loops, one loop and a final
28 state jet, and two jets. The NNLO corrections are generally large, outside the scale
29 uncertainties of the NLO calculation, because the gluon-fusion diagrams contribute
30 only positively to the cross section because of their distinct initial state, and have
31 a large amplitude—roughly 60% of the total NNLO correction—due to the high
32 effective gluon luminosity in multi-TeV proton collisions [40]. Because of the box
33 diagrams’ large contribution, “NLO + gg” simulations are often used, in which NLO
34 q \bar{q} /qg/ $\bar{q}g \rightarrow ZZ$ and LO gg $\rightarrow ZZ$ samples are summed even though they formally
35 contribute at different orders in α_s .

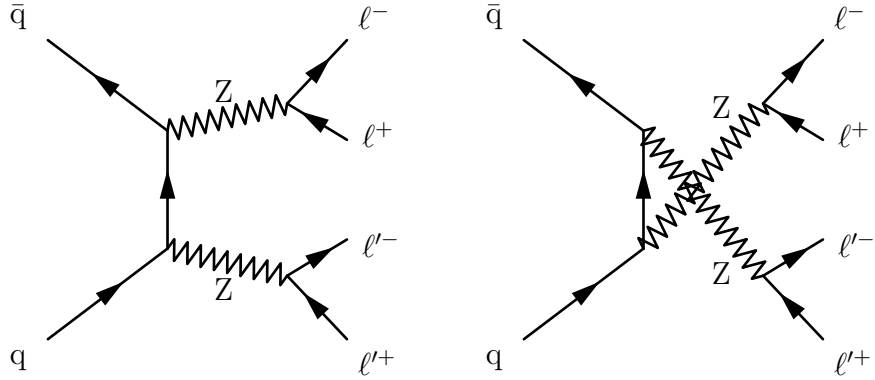


Figure 2.1: Leading order Feynman diagrams for $ZZ \rightarrow 4\ell$ production in pp collisions.

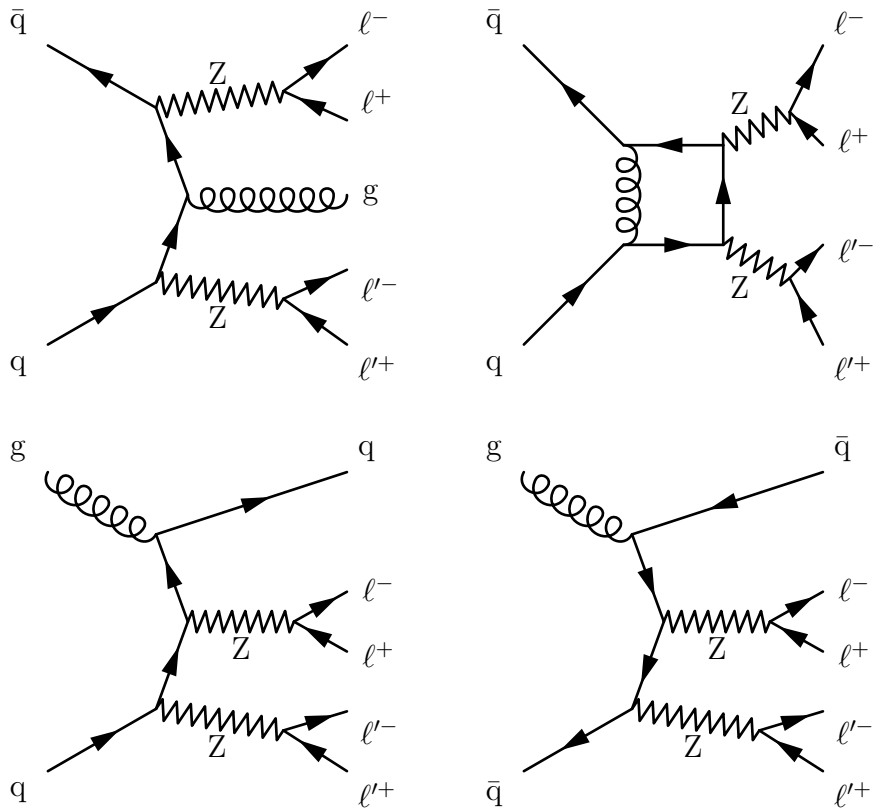


Figure 2.2: Three representative NLO Feynman diagrams for $ZZ \rightarrow 4\ell$ production in pp collisions. Clockwise from the top right, the NLO diagrams are examples of one-loop diagrams, real antiquark and quark emission, and real gluon emission.

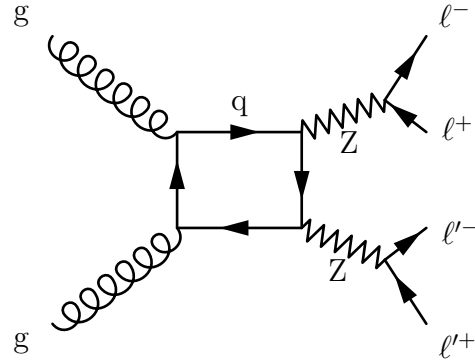


Figure 2.3: A LO box diagram for $ZZ \rightarrow 4\ell$ production through a quark loop in a gluon-gluon fusion event. This is formally an NNLO diagram for ZZ production overall, but is often included in NLO calculations because it accounts for a large fraction of the NNLO correction, due to the high effective gluon luminosity in proton collisions at high Q^2 .

36 Production of pairs of on-shell Z bosons¹ turns on sharply at the kinematic thresh-
 37 old $\sqrt{\hat{s}} = 2m_Z = 182.4$ GeV, and in proton-proton collisions at $\sqrt{s} = 13$ TeV, peaks
 38 around $m_{ZZ} \approx 200$ GeV before falling steeply at higher invariant masses. Continuum
 39 production occurs below the kinematic threshold when one or both Z bosons are re-
 40 placed by a Z^*/γ^* admixture, typically in the form of a $q\bar{q} \rightarrow Z$ event in which one of
 41 the incoming quarks emits a virtual photon as initial state radiation (ISR). Events of
 42 interest in this analysis (see Sections 5.4 and 6.3) generally have one on-shell Z , and
 43 a Z^*/γ^* at a lower mass. Nonresonant $Z\gamma^*$ production is generally flat as a function
 44 of invariant mass between roughly 100 GeV and the doubly resonant threshold.

45 2.1.1 Vector Boson Scattering

46 Vector boson scattering proceeds at hadron colliders through the diagrams shown in
 47 Fig 2.4, resulting in a $ZZjj$ final state. This fully electroweak (EWK) production

¹Events with two on-shell Z bosons are often called “doubly resonant,” but are a subset of “nonresonant” production in the sense that the ZZ system is not produced by a resonance. Either term may be used to distinguish “continuum” production from “singly resonant” production from $Z \rightarrow 4\ell$, $H \rightarrow ZZ^*$, or a potential new particle which decays to ZZ .

48 must be distinguished from the background of QCD-initiated ZZ + jets events (see
 49 Section 2.4). The hallmark of the EWK process is a pair of high energy, high rapidity
 50 jets from the quarks, which retain a high boost along the z -axis even after W^\pm or Z
 51 emission and are thus deflected through a small angle in the lab frame. At the same
 52 time, the ZZ system is produced with high invariant mass and low boost compared
 53 to QCD-initiated ZZjj events, in which the ZZ system recoils against the jets [41].
 54 Because the hard scattering interaction involves no color exchange or reconnection,
 55 VBS events are much less likely to have less energetic jets between the two high-energy
 56 quark jets. Useful variables to discriminate between EWK and QCD production
 57 therefore include the angle between the jets and their energy, their invariant mass,
 58 the ZZ invariant mass and rapidity, and the number of central jets (see Section 6.5
 59 for a full list and definitions).

60 2.1.2 Prior Measurements

61 Doubly resonant ZZ production was first observed in e^+e^- collisions at LEP by the
 62 ALEPH, OPAL, L3, and DELPHI experiments, from 183 GeV, just above the thresh-
 63 old center-of-mass energy, to the LEP maximum of 209 GeV [42–47]. Because the ZZ
 64 cross section is very small, these measurements used all possible final states except
 65 those in which all Z decay products were neutrinos or taus. This was possible because
 66 e^+e^- collisions do not suffer from the hadronization effect described above, so jets can
 67 be reliably matched to a hard scattering process, allowing identification of $Z \rightarrow q\bar{q}$
 68 decays. The measurements agreed with the SM, but were dominated by statistical
 69 uncertainties.

70 Production in hadron collisions was first observed by the CDF and D0 experi-
 71 ments, in 1.96 TeV $p\bar{p}$ events at Tevatron [48–52]. In contrast to the LEP measure-
 72 ments, $p\bar{p}$ colliders cause too many extraneous jets for the hadronic channels to be

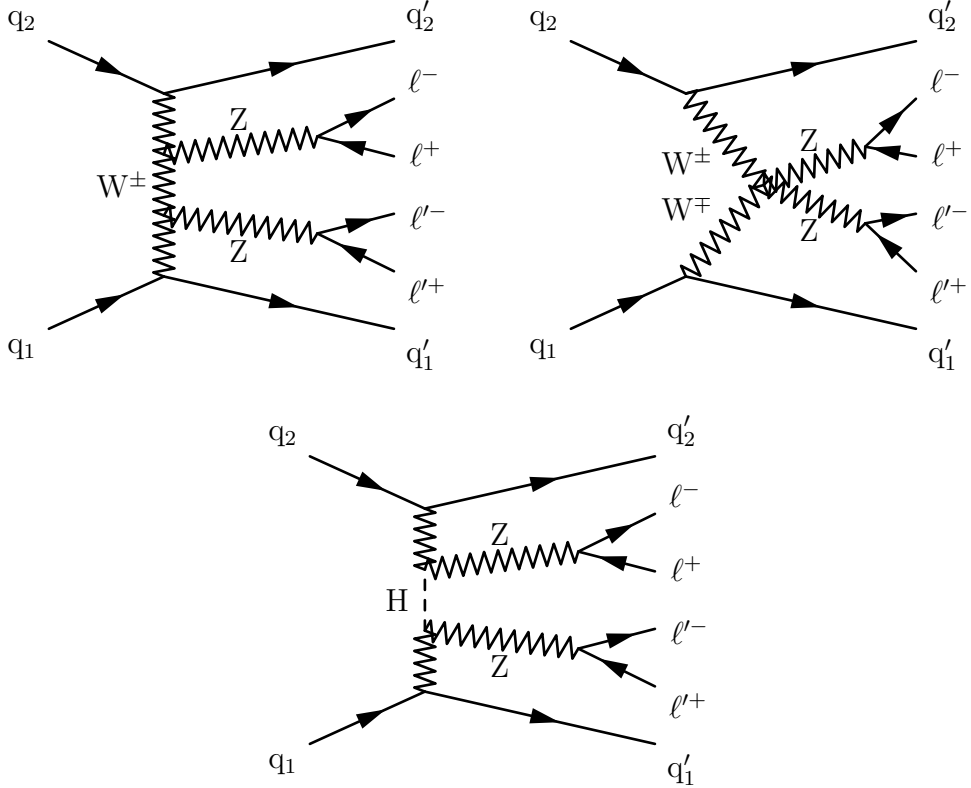


Figure 2.4: The primary ZZ VBS diagrams at hadron colliders. Diagrams also exist with antiquarks and with permutation and crossing of the final state particles. The interaction is only unitary to arbitrarily high energy when all diagrams are considered.

73 seen above the background, so only the 4ℓ and $2\ell 2\nu$ ($\ell = e, \mu$) final states were used.
 74 These fully leptonic decay modes have small branching fractions on top of the small
 75 ZZ cross section of around 1.6 pb [53], but the total Tevatron dataset of roughly 6 fb^{-1}
 76 was large enough for CDF and D0 to find a few dozen events each. Results were again
 77 fully consistent with the SM but the statistical uncertainties were large.
 78 The first run of the LHC (see Section 3.1) produced large datasets of pp collisions
 79 at $\sqrt{s} = 7$ and 8 TeV , producing ZZ events with a higher cross section than at
 80 Tevatron [40] and with a greater integrated luminosity. The measurement channels
 81 were again the fully leptonic 4ℓ and $2\ell 2\nu$ decays, and the cross sections were measured
 82 at $\sqrt{s} = 7$ and 8 TeV by both CMS [54–57] and ATLAS [58–60]. With a dataset

83 of roughly 20 fb^{-1} and signal event counts in the hundreds even for the low-rate 4ℓ
 84 channel, the 8 TeV measurements had the statistical power to include differential cross
 85 sections as functions of kinematic observables for the ZZ system and the associated
 86 jets. Statistical uncertainties were still larger than the systematic uncertainties, but
 87 they were at the level of 5–10% for the total cross section, compared to 30–50%
 88 at Tevatron and 15–150% at LEP depending on the experiment and center-of-mass
 89 energy².

90 CMS found that the total ZZ cross sections, defined as the cross sections of all
 91 events with two Z bosons in the mass range 60–120 GeV, to be

$$\begin{aligned}\sigma_{\text{ZZ}}(7 \text{ TeV}) &= 6.24^{+0.86}_{-0.80} (\text{stat})^{+0.41}_{-0.32} (\text{syst}) \pm 0.14 (\text{lumi}) \text{ pb} \\ \sigma_{\text{ZZ}}(8 \text{ TeV}) &= 7.7 \pm 0.5 (\text{stat})^{+0.5}_{-0.4} (\text{syst}) \pm 0.4 (\text{theo}) \pm 0.2 (\text{lumi}) \text{ pb},\end{aligned}\tag{2.4}$$

92 when measured with 4ℓ final states [55, 58], and

$$\begin{aligned}\sigma_{\text{ZZ}}(7 \text{ TeV}) &= 5.1^{+1.5}_{-1.4} (\text{stat})^{+1.4}_{-1.1} (\text{syst}) \pm 0.1 (\text{lumi}) \text{ pb} \\ \sigma_{\text{ZZ}}(8 \text{ TeV}) &= 7.2 \pm 0.8 (\text{stat})^{+1.9}_{-1.5} (\text{syst}) \pm 0.2 (\text{lumi}) \text{ pb}\end{aligned}\tag{2.5}$$

93 when measured with $2\ell 2\nu$ final states [56]. ATLAS found

$$\begin{aligned}\sigma_{\text{ZZ}}(7 \text{ TeV}) &= 6.7 \pm 0.7 (\text{stat})^{+0.4}_{-0.3} (\text{syst}) \pm 0.3 (\text{lumi}) \text{ pb} \\ \sigma_{\text{ZZ}}(8 \text{ TeV}) &= 7.3 \pm 0.4 (\text{stat}) \pm 0.3 (\text{syst}) \pm 0.2 (\text{lumi}) \text{ pb},\end{aligned}\tag{2.6}$$

94 using 4ℓ final states at 7 TeV [58] and a combination of 4ℓ and $2\ell 2\nu$ events at
 95 8 TeV [60]. ATLAS used a slightly different definition of the Z, considering it to
 96 have mass in the range 66–116 GeV, which reduces the SM expected cross section
 97 by 1.6% [61]. Measured cross sections from both experiments are again consistent
 98 with SM predictions of 6.7 ± 0.2 pb at 7 TeV and 8.3 ± 0.2 pb at 8 TeV, both calcu-
 99 lated at NNNLO in QCD with MATRIX, with factorization and renormalization scales

100 $\mu_F = \mu_R = m_Z$.

²Most LEP ZZ cross section measurements had statistical uncertainties around 20–40%; see references given in the text for details.

101 Searches for vector boson scattering were first performed at $\sqrt{s} = 8$ TeV. The first
 102 process examined was the low-background same-sign WW process $pp \rightarrow W^\pm W^\pm jj$
 103 studied at ATLAS, where evidence for electroweak production was observed at the
 104 level of a 3.6σ standard deviation excess over the null hypothesis [62], and at CMS,
 105 where a 2.0σ excess was found [63]. Subsequent searches for electroweak $Z\gamma jj$ pro-
 106 duction found a 3.0σ excess above the null hypothesis at CMS [64] and no significant
 107 excess at ATLAS [65]. A CMS measurement of $W\gamma jj$ production found a 2.7σ ex-
 108 cess above the null hypothesis consistent with electroweak production [66]. Searches
 109 for photon-photon VBS were performed as searches for exclusive and quasi-exclusive
 110 $\gamma\gamma \rightarrow W^+W^-$ production $pp \rightarrow p^{(*)}W^+W^-p^{(*)}$, in which the protons do not collide
 111 but instead both radiate photons, which scatter. CMS found evidence at the level
 112 of 3.4σ above the null hypothesis [67], and ATLAS saw a 3.0σ excess [68]. Roughly
 113 contemporaneously with this work, electroweak same-sign WW production was ob-
 114 served at CMS in 13 TeV collisions, with a significance of 5.5σ [69]. No searches for
 115 Electroweak ZZ production had been performed prior to the analysis described in the
 116 following chapters.

117 **2.2 Resonant ZZ*/Z γ^* Production**

118 Resonant production appears as a sharp peak in the four-lepton invariant mass distri-
 119 bution over the broad spectrum from nonresonant production. There are two known
 120 four-lepton resonances: single-Z decays to four leptons around 91 GeV, and Higgs
 121 decays to ZZ* around 125 GeV. Another resonance, caused by a new particle, could
 122 still be discovered at high mass, or at low mass but with a very small cross section.

123 2.2.1 Z Boson Decays to Four Leptons

124 A single Z boson may decay to a four-lepton final state when a lepton from a normal
 125 $Z \rightarrow \ell^+ \ell^-$ decay radiates a virtual photon, as shown in Fig 2.5. In a window around
 126 the Z mass of $80 < m_{4\ell} < 100$ GeV, t - and u -channel production (the diagrams of
 127 Fig 2.1 with γ^* for both bosons) contribute at the few-percent level (4% at $\sqrt{s} =$
 128 13 TeV). Four-fermion decays were studied in detail at LEP [70]. This included
 129 four-lepton decays, but used all $\ell^+ \ell^- f\bar{f}$ ($\ell = e, \mu, \tau$) final states, where f could be any
 130 fermion except the neutrinos. $Z \rightarrow 4\ell$ decays were also observed at 7 and 8 TeV at
 131 CMS, where the branching fraction was found to be $\mathcal{B}(Z \rightarrow 4\ell) = 4.2^{+0.9}_{-0.8}$ (stat) \pm
 132 0.2 (syst) $\times 10^{-6}$ [71], and at ATLAS, where it was found to be 3.20 ± 0.25 (stat) \pm
 133 0.13 (syst) $\times 10^{-6}$ in a slightly different phase space [72]. After correcting for phase
 134 space differences, the measurements are compatible with each other and with the SM.

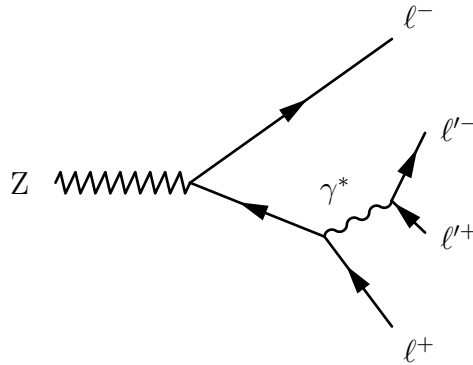


Figure 2.5: Tree-level Feynman diagram for $Z \rightarrow 4\ell$ production. Either initial lepton may radiate the γ^* .

135 2.2.2 Higgs Boson Production

136 The primary Higgs production mechanism in multi-TeV hadron collisions is gluon-
 137 gluon fusion through a quark loop, because of the gluon's high effective luminosity and
 138 the top quark's strong Yukawa coupling. Other mechanisms, in decreasing order by

139 cross section, include vector boson fusion (VBF), vector boson associated production
 140 (VH or “Higgsstrahlung”), and top-antitop associated production ($t\bar{t}H$). Tree-level
 141 Feynman diagrams for all four are shown in Fig. 2.6. The VBF process contributes to
 142 the unitarization of vector boson scattering along with the diagrams in Fig. 2.4. The
 143 SM cross sections for the various production mechanisms, and the Higgs branching
 144 fractions, are shown as functions of m_H near the measured mass of 125 GeV in Fig. 2.7.
 145 Gluon-gluon fusion has roughly an order of magnitude higher rate than the others.
 146 Decays to ZZ^* are heavily suppressed by the fact that, since $m_H < 2m_Z$, energy
 147 conservation requires one of the Z bosons to be far off its mass shell. Decays to four
 148 charged leptons are further suppressed by the small $Z \rightarrow \ell^+\ell^-$ branching fraction.
 149 However, the distinctive signature of four high-energy charged leptons in a single event
 150 is easy to detect with high efficiency and background rejection, and the momentum
 151 of electrons and muons can in general be measured with high precision, allowing
 152 the Higgs resonance to be easily seen as a sharp peak over a small, relatively flat
 153 background, and $H \rightarrow 4\ell$ is one of the most attractive channels for Higgs discovery
 154 and measurement of its properties.

155 2.2.2.1 Prior Measurements

156 Higgs boson searches at LEP were for Z-associated production, which has the highest
 157 cross section in e^+e^- collisions. The maximum LEP center-of-mass energy, 209 GeV,
 158 was just under the ZH threshold around 216 GeV. The LEP combined 95% confi-
 159 dence level (CL) lower limit on m_H was 114.4 GeV [74], and a combination of LEP
 160 data and electroweak precision measurements set an upper limit of 193 GeV [75].
 161 Searches at the CDF and D0 experiments at the Tevatron were combined to find a
 162 3.0σ local excess consistent with $m_H = 125$ GeV [76], and results from all the Teva-
 163 tron and LEP measurements and electroweak precision measurements were combined

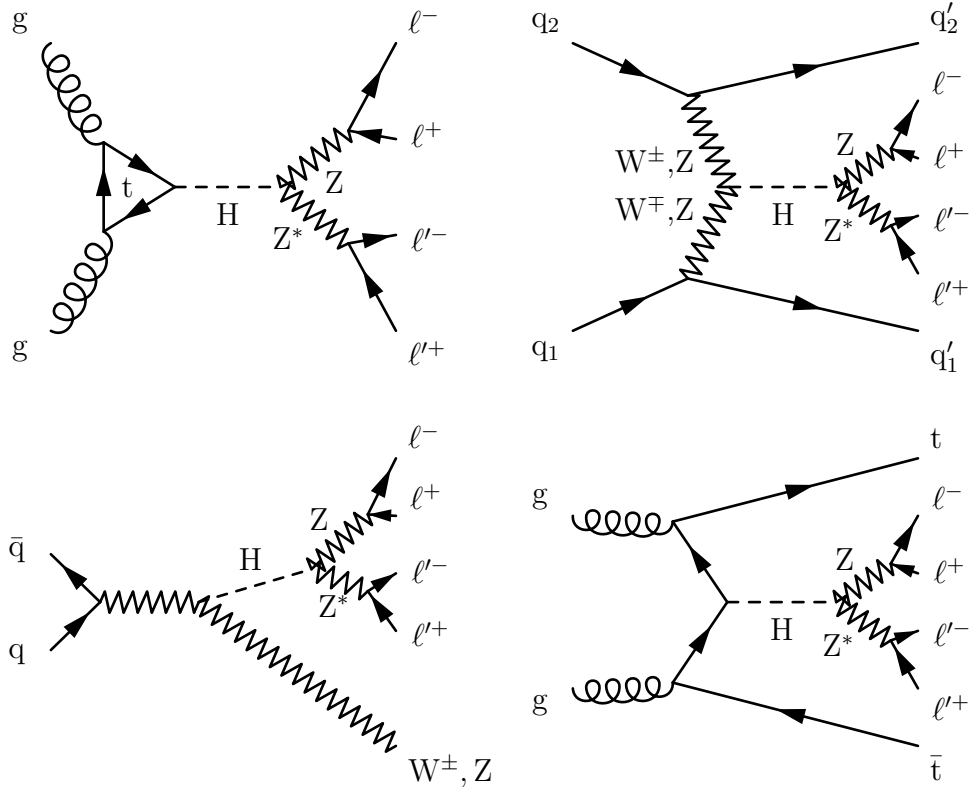


Figure 2.6: Tree-level Higgs production diagrams for gluon-gluon fusion (top left), VBF (top right), VH (bottom left), and $t\bar{t}H$, decaying to four leptons.

164 to place an upper mass limit of 158 GeV at 95% CL [77]. The Higgs was finally dis-
 165 covered simultaneously by the CMS and ATLAS collaborations with a combination
 166 of 7 and 8 TeV data [78, 79]. Its properties were subsequently investigated in detail
 167 at both experiments. The Higgs mass was found to be

$$m_H = 125.09 \pm 0.21 \text{ (stat)} \pm 0.11 \text{ (syst)} \text{ GeV} \quad (2.7)$$

168 based on a combination of data from the two experiments [80], and SM predictions
 169 of its properties have been confirmed by a number of measurements [81].

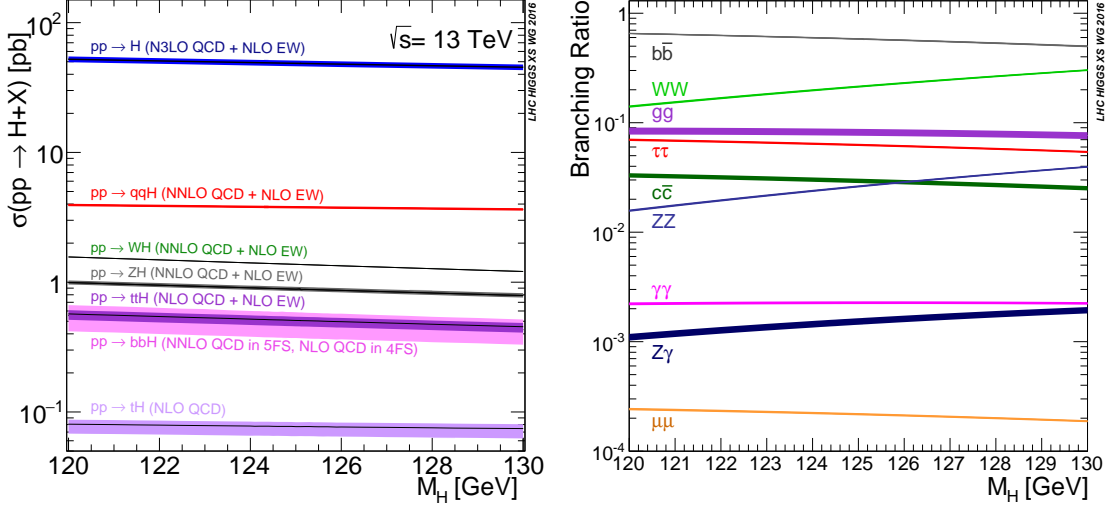


Figure 2.7: The SM cross sections for each Higgs boson production mode (left) and the Higgs branching fraction to several important final states (right), as a function of Higgs mass near the measured mass of 125 GeV. Both plots are reproduced from Ref. [73].

170 2.3 Anomalous Gauge Couplings

171 The primary hallmark of anomalous couplings is an enhanced cross section at center-
 172 of-mass energies of order 1 TeV [28]. The increase in cross section at high $m_{4\ell}$ implies
 173 higher transverse momentum for the outgoing Z bosons and leptons, as shown for two
 174 example aTGC models in Fig. 2.8. Searches for high-mass ZZ events are attractive
 175 because SM continuum production cross sections are extremely small above a few
 176 hundred GeV and all other sources of prompt or nonprompt four-lepton events are
 177 negligible, so even a handful of events would be an unambiguous sign of new physics.
 178 The search for nonzero aTGCs is performed using inclusive ZZ events, because the
 179 aTGC parameters should not have a large effect on jet distributions. The aQGC
 180 search is performed in ZZjj events because it would specifically enhance the VBS
 181 cross section at high mass.

182 The neutral aTGC parameters f_4^V and f_5^V are expected to have almost identi-

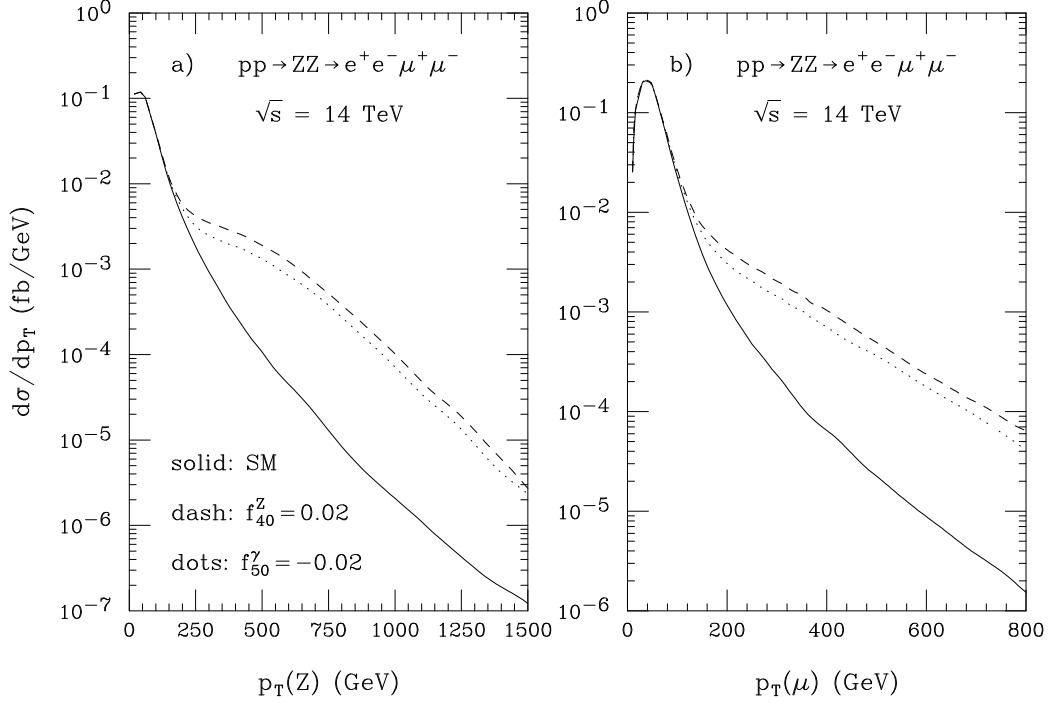


Figure 2.8: Cross section enhancements at high Z and μ momenta caused by example nonzero aTGCs. Reproduced from Ref. [28].

183 cal effects at high energy, so the search variables cannot be used to determine the
 184 relative strengths of the possible anomalous couplings [28]. However, because the
 185 terms governed by f_4^V have opposite behavior to the terms governed by f_5^Z under
 186 parity transformations, they affect the helicity amplitudes of the Z bosons and al-
 187 ter the angular distributions of the final-state leptons. Figure 2.9 shows the cross
 188 section as a function of total angular distance and the azimuthal angular difference
 189 between muons from the same Z decay for several example nonzero aTGCs and for
 190 the SM. These distributions could be used to distinguish between the possible aTGC
 191 parameters and determine the sign of the CP-conserving f_5^V terms.

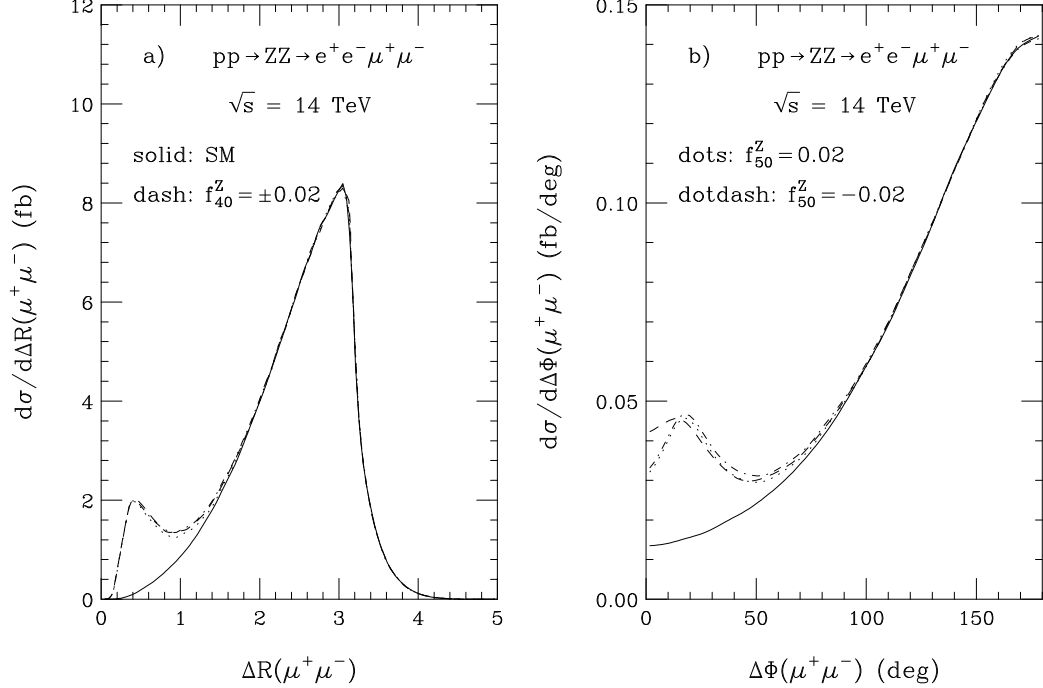


Figure 2.9: Total angular distance and azimuthal angular difference between muons from the same the same Z decay caused by several example nonzero aTGCs. Reproduced from Ref. [28].

192 2.3.1 Previous Limits

193 The first neutral aTGC searches were performed at LEP using ZZ and $Z\gamma$ events [46,
 194 47, 82, 83]. Depending on the experiment and parameter, 95% CL limits were gen-
 195 erally $\mathcal{O}(\pm 1)$, and the statistical combination set limits around 0.2–0.4 [75]. The
 196 first searches in hadron collisions were performed at Tevatron the by CDF collabo-
 197 ration, which set symmetric 95% CL limits in the range ± 0.10 –0.13 for all param-
 198 eters [84], and the D0 collaboration, which set symmetric limits around ± 0.20 –0.31
 199 for all parameters [85]. Both Tevatron experiments used a unitarity-preserving cutoff
 200 of $\Lambda = 1.2$ TeV. CMS and ATLAS set 95% CL limits at 7 TeV at $\mathcal{O}(\pm 0.1)$ [54, 58,
 201 86], and $\mathcal{O}(\pm 0.005)$ at 8 TeV [55, 87]. ATLAS presented limits from 7 TeV data with
 202 and without a unitarizing form factor; their 8 TeV results, and all CMS results, did

not use one. Prior to this work, the most stringent limits on all four neutral aTGC parameters were set by CMS with a combination of 7 and 8 TeV data [56],

$$\begin{aligned} -0.0022 < f_4^Z < 0.0026, \quad -0.0023 < f_5^Z < 0.0023, \\ -0.0029 < f_4^\gamma < 0.0026, \quad -0.0026 < f_5^\gamma < 0.0027. \end{aligned} \quad (2.8)$$

No prior aQGC searches were performed using ZZ processes, but both LHC experiments set limits on the ZZ-sensitive effective field theory operators using other channels. The most stringent limits on f_{T0} were from $\sqrt{s} = 8$ TeV $Z\gamma qq$ events at ATLAS [65], found to be

$$-3.4 < f_{T0}/\Lambda^4 < 2.9 \text{ TeV}^{-4} \quad (2.9)$$

at 95% CL, with similar results produced by CMS [64]. The most stringent limits on f_{T1} and f_{T2} were set by CMS at 8 TeV using same-sign WWqq events [63], and were found to be

$$-2.1 < f_{T1}/\Lambda^4 < 2.4 \text{ TeV}^{-4} \quad (2.10)$$

and

$$-5.9 < f_{T2}/\Lambda^4 < 7.1 \text{ TeV}^{-4}. \quad (2.11)$$

CMS and ATLAS produced nearly identical limits on f_{T8} and f_{T9} in the same $Z\gamma qq$ searches that set limits on f_{T0} ,

$$-1.8 < f_{T8}/\Lambda^4 < 1.8 \text{ TeV}^{-4} \quad (2.12)$$

and

$$-3.9 < f_{T9}/\Lambda^4 < 3.9 \text{ TeV}^{-4}. \quad (2.13)$$

2.4 Background Processes

Spurious events are categorized as irreducible backgrounds, i.e. those that are expected to have four prompt leptons, and reducible backgrounds, which have two

or three prompt leptons and another object that is misidentified as a prompt lepton. The only nontrivial irreducible backgrounds to inclusive $ZZ/Z\gamma^*$ production are WWZ triboson events in which all three bosons decay leptonically, and $t\bar{t}Z$ events in which both top quarks and the Z all decay leptonically as shown at tree level in Fig. 2.10. The most prominent reducible backgrounds are $WZ \rightarrow 3\ell\nu$ events in which a jet fragment is misidentified as a prompt lepton, $Z + \text{jets}$ events in which two jet fragments are misidentified, and leptonic $t\bar{t}$ events with two misidentified fragments from the secondary b-jets. For the VBS search, the background is real ZZ events which have two jets, but the jets originate from QCD interactions instead of the fully electroweak processes of Fig. 2.4. An example non-VBS $ZZ + 2\text{jets}$ diagram is also shown in Fig. 2.10.

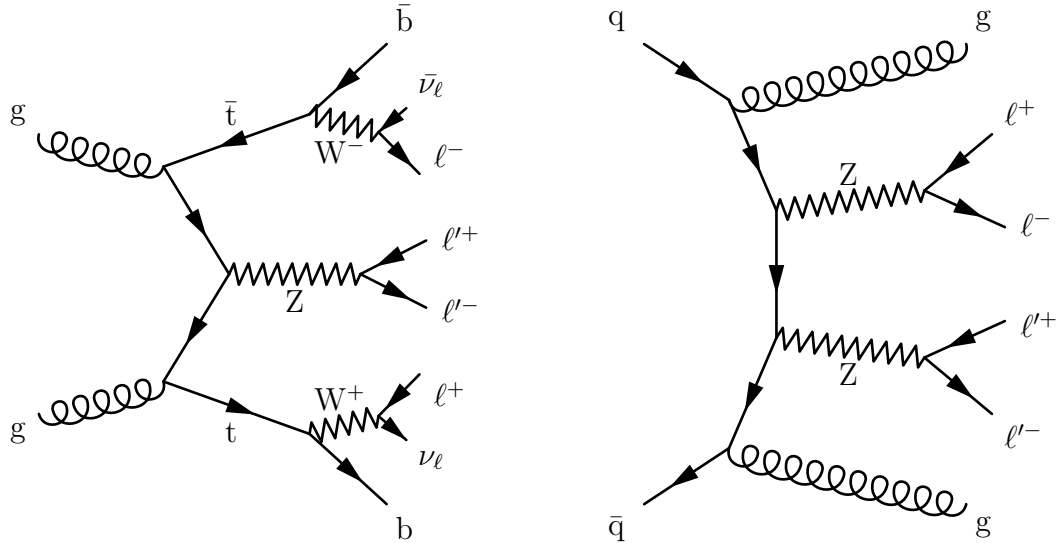


Figure 2.10: An example tree-level $t\bar{t}Z$ diagram (left), which is an irreducible background for inclusive $ZZ/Z\gamma^*$ production, and an example non-electroweak $ZZjj$ diagram (right).

0 Chapter 3

1 The CMS Experiment and the 2 CERN LHC

3 Production of controlled high-energy particle collisions, and detection of particles
4 created in those collisions, are monumental technical challenges. The apparatus used
5 to obtain the results presented in this thesis are the result of decades of work by
6 thousands of scientists and engineers, making use of many techniques developed in
7 the course of building and operating previous experiments. The CERN Large Hadron
8 Collider (LHC) [88, 89] accelerates pairs of charged hadron (proton or lead ion) beams
9 and collides them to provide a source of high energy particle interactions for several
10 fully independent detectors, including the Compact Muon Solenoid (CMS) [90], which
11 collected the data used in the studies presented here. Detailed descriptions of the
12 LHC and CMS follow.

13 3.1 The CERN Large Hadron Collider

14 The LHC, the most powerful particle accelerator and collider ever built, is a 26.7 km
15 circumference ring of superconducting magnets running through tunnels roughly
16 100 m below the suburbs and countryside near Geneva, Switzerland. It first produced
17 collisions suitable for collecting physics data in 2010 before generating large datasets
18 with beam energies of 3.5 TeV in 2011 and 4 TeV in 2012. Following a shutdown
19 for upgrades and repairs, it operated in 2015 and 2016 to deliver beam energies of
20 6.5 TeV. Beams collide head-on so that the center-of-mass frame of the proton-proton
21 system is the rest frame of the detectors, giving proton-proton center-of-mass ener-
22 gies of 7, 8, and 13 TeV respectively for collisions in 2010–2011, 2012, and 2015–2016.
23 Each successive energy was the highest ever achieved in controlled hadron-hadron
24 collisions, giving unprecedented access to extremely high-energy processes at every
25 step.

26 In addition to increasing collision energies, the LHC increased its rate of collisions
27 with each new machine configuration. The average event rate dN/dt for a process
28 with production cross section σ is determined by the instantaneous luminosity \mathcal{L} of
29 the collider,

$$\frac{dN}{dt} = \mathcal{L}\sigma \quad (3.1)$$

30 so a high instantaneous luminosity enables the observation of rare processes like Higgs
31 boson production. The LHC’s unprecedented luminosities have allowed collection of
32 the largest physics datasets in history.

33 The desire for high luminosities drove the decision to collide protons with other
34 protons instead of with antiprotons as was done at Tevatron, LHC’s predecessor at
35 Fermilab in Batavia, IL. Antiprotons simply cannot be produced in sufficient quan-
36 tities for a collider on this scale. Tevatron was designed to study many processes

37 that are $q\bar{q}$ -initiated, so it is useful to have valence antiquarks available in the col-
38 lisions. The LHC was designed with Higgs boson production in mind, and the two
39 most important Higgs production modes are proton/antiproton agnostic. Even for
40 $q\bar{q}$ -initiated processes, valence antiquarks are less critical at the LHC because, for the
41 same center of mass energy, the effective $q\bar{q}$ luminosity is higher for proton-proton
42 collisions at LHC energies than at Tevatron energies (1.98 TeV center-of-mass energy)
43 as discussed in Section 1.6.

44 In addition to protons, the LHC can accelerate beams of lead nuclei to 2.51 TeV
45 per nucleon, also the highest ever achieved. All studies presented in this thesis were
46 performed on proton-proton collision data, rendering the details of so-called “heavy
47 ion” beams beyond the scope of this document.

48 Beams are maintained and manipulated with magnets, most of them made of
49 superconducting niobium-titanium (NbTi) windings cooled to 1.9 K by superfluid
50 helium. Dipole magnets with fields up to 8.33 T bend the beam around the ring,
51 interspersed with quadrupoles for focusing. More quadrupoles and higher-moment
52 magnets keep the beams focused, squeeze them for collisions, and apply a number
53 of corrections. Superconducting radio frequency (RF) cavities operating at 400 MHz
54 accelerate the beam, maintain it at its final energy, and maintain bunch shape and
55 spacing.

56 3.1.1 Accelerator Chain, Layout, and Detectors

57 The LHC was built in tunnels originally constructed for the Large Electron-Positron
58 Collider (LEP), an e^+e^- collider that operated from 1989 to 2000. Using existing cav-
59 erns, tunnels, and infrastructure was a substantial cost-saving measure, but imposed
60 several important constraints on the LHC’s design. In LEP, the electron and positron
61 beams could be accelerated in opposite directions by the same magnets, because they

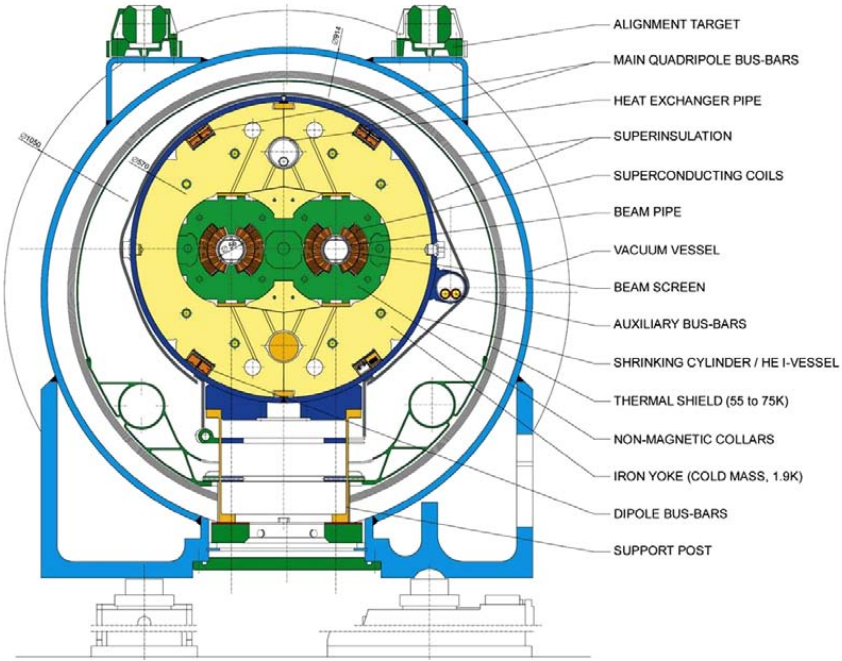


Figure 3.1: Schematic cross section of an LHC dipole and its attendant electrical and cryogenic infrastructure, reproduced from Ref. [88].

62 are oppositely charged. Conversely, proton beams require opposite magnetic fields for
 63 the two beams. Because the tunnels were not wide enough to accommodate two com-
 64 pletely separate beam lines, most of the magnets in the LHC use a twin-bore design,
 65 shown schematically in Fig. 3.1, in which the pipes and windings for the two beams
 66 share a common cryogenic system. The electromagnetic, mechanical, and cryogenic
 67 coupling of the two beamlines represents a significant engineering challenge [88, 89].

68 Because no single accelerator has the dynamic range necessary to take a stationary
 69 proton to TeV-scale energies, a chain of smaller accelerators repurposed from previous
 70 experiments feeds moderate-energy protons into LHC. Protons are obtained by ion-
 71 izing hydrogen atoms, then accelerated to 50 MeV by the Linac 2 linear accelerator
 72 and injected into the Proton Synchrotron Booster (PSB), the first of several circu-
 73 lar accelerators. The PSB feeds 1.4 GeV protons into the Proton Synchrotron (PS),
 74 which in turn injects them into the Super Proton Synchrotron (SPS) at 26 GeV. The

75 protons are then accelerated to 450 GeV in the SPS before being injected into LHC.
 76 A diagram of the entire accelerator chain is shown in Fig. 3.2.

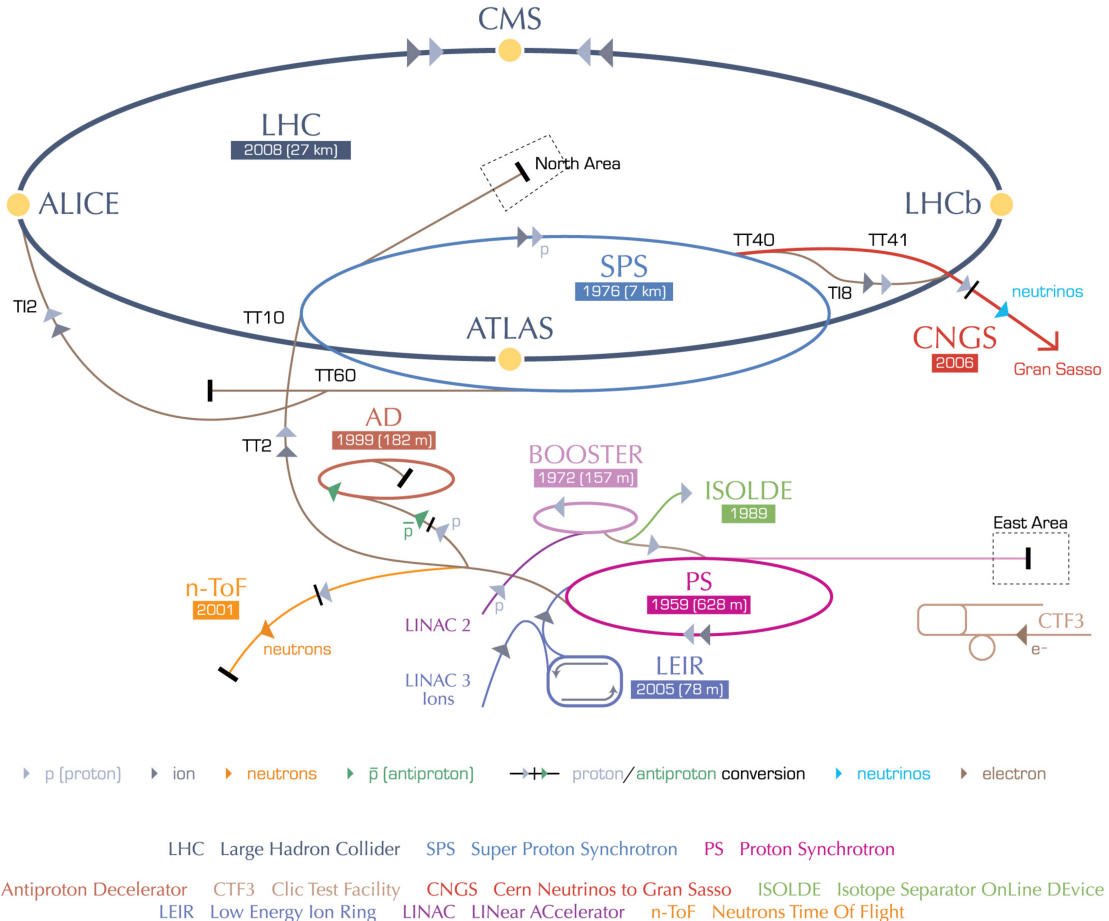


Figure 3.2: A schematic of the LHC accelerator chain and peripheral experiments, reproduced from Ref. [91].

77 The LHC ring is divided into eight sectors, each of which features a 528 m straight
 78 section connected to the adjacent sections by 2.45 km arcs. The straight section length
 79 was set by the need for RF cavities to accelerate LEP beams to counteract synchrotron
 80 radiation, which is a primary factor limiting electron and positron beam energy. This
 81 is not ideal for proton beams; protons' much higher mass means they radiate less and
 82 need fewer RF cavities. The straight sections feature access points numbered with
 83 Point 1 at the main CERN site in Meyrin, Switzerland, and the rest numbered 2–8,

84 increasing in the clockwise direction when viewed from above. Points 1, 2, 5, and 8
85 have beam crossing points and host detectors to study the resulting proton-proton
86 collisions. Points 3 and 7 feature collimators to reduce momentum and betatron
87 nonuniformities in the beams. The RF cavities are at Point 4 and the beams are
88 dumped after use or in the event of a magnet quench at Point 6. Beams are disbursed
89 and deflected into an 8 m long water-cooled graphite absorber by fast kicker magnets
90 which activate in a 3 μ s-long bunch-free region of the beam known as the abort gap.

91 The CMS detector is at Point 5 in Cessy, France, the furthest point on the ring
92 from the Meyrin site and Point 1, which houses ATLAS [92], a similar but fully
93 independent general-purpose particle detector. CMS and ATLAS use complemen-
94 tary detector technology so that any measurement or discovery by one can be made
95 concurrently or verified by the other. The other two experimental insertions feature
96 specialized detectors studying collisions at lower-luminosity beam interaction points.
97 The LHCb detector [93], at Point 8, studies hadronic physics with an emphasis on
98 b-hadrons, and ALICE [94] studies heavy ion collisions at Point 2. Three smaller
99 experiments share interaction points with the larger detectors, with TOTEM [95]
100 studying proton structure and the total proton-proton interaction cross section next
101 to CMS; LHCf [96] studying the π^0 energy spectrum and multiplicity near ATLAS;
102 and MoEDAL [97] searching for magnetic monopoles or other heavy, stable, ionizing
103 particles at Point 8 with LHCb.

104 **3.1.2 Operating Parameters**

105 With the beam energy set by the radius of the ring and the strength of available
106 magnets, the number of interesting physics events produced in LHC collisions depends

107 only on the integrated luminosity

$$\mathcal{L}_{int} = \int \mathcal{L} dt, \quad (3.2)$$

108 where \mathcal{L} is the instantaneous luminosity defined in Eq. (3.1) and the integral runs
 109 over the time the machine spends in collisions mode. LHC's availability for colli-
 110 sions depends on the electrical and mechanical stability of the accelerators and their
 111 support systems, including the cryogenics and the vacuum in the beam pipe. The
 112 instantaneous luminosity while running depends only on the beam parameters. For
 113 symmetric beams which each have n_b colliding gaussian bunches of intensity (i.e. num-
 114 ber of protons in the bunch) N_b , orbiting the ring with frequency f_{rev} and relativistic
 115 factor $\gamma = E_p/m_p$, the instantaneous luminosity is give by

$$\mathcal{L} = f_{rev} \frac{n_b N_b^2 \gamma}{4\pi \beta^* \epsilon_N} R, \quad (3.3)$$

116 where β^* is the amplitude of the beams' betatron oscillations around the nominal
 117 ring path at the interaction point, the normalized emittance ϵ_N is a measure of the
 118 beams' spread in both position and momentum space, and R is a geometrical factor
 119 accounting for the beam crossing angle,

$$R = \sqrt{1 + \left(\frac{\theta_c \sigma_z}{2\sigma^*} \right)^2}. \quad (3.4)$$

120 Here θ_c is the beams' crossing angle, and σ_z and σ^* are respectively the longitudinal
 121 and transverse RMS widths of the bunches in the lab frame.

122 3.1.2.1 Design

123 The machine parameters in the LHC design specification can be seen in the first col-
 124 umn of Table 3.1. Machine parameters during data taking have in general been quite
 125 different, due to both technological advances and technical challenges. In particular,

Table 3.1: LHC beam parameters as designed and in practice. As stated in the text, n_b is the number of colliding bunches, N_b is the number of protons in each bunch, β^* is the betatron amplitude at the interaction point, ϵ_N is the normalized emittance, and $\mathcal{L}_{(int)}$ is the instantaneous (integrated) luminosity.

Year	Design		Run I		Run II	
		2010	2011	2012	2015	2016
Energy per beam (TeV)	7	3.5	3.5	4	6.5	6.5
Bunch spacing (ns)	25	150	50	50	25	25
n_b	2808	348	1331	1368	2232	2208
$N_b (10^{11})$	1.15	1.2	1.5	1.7	1.15	1.25
β^* (m)	0.55	3.5	1.0	0.6	0.8	0.4
ϵ_N (mm mrad)	3.75	2.2	2.3	2.5	3.5	3.0
Peak pileup	FIXME	4	17	37	22	49
Peak $\mathcal{L} (10^{34} \text{cm}^{-2}\text{s}^{-1})$	1	0.02	0.35	0.77	0.52	1.53
$\mathcal{L}_{int} (\text{fb}^{-1})$		0.04	6.1	23.3	4.2	41.1

beam energy and number of colliding bunches are both lower than designed due to commissioning issues with the magnets and their safety systems [98], but increases in the number of collisions per bunch crossing (“pileup”) have more than compensated, leading to a peak instantaneous luminosity in 2016 that was more than 50% higher than designed. Operating parameters have changed frequently during data taking and upgrades are always ongoing.

3.1.2.2 Run I

The LHC came online in 2010 with a beam energy of 3.5 TeV, which was increased to 4 TeV in 2012. Bunches were spaced 50 ns apart instead of 25 ns to allow full exploitation of excellent injection chain performance [99]. Beams exiting the SPS had bunch intensity as much as 50% higher than anticipated in the original LHC design and beam emittance as low as 67% of nominal. This allowed the LHC to achieve 77% of its design instantaneous luminosity in 2012 despite having roughly half as many bunches in each beam.

Machine availability was overall good considering the complexity and relative newness of the LHC, with about 36% of scheduled time spent in stable beams. In all, LHC delivered 6.1 fb^{-1} to CMS and ATLAS in 2011 and 23.3 fb^{-1} in 2012, enough to allow discovery of the Higgs boson. The integrated luminosity for each year of LHC operation is shown as a function of calendar month and day in Fig. 3.3.

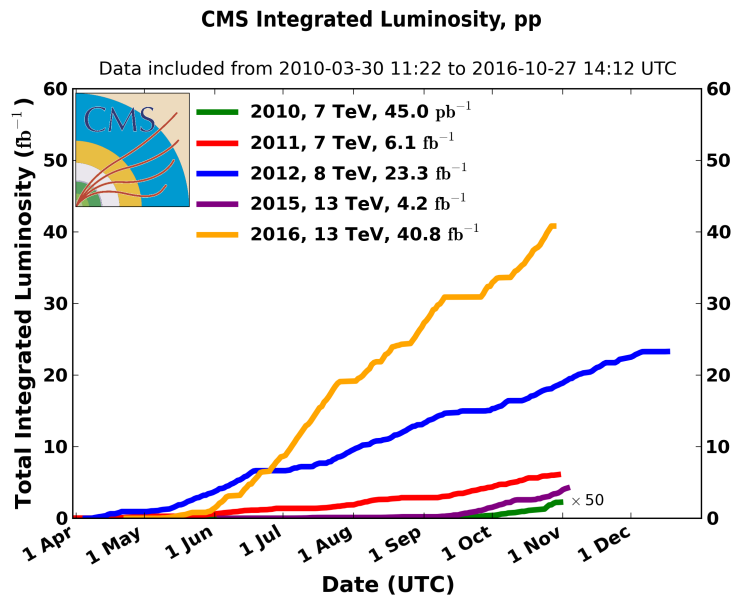


Figure 3.3: The integrated luminosity delivered to CMS in each year of LHC operation, shown as a function of the date within the year.

3.1.2.3 Run II

The LHC shut down for 2013 and 2014 to allow a number of repairs and upgrades, including measurements, repairs and upgrades on the electrical connections and cryogenic safety systems. Beam energies were increased to 6.5 TeV, close to the nominal 7 TeV. The bunch spacing was decreased to 25 ns while maintaining low emittance and high bunch intensity with the implementation of the beam compression merging and splitting (BCMS) scheme in which bunches are merged in the PS before they are split for injection into SPS, allowing higher bunch intensity [100]. This was offset

153 by vacuum problems in the SPS beam dump, which limited the total number of col-
 154 liding bunches to around 2200 [101]. Improvements in collimators and beam optics
 155 reduced β^* to 40 cm in 2016, lower than the design β^* of 55 cm. Overall instantaneous
 156 luminosities were substantially higher than originally designed.

157 Machine availability in Run II was excellent, with over 60% of planned time spent
 158 in stable beams [101]. The world’s first 13 TeV collisions in 2015 were the subject of
 159 a number of measurements and searches, though the 4.2 fb^{-1} integrated luminosity
 160 delivered to Points 1 and 5 in 2015 was less than planned due to several mechanical is-
 161 sues. The integrated luminosity achieved in 2016, 41.1 fb^{-1} , was far above the roughly
 162 25 fb^{-1} expected and more than all previous runs combined, allowing measurements
 163 and searches of unprecedented sensitivity and reach, including those presented in this
 164 Thesis.

165 3.2 The Compact Muon Solenoid Detector

166 The CMS detector [90] is a general-purpose particle detector located in a cavern
 167 roughly 100 m below the surface at LHC Point 5. Though designed to do a wide
 168 range of physics analyses, CMS was designed specifically with Higgs boson discovery
 169 in mind. Primary design goals include

- 170 • High-efficiency reconstruction of charged particles with precise measurement of
 171 their trajectories and momenta
- 172 • Good electromagnetic energy resolution, including diphoton and dielectron mass
 173 resolution
- 174 • Hermetic calorimetry for good missing transverse energy and dijet mass resolu-
 175 tion

176 • Good muon identification, momentum resolution (including dimuon mass reso-
 177 lution), and charge determination over a broad range of energies

178 To this end, CMS features a silicon tracker, a scintillating crystal electromagnetic
 179 calorimeter (ECAL), and a hermetic hadronic calorimeter (HCAL) inside a 3.8 T
 180 solenoid magnet surrounded by ionized gas muon tracking devices, all of which can
 181 be seen as part of the whole detector in Fig. 3.4. Decisions on which events to read
 182 out are made on-line by a two-level trigger system. Descriptions of these systems
 183 follow.

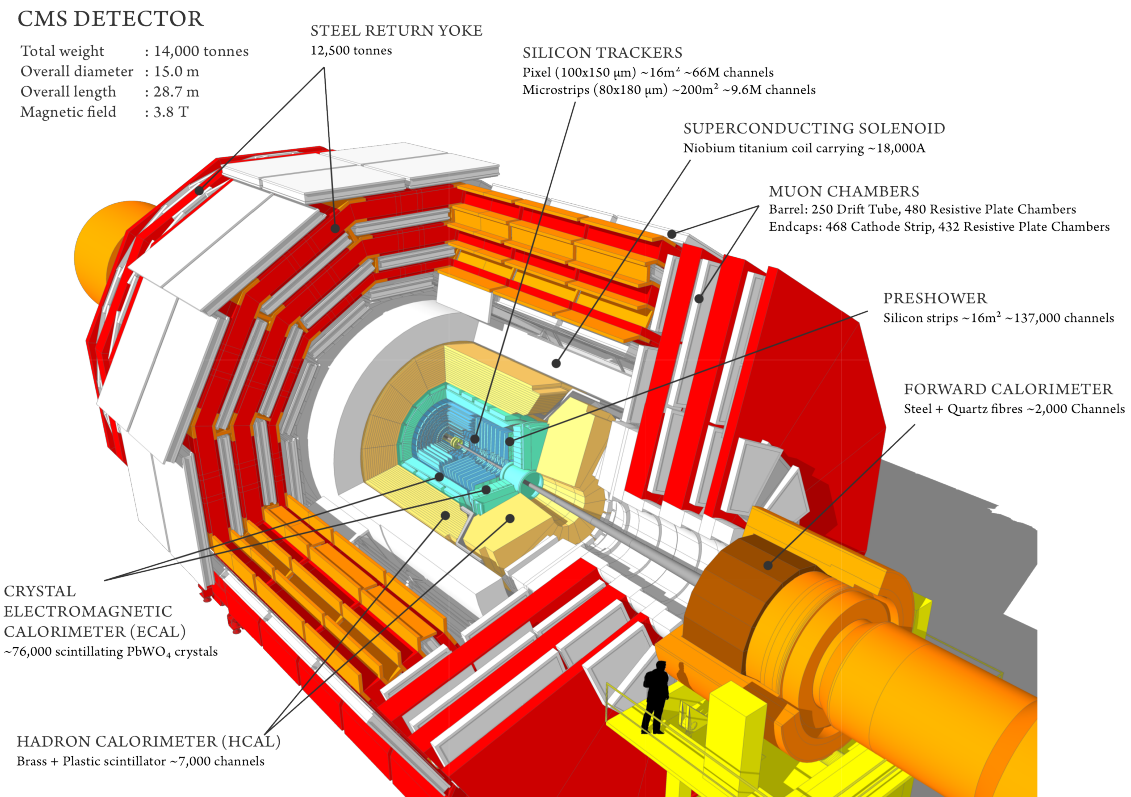


Figure 3.4: Cutout schematic of CMS with all major subdetectors, the beamline, the magnet, and the return yoke visible. Reproduced from Ref. [102].

¹⁸⁴ **3.2.1 Terminology and Geometry**

¹⁸⁵ The CMS detector systems are arranged in cylindrical layers with the interaction
¹⁸⁶ point at the center, serving as the origin for the coordinate system. The coordinate
¹⁸⁷ system is defined with the positive- x direction pointing toward the center of the
¹⁸⁸ ring, positive- y pointing vertically up, and positive- z pointing parallel to the beam
¹⁸⁹ in the counterclockwise direction when the LHC ring is viewed from above. Particle
¹⁹⁰ momenta are typically expressed in quasicylindrical coordinates (p_T, η, ϕ) . Here p_T is
¹⁹¹ the magnitude of the particle's momentum transverse to the beam

$$p_T \equiv \sqrt{p_x^2 + p_y^2}, \quad (3.5)$$

¹⁹² and ϕ is the azimuthal angle, i.e. the angle from the x -axis to the particle's trajectory
¹⁹³ in the x - y plane. The pseudorapidity η is defined as

$$\eta \equiv -\ln \left[\tan \left(\frac{\theta}{2} \right) \right] \quad (3.6)$$

¹⁹⁴ where θ is the polar angle measured from the z -axis. The relativistic rapidity

$$y \equiv \frac{1}{2} \ln \left(\frac{E + p_z}{E - p_z} \right), \quad (3.7)$$

¹⁹⁵ converges to the pseudorapidity in the limit of massless particles. Pseudorapidity
¹⁹⁶ is preferred to rapidity because it is purely geometrical, with no dependence on the
¹⁹⁷ particle energy. Both are preferred over θ because rapidity differences are invariant
¹⁹⁸ under longitudinal boosts, and because hadron flux at colliders is roughly constant as
¹⁹⁹ a function of rapidity. The transverse energy E_T is the the magnitude of the particle's
²⁰⁰ four-momentum transverse to the beam, equal to p_T in the limit of massless particles.
²⁰¹ Spatial coordinates are expressed as (r, η, ϕ) , where r is the distance from the beam
²⁰² in the x - y plane.

203 **3.2.2 Magnet and Inner Tracking System**

204 A particle of charge q moving through a uniform magnetic field of strength B that
 205 points in the z direction will travel in a helix of radius R , given by

$$R = \frac{p_T}{|q|B}, \quad (3.8)$$

206 with the chirality of the helix determined by the sign of q . Thus one can determine the
 207 transverse momentum of the particle by measuring its path through the magnetic field
 208 and finding the radius of curvature. In practice, all but the lowest-energy particles
 209 leave too short an arc in the detector for direct measurement of the radius, so the
 210 sagitta of the arc is used instead, given by

$$s = \frac{qBL^2}{8p_T} \quad (3.9)$$

211 where L is the length of the chord spanning the arc (typically equal to the radius of
 212 the tracking system). The transverse momentum resolution varies as

$$\frac{\delta p_T}{p_T} \propto \frac{p_T}{BL^2}, \quad (3.10)$$

213 so a strong field and a large tracking volume are vital to keeping measurements precise
 214 even at high energies.

215 To this end, CMS contains the world's largest superconducting magnet¹, a solenoid
 216 13 m long and 6 m in diameter, which generates a nearly-uniform 3.8 T field in the
 217 centralmost part of the detector [103]. To measure the paths of charged particles in
 218 the field, the volume closest to the interaction point contains layers of silicon sensors
 219 that detect hits from charged particles with high efficiency and excellent position
 220 resolution, between 4.4 cm and 1.1 m from the beam for 2.7 m on either side of the
 221 interaction point. This system, called the inner tracker and shown schematically

¹Largest in the sense of having the largest stored energy when at constant full field. The largest by size is the ATLAS barrel toroid.

in Fig. 3.5, consists of an inner pixel detector surrounded by a larger silicon strip detector. Both consist of concentric cylinders of sensors covering the barrel of the detector capped by discs covering the high- η region, up to $|\eta| < 2.5$. With a total of roughly 200 m^2 of silicon, the inner tracker is the largest silicon tracker in the world. Tracks may be reconstructed with hits in as many as 14 layers. The downside of this is that the tracker and its mechanical support structure represent a substantial amount of material for electrons and photons to interact with before they reach the calorimeters, with total material budget between 0.4 radiation lengths ($\eta = 0$) and 1.8 radiation lengths ($|\eta| \approx 1.4$), as shown in Fig. 3.6. The tracker-only p_T uncertainty is around 1.2% at 200 GeV and 15% at 1 TeV . Tracker readout is too slow for it to be used in the L1 trigger (see Section 3.2.6.1), the first set of trigger decisions must be made using only information from the calorimeters and outer muon system.

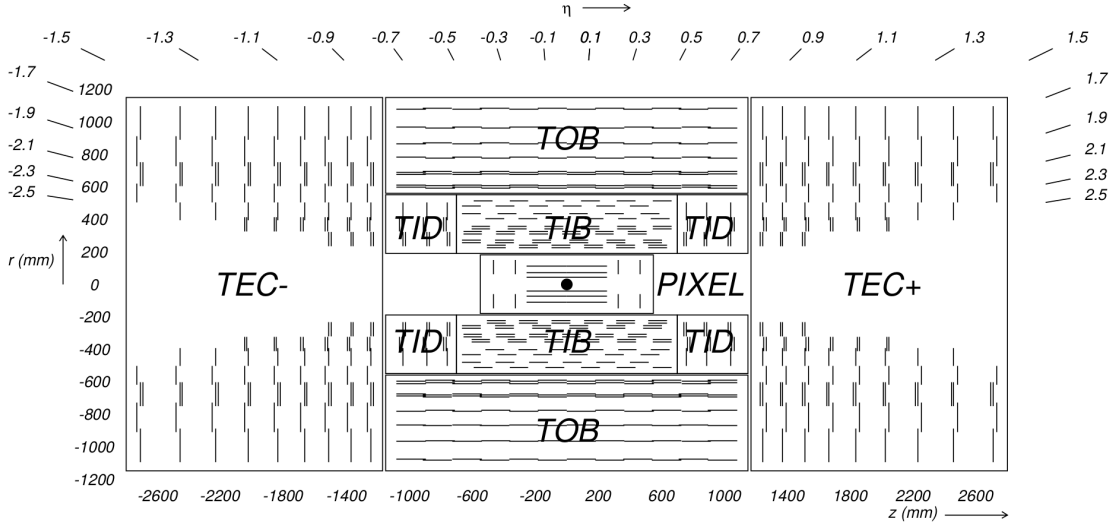


Figure 3.5: Diagram of the inner tracker layout, reproduced from Ref. [90].

As the system closest to the interaction point, the inner tracker is subject to extremely high radiation doses, equivalent to 840 kGy for the innermost pixel layer over an integrated luminosity of 500 fb^{-1} , so radiation tolerance is a major design constraint for both the sensors and readout electronics [104]. Leakage currents in

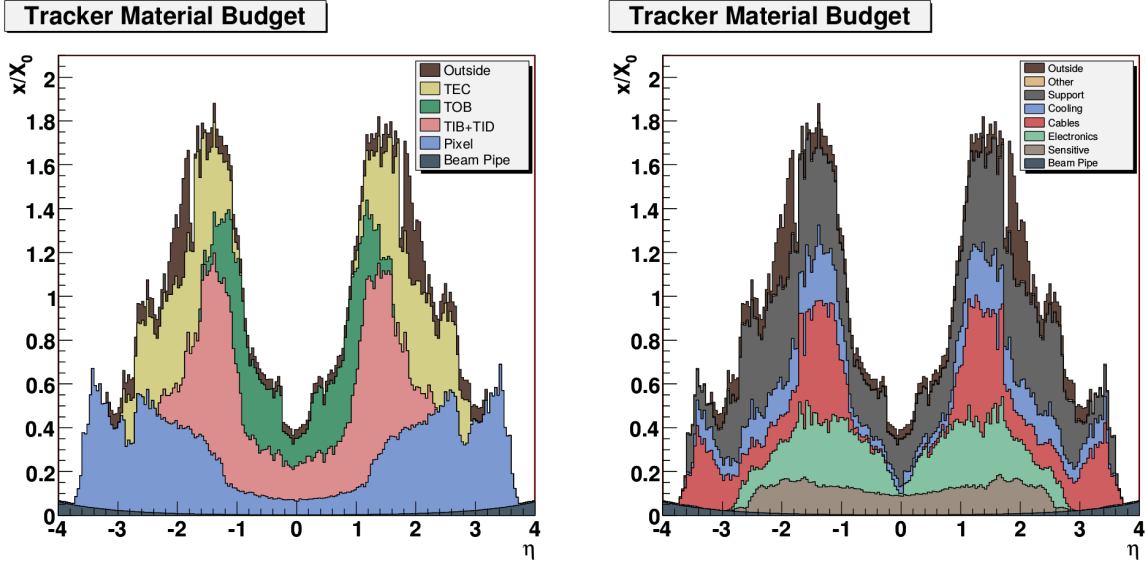


Figure 3.6: Total tracker material budget in units of electromagnetic radiation lengths, as a function of pseudorapidity. At (left) the total is divided by detector subsystem, at (right) by the function of the material. Reproduced from Ref. [90].

the sensors, which degrade sensor performance, increase linearly with radiation fluence and exponentially with temperature. Because leakage currents cause self-heating in the silicon, they can create a dangerous positive thermal feedback loop if the sensors are not cooled below -10°C during operation. Reverse annealing, a process by which radiation-induced defects in the silicon can cause further damage months after the radiation dose is received, can be mitigated by keeping the sensors below 0°C at all times except for brief maintenance periods [90]. Therefore, to improve tracker performance and increase the detectors' lifetimes, a gas cooling system is used to keep the strip tracker around -15°C and the pixel detector around -20°C during operation.

3.2.2.1 Pixel Detector

The pixel detector [104], consisting of three layers in the barrel and two in the endcap, is responsible for accurate reconstruction of primary proton-proton interaction ver-

tices and secondary vertices from decays of b-hadrons or other long-lived particles, as well as providing “seed” tracks that may be used in strip tracker reconstruction. As the system closest to the interaction point, the pixel system experiences the highest charged-particle flux and therefore must have extremely fine granularity to differentiate between nearby particles. The 66 million pixels in the system have a cell size of $100 \times 150 \mu\text{m}^2$. Interpolation of the analog signals from the individual pixels allows a final spatial resolution of $15 \mu\text{m}$ in each direction. The outermost barrel layer is 10.2 cm from the beam, and the second endcap disk is 46.5 cm from the interaction point. The sensor modules are arranged such that at least three sensors cover the solid angle within the pixel detector’s acceptance.

3.2.2.2 Strip Tracker

Outside the pixels is the silicon strip tracker [104], extending out to 1.1 m in the r direction and ± 2.8 m in the z direction. The tracker is divided into inner and outer subdetectors, each of which has both barrel cylinders and endcap discs. In total, there are ten layers in the barrel and nine in each of the endcaps. The inner tracker uses $320 \mu\text{m}$ -thick sensors with a typical strip cell size of $10 \text{ cm} \times 80 \mu\text{m}$, leading to hit resolutions of $23\text{--}35 \mu\text{m}$. The outer tracker uses $500 \mu\text{m}$ -thick sensors with typical strip sizes up to $25 \text{ cm} \times 180 \mu\text{m}$, leading to hit resolutions of $35\text{--}53 \mu\text{m}$.

3.2.3 Electromagnetic Calorimeter

Outside of the tracker is the electromagnetic calorimeter (ECAL), which is designed to absorb and measure the energy of electrons and photons. ECAL is made of 68,524 radiation tolerant lead tungstate (PbWO_4) crystals arranged in a cylindrical barrel (EB) covering $|\eta| < 1.444$ and two endcap discs (EE) covering $1.566 < |\eta| < 3.0$. The geometry of the ECAL barrel and endcap can be seen in Fig. 3.7; the small

275 gap between the barrel and endcap is necessary to accommodate cabling and support
 276 structures for the tracker. PbWO₄ crystals scintillate blue-green light and are op-
 277 tically transparent, so the resulting light can be read out by avalanche photodiodes
 278 (APDs) in the barrel and vacuum phototriodes (VPTs) in the endcap. ECAL's gran-
 279 ularity is set by PbWO₄'s small Molière radius of 2.2 cm, which is also the size of the
 280 square front faces of the barrel crystals, which flare out to 2.6 cm at the back, giving
 281 them a truncated pyramid shape covering a roughly 0.0174×0.174 area of $\eta\phi$ space.
 282 The endcap crystals go from 2.86 cm squares at the front to 3.0 cm at the back.

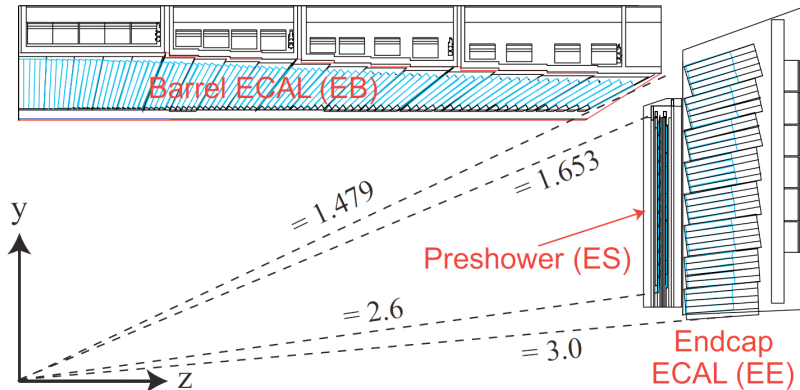


Figure 3.7: Diagram of ECAL geometry, reproduced from Ref. [105].

283 One of the primary design innovations of CMS—the eponymous compactness—
 284 was to place the calorimetry inside the magnet so that tracks can be unambigu-
 285 ously associated with energy deposits in the calorimeters without interference from
 286 scattering in the magnet coils. This is possible in part thanks to the high density
 287 (8.28 g/cm^3) and short radiation length (0.89 cm) of PbWO₄, which allow ECAL
 288 crystals to be only 23 cm long in the barrel and 22 cm long in the endcap while still
 289 spanning 25.8 and 24.7 radiation lengths, respectively. This is enough to ensure that
 290 few electrons or photons escape ECAL with any appreciable remaining energy.

291 The total scintillation light yield is relatively low, averaging just 4.5 photons
 292 per MeV deposited. This is partially compensated by the fact that virtually all of

293 ECAL is active material and no energy is lost to uninstrumented absorbers, but
 294 Poisson fluctuations in the yield are still the largest contribution to ECAL energy
 295 resolution for most electron and photon energies. This statistical uncertainty is repre-
 296 sented by the first term in the full resolution equation,

$$\left(\frac{\delta E}{E}\right)^2 = \left(\frac{2.8\%}{\sqrt{E/\text{GeV}}}\right)^2 + \left(\frac{0.12}{E/\text{GeV}}\right)^2 + (0.30\%)^2. \quad (3.11)$$

297 The second term comes from electronic noise and noise from pileup, and the last term
 298 represents intrinsic differences between crystals. The upside to PbWO₄'s scintillation
 299 is that it is fast: roughly 80% of the light is emitted in the 25 ns between bunch
 300 crossings, so energy measurements require integration over only a few bunch crossings.

301 3.2.4 Hadronic Calorimeter

302 Between ECAL and the magnet is the hadronic calorimeter (HCAL), responsible for
 303 measuring the energy of hadronic jets. HCAL is a sampling calorimeter, meaning
 304 that the hadrons pass through dense, uninstrumented material and the products of
 305 the resulting interactions deposit energy in scintillators which are used to measure the
 306 total energy of the original incoming particles. The HCAL barrel (HB, $|\eta| < 1.305$)
 307 and endcap (HE, $1.305 < |\eta| < 3.0$) are made of layers of brass absorber interleaved
 308 with plastic scintillating tiles. The energy resolution in HB and HE is given by

$$\left(\frac{\delta E}{E}\right)^2 = \left(\frac{90\%}{\sqrt{E/\text{GeV}}}\right)^2 + (4.5\%)^2. \quad (3.12)$$

309 The first term is from the stochastic evolution of hadronic showers in the absorber,
 310 the second is from calibration uncertainties.

311 The geometry of HB, HE, and HO is shown in Fig. 3.8. The thickness of HB and
 312 HE is constrained by the size of the magnet, varying from 5.4 nuclear interaction
 313 lengths in the central barrel to more than 10 in the endcaps. Because HB is not thick

314 enough to absorb all hadrons in the barrel, there is an extra outer HCAL component
 315 (HO) outside of the magnet, consisting of two more layers of scintillator on either
 316 side of a 20 cm-thick iron “tail catcher” covering $|\eta| < 1.3$. With HO and the 1.1
 317 interaction lengths in ECAL considered, no part of the calorimeter system spans
 318 fewer than 11.8 interaction lengths except in the gaps between barrel and endcap,
 319 minimizing the flux of hadronic “punchthrough” interacting with the muon system.
 320 The total material budget in front of the layers of the muons systems is shown in
 321 Fig. 3.9.

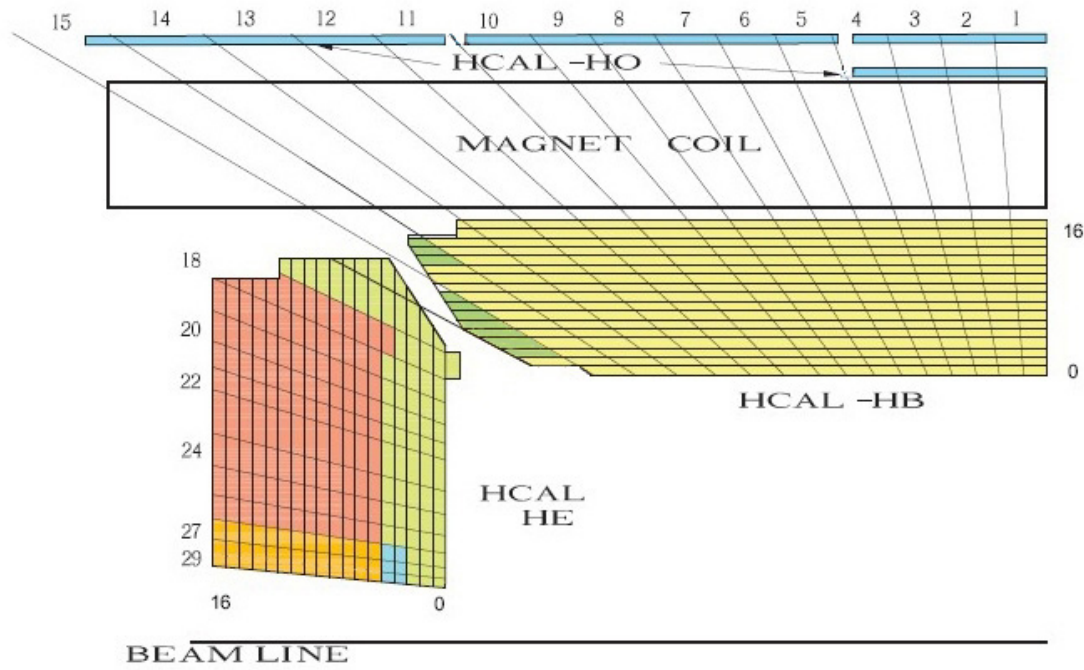


Figure 3.8: Diagram of HCAL geometry, reproduced from Ref. [90].

322 Closer to the beam line on each side, the forward hadronic calorimeter ($3.0 <$
 323 $|\eta| < 5.2$) is made of iron and quartz fibers instead of brass and plastic scintillator to
 324 maximize radiation hardness. It acts as a Cherenkov detector with the quartz fibers
 325 as the active detection element. Half the fibers extend the entire depth of HF, while
 326 the other half start after the hadrons have traversed 22 cm of iron, allowing some

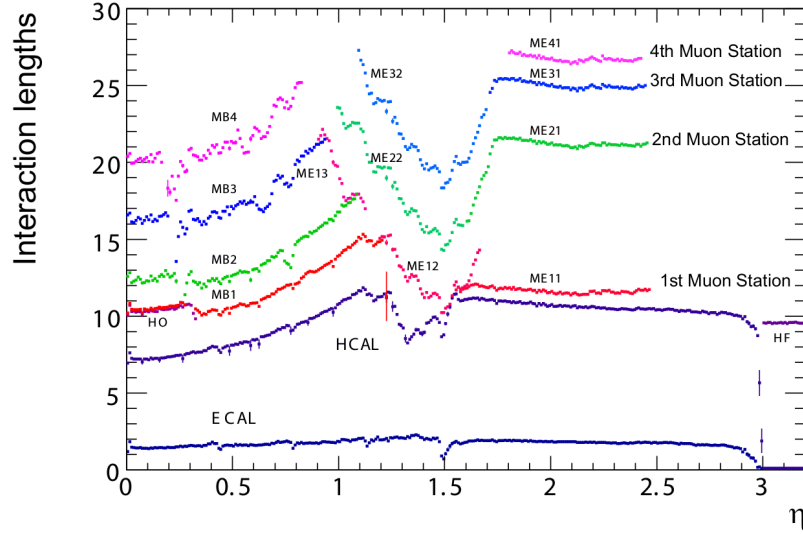


Figure 3.9: Total material budget in units of nuclear interaction lengths, as a function of pseudorapidity, reproduced from Ref. [90].

327 differentiation between electromagnetic and hadronic energy. The energy resolution
 328 in HF is given by

$$\left(\frac{\delta E}{E}\right)^2 = \left(\frac{172\%}{\sqrt{E/\text{GeV}}}\right)^2 + (9\%)^2, \quad (3.13)$$

329 where the terms have the same physical interpretation as those in Eq. (3.12). HF
 330 improves CMS's missing energy resolution by roughly a factor of three.

331 3.2.5 Muon Spectrometer

332 Many of the most interesting physics processes at the LHC involve high energy muons,
 333 so muon identification, triggering, and momentum measurement are important de-
 334 sign goals. Muons leave very little energy in the calorimeters, so ECAL and HCAL
 335 cannot be used for triggering and identification as they are for electrons, photons and
 336 hadrons, or to improve momentum measurements of high- p_T muons whose tracks are
 337 too straight to allow good measurements of their curvature. Instead, these functions
 338 are provided for muons by three gas-based systems surrounding the rest of the de-
 339 tector [106, 107]. In all three, ionizing gas chambers provide hits which form a track.

340 The magnetic field for this is provided by the return yoke, a set of steel plates inter-
 341 leaved with the muon chambers which confine the solenoid's magnetic return field.

342 The yoke plates weigh a total of 10,000 t and are fully saturated by the solenoid.

343 Unlike the inner tracker, the muon systems can be read out fast enough to provide
 344 triggering. Because muons above 3 GeV generally traverse the muon system while
 345 most other measurable particles are stopped in the calorimeters, magnets, or return
 346 yoke, the muon system provides high efficiency, low-background muon identification.

347 The muon system's momentum measurements are not competitive with the inner
 348 tracker's at low p_T , but a combined fit of the inner track and the muon system
 349 ("standalone") track improves muon p_T resolution above roughly 200 GeV. The
 350 geometry of all three muon systems and the return yoke can be seen in Fig. 3.10.

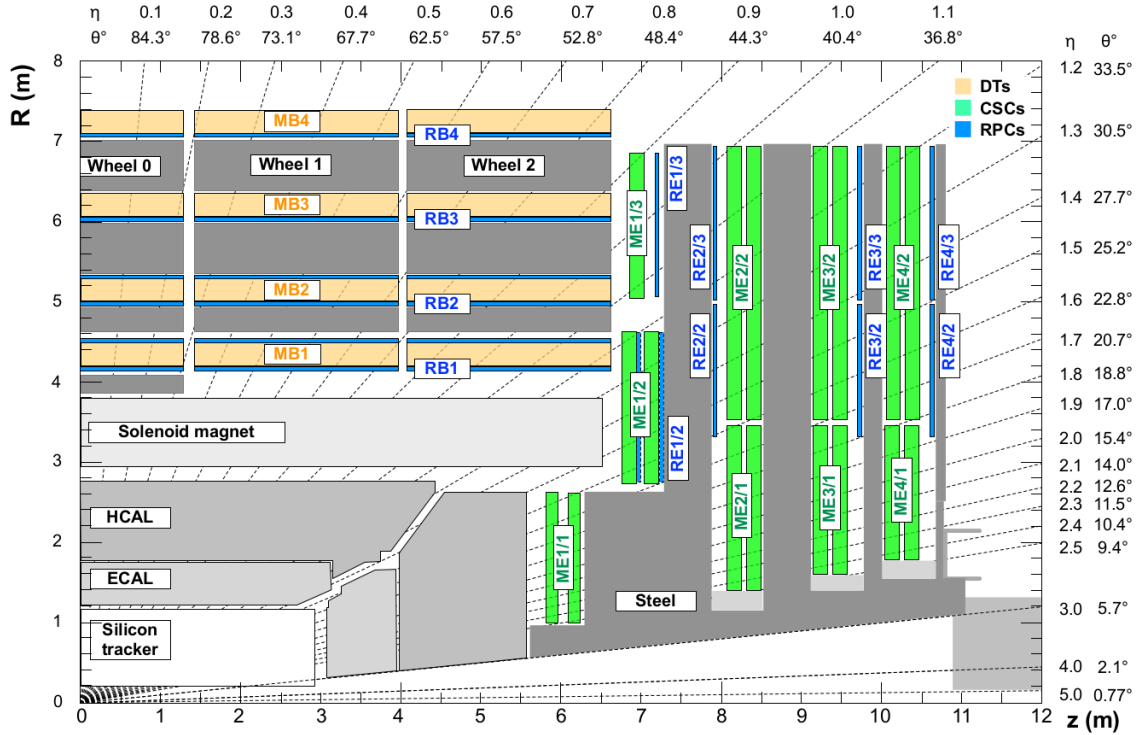


Figure 3.10: Diagram of muon system and return yoke geometry, reproduced from Ref. [107]. The magnet, calorimeters, and inner tracker are also visible.

351 **3.2.5.1 Drift Tubes**

352 In the barrel ($|\eta| < 1.2$), drift tube (DT) chambers are arranged in four “stations”
 353 separated by the steel layers of the yoke. Stations are made of two or three superlayers
 354 (SLs) of four layers of rectangular drift cells. Adjacent layers are staggered latterally
 355 by half a drift cell width to avoid gaps. Each station has two SLs with wires running
 356 parallel to the beam to measure muon tracks in the $r\text{-}\phi$ plane, separated by an
 357 aluminum honeycomb lattice to provide mechanical rigidity and act as a spacer. The
 358 inner three stations contain an extra SL on the outer side of the spacer with wires
 359 perpendicular to the beam line, to measure muon position along the z -axis.

360 Each drift cell contains a roughly 2.4 m-long wire in gas (85% Ar, 15% CO₂). The
 361 electric field in the cell is provided by aluminum tape glued to the top and bottom
 362 of the cell and held at +1.8 kV relative to the grounded aluminum plates above and
 363 below. Aluminum tape cathodes on the side of the cell are held at -1.2 kV, while the
 364 wires act as +3.6 kV anodes. The width of each cell perpendicular to muon motion,
 365 42 mm, was chosen for a maximum drift time of 380 ns, sufficient to obviate the need
 366 for double-hit readout logic in this low-occupancy region of the detector. The height
 367 of 13 mm set by mechanical and space constraints. Track timing resolution in each
 368 SL is a few nanoseconds when all cells are allowed to read out all deposited charge.
 369 The $r\text{-}\phi$ position resolution available for online use in the trigger is about 1.5 mm in
 370 each SL; offline, for a single wire it is roughly 250 μm , leading to an overall offline
 371 resolution of 100 μm at each station.

372 **3.2.5.2 Cathode Strip Chambers**

373 Muons with $1.2 < |\eta| < 2.4$ are detected by the cathode strip chambers (CSCs).²
 374 The CSC system’s trapezoidal chambers are arranged on discs interleaved with the

²Where the CSCs and DTs overlap ($0.9 < |\eta| < 1.2$), tracks are formed from hits in both.

375 endcap yoke in four layers. Chambers close to the beamline each cover 20° sections
376 in ϕ while outer chambers cover 10° sections, with overlap to avoid gaps.

377 A CSC chamber is made of seven panels sandwiched together to make six gaps
378 filled with a gas mixture (40% Ar, 50% CO₂, 10% CF₄). Six of the plates have cathode
379 strips milled into one side, varying in pitch from 8.4 mm at the narrow end of the
380 trapezoid to 16 mm at the wide end, with 0.5 mm gaps between strips. Three panels
381 are wrapped with anode wires, alternating with the other panels so that every gas
382 gap has a plane of wires. Wires are spaced 3.2 mm apart and run azimuthally around
383 the detector, except for the innermost chamber closest to the interaction point, which
384 are inside the magnet and must have their wires tilted 29° so that charge collected
385 by the wires moves parallel to them despite the Lorentz forces from the solenoid.

386 A typical muon will deposit charge in 3–4 cathode strips and a similar number of
387 anode wires per gas gap, allowing hit position to be interpolated using all these sig-
388 nals as well as timing information. The single-plane spatial resolution can be as good
389 as 80 μm but depends strongly on where in the width of the strip the muon hits. The
390 strips in alternating planes are therefore offset by half their width. Measurements
391 from all six gas gaps in a chamber are combined into a segment with position reso-
392 lution in the 30–80 μm range, which depends on the chamber but not where in the
393 chamber the muon hit.

394 Anodes and cathodes are held 3.6 kV from each other, leading to a drift time of
395 roughly 300 ns. Single anode planes have an RMS timing resolution of around 11 ns,
396 insufficient for assigning a hit unambiguously to an individual bunch crossing, as
397 required for triggering. However, information from all six anode planes in a chamber
398 can be combined to yield a segment timing resolution around 5 ns. Segments are
399 therefore the unit of information sent to the trigger. Segment position resolution at
400 trigger level is 1–2 mm.

401 **3.2.5.3 Resistive Plate Chambers**

402 To provide a redundant set of muon momentum measurements, as well as precise
 403 timing of muon hits, CMS has six layers of resistive plate chambers (RPCs) in the
 404 barrel and four in the endcap up to $|\eta| < 1.6$. RPC chambers consist of two thin
 405 layers of inert gas (95.2% $\text{C}_2\text{H}_2\text{F}_4$, 4.5% C_4H_{10} , 0.3% SF_6) each between a pair of
 406 Bakelite electrodes held at 9.3 kV. The two “gas gaps” are placed on either side of
 407 a plane of copper strips. When a passing muon ionizes the gas, the high voltage
 408 causes a fast electron avalanche read out by the strips. The narrow gap allows the
 409 RPCs to have single-hit timing resolution around 1 ns, but the spatial resolution is
 410 limited to about 1 cm by the size of the readout strips. The DTs and CSCs both
 411 have better momentum resolution than the RPCs, but RPCs are a simple, robust
 412 auxiliary system and the timing resolution can be used in conjunction with the other
 413 systems to improve overall muon measurements. The gaps between RPC chambers
 414 do not align with the gaps in the other outer muon systems, increasing the muon
 415 spectrometer’s geometrical acceptance.

416 **3.2.6 Data Acquisition and Trigger**

417 With a bunch crossing rate of 40 MHz and over 40 collisions possible in each crossing,
 418 the collision rate can exceed 1.6 GHz. Event sizes on disk of 1–2 MB mean that the
 419 raw data generation rate of CMS could potentially be several PB/s, substantially
 420 more than can be read out, stored or analyzed with current technology. However,
 421 most events consist only of low-energy, well-understood QCD interactions, so the
 422 data rate can be drastically reduced by reading out and storing only events likely to
 423 have interesting physics content. CMS reduces the event rate with a two-level trigger
 424 system.

425 The level-1 (L1) trigger uses custom hardware operating on trigger primitives
426 (TPs) containing lower-granularity detector information to reduce the event rate to
427 100 kHz or less. The inner tracker’s readout is too slow for use in the trigger, so only
428 the calorimeters and muon systems generate TPs. Events accepted at level-1 are fully
429 read out, digitized, and sent to the high level trigger (HLT), where they are partially
430 reconstructed in software and filtered further, reducing the final rate of stored events
431 to roughly 1 kHz.

432 **3.2.6.1 Level-1 Trigger**

433 LHC beams collide at too high a rate for trigger decisions to be made in software,
434 so the L1 trigger is instead implemented in custom hardware, with processing done
435 using field-programmable gate arrays (FPGAs) as much as possible for flexibility, and
436 application-specific integrated circuits (ASICs) where required. Hardware limitations
437 of other CMS subsystems—in particular, the inner tracker’s readout speed and buffer
438 capacity—impose strict constraints on the system. The rate of events passing at
439 level-1 cannot exceed 100 kHz and the system’s overall latency cannot exceed roughly
440 $4.2 \mu\text{s}$ from the proton-proton interaction to data storage at level-1. These goals are
441 achieved while maintaining high efficiency for interesting physics events by using low-
442 granularity detector information, to reduce the bandwidth needed within the trigger
443 system. Information flows through several processing steps, with the data throughput
444 reduced at each step. Calorimeter and muon information are processed in parallel
445 and combined only in the final step. Optical links between systems provide high-
446 bandwidth data transfer and allow flexibility in the overall trigger architecture. The
447 calorimeter trigger was upgraded with respect to the Run I configuration in 2015,
448 and the whole trigger system was overhauled in 2016 [108]. Both configurations will
449 be described here.

450 Calorimeter information is compressed into TPs for use in the trigger by trigger
 451 primitive generators (TPGs). Each TP represents a “tower” consisting of a 5×5
 452 cluster of barrel or endcap ECAL crystals and the HCAL tower behind them, or a
 453 section of the HF. The TP contains an 8-bit transverse energy sum and a quality bit
 454 for each calorimeter, and six bits of error checking and bookkeeping information. In
 455 2015, TPs were sent to the Regional Calorimeter Trigger (RCT) [109], which processed
 456 18 portions of the detector (segmented in ϕ with $+\eta$ and $-\eta$ treated separately) in
 457 parallel in separate crates of electronics, using several ASICs and one FPGA in each
 458 crate for processing [110]. Each RCT crate summed the TPs with $|\eta| < 3.0$ into
 459 4×4 tower regions, and found isolated and non-isolated 2×1 tower e/γ and τ
 460 candidates. These objects were sent to Stage 1 Layer 2, which selected the best e/γ
 461 and τ candidates from the entire detector, clustered regions into 3×3 region jet
 462 candidates, and computed global quantities like missing transverse energy and the
 463 scalar sum of transverse momentum for all particles in the event. Pileup subtraction
 464 was performed with a lookup table (LUT) based on the number of regions in the
 465 detector with no energy.

466 In 2016, the whole calorimeter trigger was replaced with a new two-tiered system.
 467 Stage 2 Layer 1 (“CaloL1”) consists of 18 FPGA-based Calorimeter Trigger Proces-
 468 sor 7 (CTP7) cards [111], which calibrate and reformat the TPs before forwarding
 469 them to Stage 2 Layer 2 (“CaloL2”) [110], an FPGA-based time-multiplexed system
 470 which finds e/γ , τ , and jet candidates and computes global quantities for whole events
 471 in parallel using tower-level information.

472 In 2015, the DTs and CSCs fed track segments into track finders (DTTF [112] and
 473 CSCTF [113]) which used pattern recognition algorithms to reconstruct tracks and
 474 measure their p_T , sharing information between the track finders to avoid inefficiency
 475 in the overlap region. The RPCs made their own tracks. Since the 2016 upgrade,

476 track finding has been done by geometrical region of the detector rather than detector
 477 subsystem alone, with separate track finders for the barrel (BMTF, $|\eta| < 0.85$) using
 478 DT and RPC information [114], the endcap (EMTF, $1.25 < |\eta| < 2.4$) using CSC and
 479 RPC information [108], and the overlap region (OMTF, $0.85 < |\eta| < 1.25$) using all
 480 three muon systems [115]. The track finders feed into the Global Muon Trigger (GMT,
 481 upgraded to μ GMT in 2016) [116, 117], which merges and sorts tracks, analyzes their
 482 quality and selects the best ones.

483 The calorimeter and muon trigger systems, which have up to this point worked
 484 entirely in parallel, both send their selected candidates and global quantities to the
 485 Global Trigger (GT, upgraded to μ GT) [118, 119]. The Global Trigger contains the
 486 trigger menu, the configurable set of algorithms used to determine whether an event
 487 is accepted or not. These algorithms can use combinations of the objects from the
 488 calorimeter and muon trigger systems, including imposing topological requirements,
 489 e.g. requiring a large $\Delta\eta$ between muons in a pair. The final decision is a logical OR
 490 of all triggers in the menu, but each trigger may be prescaled, i.e. only included in
 491 the final decision a fraction of the time in order to reduce its rate. When an event is
 492 accepted, a level 1 accept (L1A) signal is sent to all CMS subsystems instructing them
 493 to read out information collected in the accepted event, which is stored in buffers until
 494 it can be read out or safely discarded. A diagram of the whole 2016 L1 trigger system
 495 and its information flow is shown in Fig. 3.11.

496 3.2.6.2 High-Level Trigger

497 After an accepted event is read out and digitized, it must undergo another level
 498 of screening before being stored. The High Level Trigger (HLT) uses full detector
 499 information reconstructed with versions of the normal CMS reconstruction algorithms
 500 specially optimized for speed, running on a large farm of commercial computers [120].

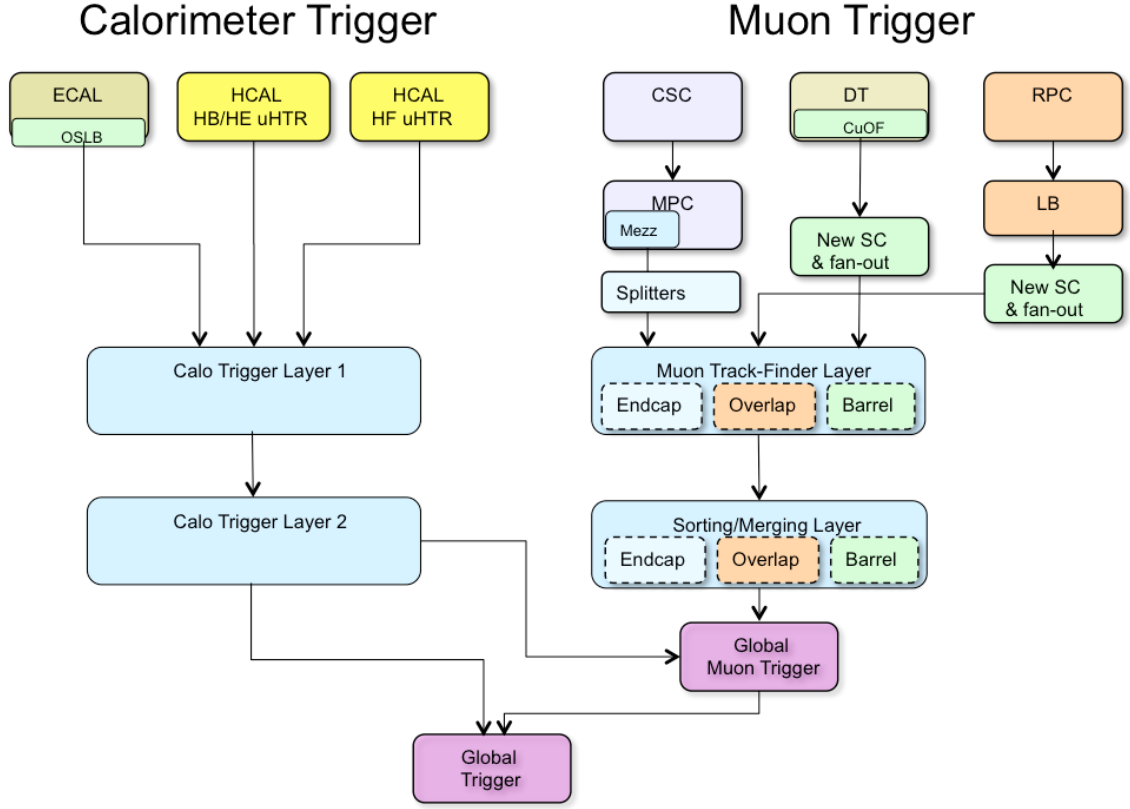


Figure 3.11: Data flow diagram for the CMS L1 trigger after the 2016 overhaul, reproduced from Ref. [108].

501 Much of HLT's power comes from having tracker information, allowing more precise
 502 momentum measurements, isolation calculations and identification algorithms than
 503 are available at L1. For example, the pixels can be used to reconstruct vertices and
 504 tag b-quark jets, and requirements can be placed on the invariant mass of a lepton
 505 pair. However, track reconstructions is slow, so it is typically only done as one of the
 506 last steps in the filtering process, allowing the event to be rejected based on more
 507 easily reconstructed objects like tracks in the muon system. Other optimizations
 508 include only reconstructing tracks near objects passed in by the L1 Global Trigger.
 509 The final result is that the rate of events saved for later analysis is around 1 kHz.

510 3.2.7 Luminosity Determination

511 A precise measurement of the luminosity delivered by the LHC is critical to precisely
 512 measuring any cross section. The instantaneous luminosity for n_b colliding bunch
 513 pairs with intensity N_b and orbit frequency f_{rev} is given by

$$\mathcal{L} = \frac{n_b N_b^2 f_{rev}}{A_{\text{eff}}} \quad (3.14)$$

514 where A_{eff} is the effective area of the beam-beam overlap. If beam i has a gaussian
 515 density profile in the u direction of width $\sigma_{i,u}$, and the beam densities are uncorrelated
 516 in each direction, then

$$A_{\text{eff}} = 2\pi\sqrt{\sigma_{1,x}^2 + \sigma_{2,x}^2}\sqrt{\sigma_{1,y}^2 + \sigma_{2,y}^2}. \quad (3.15)$$

517 The beam widths $\sigma_{i,u}$, the only unknowns in Eq. (3.14), are purely geometrical and
 518 can be found with the Van de Meer (VdM) scan method [121, 122]. In a VdM scan,
 519 for which LHC has a special run mode, one beam is held fixed while the position
 520 of the other is scanned in the x - y plane, and detector activity is measured as a
 521 function of beam displacement. Because the width of the interaction rate distribution
 522 is independent of its overall normalization, the detector activity metric may be any
 523 quantity linearly proportional to the interaction rate.

524 Over the course of an LHC run, n_b , N_b , and A_{eff} are all subject to change, and
 525 in fact the VdM scans are performed regularly, so in practice the procedure outlined
 526 above provides a calibration and overall scale for luminosity measurements during
 527 physics collisions. For a given detector metric labeled Q with rate R^Q that peaked
 528 at R_0^Q with no beam displacement, the VdM scan yields a visible cross section, the
 529 constant of proportionality between the rate and the instantaneous luminosity,

$$\sigma_{\text{vis}}^Q \equiv \frac{R^Q}{\mathcal{L}} = \frac{A_{\text{eff}} R_0^Q}{f_{rev}}. \quad (3.16)$$

530 CMS has several such metrics; the primary one used for measuring integrated lumi-
 531 nosity is the number of pixel hit clusters [123, 124]. The instantaneous luminosity is
 532 given by

$$\mathcal{L} = \frac{\langle N_c \rangle f_{rev}}{\sigma_{\text{vis}}^{\text{PCC}}} = \frac{\langle N_c \rangle f_{rev}}{A_{\text{eff}} \langle N_c \rangle_0} \quad (3.17)$$

533 where $\langle N_c \rangle = R^{\text{PCC}} / f_{rev}$ is the average number of pixel hit clusters at each bunch
 534 crossing and $\langle N_c \rangle_0$ is its peak value during the VdM scan.

535 A number of complications must be accounted for or included in systematic un-
 536 certainty estimates. Beam-beam interation effects, correlations between the proton
 537 density distributions in the x and y directions, drifts in the beam orbit, and nor-
 538 malization uncertainties on the bunch intensity and absolute distance scale from the
 539 beam spot must all be handled with care. The result is a total integrated luminosity
 540 uncertainty of 2.3% in 2015 [123] and 2.5% in 2016 [124].

⁰ Chapter 4

¹ Simulation

² Comparing data collected by CMS to theoretical predictions is a complex task. The
³ theories described in Chapter 1 are understood in great detail, but using this knowl-
⁴ edge to calculate observables is a nontrivial enterprise. Once calculated, observables
⁵ must be compared to data from a detector with finite resolution and subject to a
⁶ number of experimental effects that do not exist in the rarefied world of quantum
⁷ field theory. The general strategy is to employ numerical simulations of individual
⁸ collision events that involve a physics process of interest, and apply accurate simu-
⁹ lations of the detector’s response to these events to obtain samples that are directly
¹⁰ comparable to data. The success of all steps in this process at a high-luminosity
¹¹ hadron collider is one of the triumphs of the LHC era, with many observables in
¹² interesting processes simulated accurately to the level of a few percent.

¹³ 4.1 Monte Carlo Event Generation

¹⁴ Even in trivial cases, it would be impossible to integrate over the phase space of hard
¹⁵ scattering outcomes determined from theory, convolved with matter interactions, de-

16 tector effects, and other experimental factors, to calculate observables analytically.
 17 Particle interactions are well-understood on a microscopic scale, but it is extremely
 18 difficult to extrapolate from this first-principles understanding to a description of the
 19 macroscopic behavior of an ensemble of particles as needed to make predictions about
 20 fundamentally stochastic processes. Observable spectra are therefore modeled with
 21 the Monte Carlo (MC) method [39, 125], a numerical integration technique so named
 22 because, like a casino, it relies heavily on random numbers¹. The scattering ampli-
 23 tudes for a process are calculated from theory at a chosen perturbative order, and
 24 for each simulated event a configuration of final state particles is selected at random
 25 from this phase space. The final state particles are propagated through decays, radia-
 26 tion, hadronization, and interaction with other matter—such as the detector—based
 27 on well-understood physics principles, and the outcome of any stochastic process is
 28 chosen at random from a realistic set or distribution of possibilities. In the limit of
 29 a large number of simulated events, the distributions from the simulated detector
 30 will converge to be directly comparable to aggregated data. Individual steps in this
 31 process are detailed in the following sections.

32 **4.1.1 Matrix Element and Hard Process Generation**

33 Event generator programs start by calculating the scattering amplitudes for a pro-
 34 cess at a chosen order in perturbation theory. For example, the generator MAD-
 35 GRAPH5_AMC@NLO [127] generates all the relevant Feynman diagrams up to NLO
 36 and calculates the matrix elements for them. Others, like POWHEG [128–130], SHER-
 37 PA [131] and MCFM [53, 132, 133], are not fully general but have a broad range of
 38 physics processes implemented at NLO; SHERPA and MCFM can do some calculations

¹Pseudorandom numbers are actually used, but there is no difference in practice as long as a good pseudorandom number generator (PRNG) is chosen and seeded properly. The Mersenne Twister algorithm [126] is the modern standard among general-purpose PRNGs in physics and elsewhere.

39 at NNLO [134]. Events are generated across the entire allowed phase space, either
40 uniformly or with the specific distribution dictated by one of several “importance
41 sampling” techniques [39, 135] which ensure appropriate statistical coverage in re-
42 gions where the distribution has a large slope or value. Each event is assigned a
43 weight $w \in (0, 1)$ based on the scattering amplitude in that region of phase space and
44 the probability of having an appropriate initial state based on the PDFs discussed in
45 Section 1.6. The sample is then “unweighted” to a subset that is directly comparable
46 to data by removing events with a probability proportional to $1 - w$.

47 **4.1.2 Parton Shower, Hadronization, and Underlying Event**

48 **4.1.3 Pileup Simulation**

49 **4.2 Detector Simulation**

0 Chapter 5

1 Object Reconstruction and 2 Selection

3 The raw detector information stored on disk after an event passes trigger selections
4 is not yet suitable for physics analysis. Hits in the tracker and muon systems, and
5 energy deposits in the calorimeters, require significant processing to build physics
6 objects that are interpretable in terms of the physics of the hard scatter. Patterns in
7 the tracker and muon system hits are found and used to construct charged particle
8 and muon tracks, and energy deposits in the calorimeters are grouped into clusters.
9 Final state particles that interact with CMS are reconstructed from the tracks and
10 calorimeter clusters, final state particles are clustered into jets, charged particles are
11 clustered by track origin to find proton-proton collision vertices, and visible particle
12 momenta are summed to find the transverse momentum imbalance from undetectable
13 particles (in the SM, neutrinos). The resulting physics objects undergo selection to
14 determine which represent real particles of interest for the analysis. Selected particles
15 are used to reconstruct the hard interaction from the collision—in the analyses pre-
16 sented here, leptons are paired to form Z/γ^* boson candidates which may be paired

17 to form Higgs or Z boson candidates or nonresonant ZZ candidates, and jets are
 18 used to construct hadronic observables and to distinguish electroweak and QCD ZZ
 19 production.

20 **5.1 Track Reconstruction and Vertex
 21 Identification**

22 Tracks are reconstructed in the inner tracker by iterative application of a combina-
 23 torial Kalman filter algorithm [136–139]. At each iteration, tracks found in the pixel
 24 detector are used as “seeds”, track segments which serve as the initial trajectories on
 25 which strip tracker hits from the same particle are expected. The pixel seed supplies
 26 the initial parameters for the combinatorial Kalman filter. At each tracker layer, the
 27 algorithm predicts where the particle will hit the next layer based on the track’s cur-
 28 rent parameters, taking into account the effects of particle interaction with tracker
 29 material. The extrapolated trajectory is used to find compatible hits in the next layer
 30 with a χ^2 test, and if possible the most compatible hit is added to the track and its
 31 parameters are updated accordingly. If no hits are compatible, a “ghost” hit which
 32 does not contribute to the track parameters may be added to account for the possibil-
 33 ity of a missing hit in the corresponding layer. This procedure is repeated recursively
 34 at each tracker layer, from the innermost layer past the seed to the outermost layer
 35 of the silicon strip tracker. If two tracks found in an iteration share too many hits,
 36 they are assumed to be from the same particle and the one with fewer hits is rejected,
 37 using the total χ^2 of all hits as a tiebreaker. The first iterations of the track finding
 38 algorithm searches for high- p_T tracks from primary proton-proton interactions, which
 39 are easier to find because they are close to straight and originate from the beam line.
 40 When a track is found, its constituent hits are removed from consideration in future

41 iterations, reducing the computational complexity of finding the more difficult tracks
 42 from lower- p_T particles and products of b hadron decays which happen away from
 43 the beam line.

44 Because the Kalman filter obtains the final track parameters only at the out-
 45 ermost tracker layer, each track is refit and smoothed with further Kalman filters,
 46 improving track quality and reducing fake rate. Spurious tracks are rejected from the
 47 final collection with requirements on the number of layers hit, the χ^2 of the fit, and
 48 compatibility with a primary vertex.LHC The efficiency for reconstructing tracks of
 49 all prompt charged particles with $p_T > 900$ MeV is around 94% in the barrel and
 50 85% in the endcap; for isolated muons, it is virtually 100% in the whole tracker
 51 acceptance [139].

52 Electrons lose substantially more energy to interactions with the tracker material
 53 than other charged particles, often breaking the assumption of Gaussian energy loss
 54 inherent to the Kalman filter. To mitigate the impact of the resulting poor track
 55 fits, tracks with many missing hits or a poor χ^2 are refit using a Gaussian sum filter
 56 (GSF) [140]. Any Kalman filter or GSF tracks with trajectories that intersect ECAL
 57 energy clusters (see below) are considered electron track candidates and refit with a
 58 second, more complicated GSF. This GSF track collection is used as inputs to the
 59 PF electron reconstruction described below.

60 Proton-proton interaction vertices are found by clustering tracks by minimizing
 61 the figure of merit

$$\chi^2 = \sum_i \sum_j p_{ij} \frac{(z_j^t - z_i^V)^2}{\sigma_j^2}, \quad (5.1)$$

62 where z_i^V is the z position of vertex i , z_j^t is the z position of track j at its closest
 63 point to the beamline, and σ_j^2 is its uncertainty. The track-vertex association matrix
 64 p_{ij} maps tracks to their associated vertices, i.e. $p_{ij} = 1$ if vertex i and track j are
 65 associated, $p_{ij} = 0$ if they are not. Rather than minimize Eq. (5.1) directly with an

66 unknown number of vertices, the CMS clustering algorithm [139, 141] uses a tech-
 67 nique known as deterministic annealing [142], which treats the system as a statistical
 68 ensemble of associations between the tracks and an unknown number of vertices. The
 69 association matrix p_{ij} is then the probability that vertex i and track j are associated.
 70 If every possible set of assignments, for every possible number and arrangement of
 71 vertices, is considered equally probably, this is analogous to a thermodynamic system
 72 at high temperature, with χ^2 playing the role of energy. The system is simulated at
 73 high “temperature” and the analog of free energy is minimized to determine p_{ij} . The
 74 temperature is then lowered in steps, with track-vertex associations deterministic in
 75 the limit of zero temperature.

76 Among the interaction vertices in an event, the one whose associated charged
 77 particles have the highest sum of p_T^2 is labeled the primary vertex (PV). A PV must be
 78 less than 24 cm from the nominal beam spot in the z direction and less than 2 cm from
 79 the beamline. Many commonly-used analysis observables are strongly dependent on
 80 the number of secondary proton-proton interaction vertices in the event, colloquially
 81 called the pileup. The pileup distribution used in Monte Carlo samples are not the
 82 same as the distribution in data, biasing sensitive quantities. Monte Carlo events are
 83 therefore reweighted based on the number of simulated pileup vertices such that the
 84 overall N_{vtx} (number of proton-proton interaction vertices) distributions match.

85 5.2 Particle Flow Reconstruction

86 The simplest conceivable algorithm would reconstruct each type of particle mostly
 87 with information from single subsystems: muons with the outer muon system, elec-
 88 trons and photons with ECAL, jets with the calorimeters aided by inner tracker
 89 information to handle b jet vertexing, etc. This approach is sufficient for many anal-

90 yses and sophisticated versions of the general principle have performed admirably at a
 91 number of experiments, but it is suboptimal. It fails to exploit the full detector infor-
 92 mation for many objects—for example, not using the inner tracker’s precise measure-
 93 ments of low-energy charged hadrons in jets made by clustering calorimeter deposits—
 94 and misses significant correlations between detector systems. The CMS collaboration
 95 takes a different approach, using a particle flow (PF) algorithm combining subde-
 96 tector signals for optimal particle reconstruction and identification [**CMS:2009nxa**,
 97 143, 144].

98 Several features of CMS facilitate PF reconstruction, as described in Section 3.2.
 99 The most important is that the calorimeters are inside the magnet and close to the
 100 tracker, so charged particles are much less likely to interact with material between
 101 them. The inner tracker’s precise position measurement and ECAL’s fine segmen-
 102 tation thus allow tracks to be associated to calorimeter clusters even for individual
 103 charged hadrons of modest energy.

104 **5.2.1 PF Candidates**

105 The inputs to the PF algorithm are inner tracker tracks, muon system tracks, and
 106 clusters of energy deposits in the calorimeters, all of which are calibrated beforehand.
 107 Calorimeter clusters are built independently for each subsystem, with ECAL and
 108 HCAL barrel and endcaps considered separately. Topological clusters are built by
 109 combining adjacent cells with energy deposits over a threshold, using cells that are
 110 local energy maxima as seeds. Within the topological clusters, the final calorime-
 111 ter clusters are built by fitting the energy deposits with the sum of several two-
 112 dimensional Gaussians, one Gaussian for each seed in the topological cluster.

113 The first step of the PF algorithm is to link tracks and clusters across subdetec-
 114 tors. Tracks are linked to calorimeter clusters by extrapolating from the track to the

115 calorimeter cells the particle would be expected to hit. To account for bremsstrahlung
 116 photons from electron interactions with tracker material, GSF tracks are linked with
 117 ECAL clusters compatible with a tangent to the track where it hit the tracker. Over-
 118 lapping ECAL and HCAL clusters are linked outside the inner tracker acceptance.
 119 Inner tracks are linked to muon system tracks if they are compatible with each other
 120 within the resolution of the muon system. The groups of linked objects, called “PF
 121 blocks”, usually originate from one or a few particles and are the basic unit of PF
 122 reconstruction.

123 **5.2.1.1 Muons**

124 Muon candidates in CMS [145] come in three flavors: “standalone”, “tracker”, and
 125 “global” muons. Standalone muons use only the track from the muon spectrometer
 126 (the “standalone track”), built with a fit to track segments made of clusters of hits in
 127 the DTs, CSCs, and RPCs. Tracker muons use only the inner track, identified as a
 128 muon because the track is compatible with one or more track segments in the muon
 129 system. Global muons use a combined “global track” made by fitting the hits in an
 130 inner track and a compatible standalone track to a common muon trajectory through
 131 the whole detector. By construction, global muons have corresponding standalone
 132 and tracker muons. The inner track typically dominates the global track fit, so
 133 the corresponding tracker muon is merged with the global muon. When a muon
 134 candidate is reconstructed, its constituent tracks are removed from the PF block and
 135 are therefore not used in further reconstruction.

136 **5.2.1.2 Electrons and Prompt Photons**

137 Electron reconstruction uses GSF tracks linked with ECAL clusters [140, 146]. The
 138 cluster associated to a track and the bremsstrahlung candidate clusters on tangents to

139 the track are collectively called the “supercluster”. Prompt photons are reconstructed
 140 from superclusters without associated tracks except displaced track pairs consistent
 141 with photon-initiated electron-positron pair production in the tracker material [147].
 142 In both cases, the HCAL energy near the supercluster cannot be more than 10% of the
 143 supercluster energy. Non-isolated photons, i.e. those with substantial nearby tracks
 144 or calorimeter deposits or a ratio of ECAL and HCAL energy incompatible with a
 145 photon, as assumed to be from π^0 decays and are described with neutral hadrons in
 146 the next section. Tracks and clusters used to reconstruct electrons and photons are
 147 removed from the PF block and are not used in hadron reconstruction.

148 5.2.1.3 Charged and Neutral Hadrons

149 With muon, electron, and prompt photon constituents removed, remaining detector
 150 signals are taken to be from charged and neutral hadrons (including non-prompt
 151 photons) [CMS:2009nxa, 144]. Clusters in ECAL without associated tracks are
 152 taken to be photons from π^0 decays, because neutral hadrons deposit very little
 153 energy in ECAL. Trackless clusters in HCAL are taken to be neutral hadrons. Both
 154 are removed from the PF blocks, so all that remain are linked clusters and tracks.
 155 Paired tracks and clusters with compatible energies are taken to be charged hadrons.
 156 If the track p_T is much less than the calorimeter-measured p_T , the pair is labeled as
 157 overlapping charged and neutral hadrons.

158 5.2.2 Jets

159 Effective clustering of hadrons, non-prompt photons, and non-prompt leptons into jets
 160 is critically important for many physics analyses, including the ZZ + jets differential
 161 cross section measurements and the ZZ VBS search. Clustering must be efficient, to
 162 ensure the tagging jets in VBS events are found, but the clustering algorithm should

163 not tag spurious jets, as the number of jets in an event is sensitive to higher-order QCD
164 corrections and therefore an interesting quantity to compare to theoretical predictions.
165 Similarly, the algorithm should not erroneously cluster particles from the same initial
166 parton into multiple jets or merge jets from multiple original partons, because the
167 kinematics of the original quarks and gluons are also of theoretical interest and the
168 detector-level jet kinematics should accurately reflect them. A clustering algorithm
169 is said to be “infrared safe” if the presence of low-energy hadrons from soft gluon
170 radiation does not change the number of jets or have a qualitatively significant effect
171 on jet shapes and kinematics. This fits with the intuition that a single 1 GeV pion
172 should have essentially no effect in an event with multiple jets with energies on the
173 order of hundreds of GeV [148]. An algorithm is said to be “collinear safe” if the
174 jets are not changed substantially by splitting one hadron into two nearly collinear
175 hadrons with the same total four-momentum. This also fits with physical intuition in
176 that jets deposit energy over an area significantly larger than the spatial resolution of
177 the detector, so increasing the detector granularity enough to resolve two very close
178 particles (without changing their total four-momentum) should have little or no effect
179 on the jet.

180 Infrared and collinear (IRC) safety are critically important for comparing data
181 to theoretical predictions [149]. Collinear splittings and soft gluon radiation during
182 jet fragmentation should not affect the dynamics of the TeV-scale hard scattering
183 processes we wish to probe, but they are nonperturbative and difficult to model, and
184 experimental analysis can only probe the underlying hard interaction if it is insensitive
185 to this kind of mismodeling. Experimental detectors’ finite resolution and inability to
186 measure arbitrarily soft particles enforces some level of IRC safety on any algorithm,
187 but the results of an analysis methods that uses an IRC unsafe clustering will depend
188 on the complex, detector-dependent details of this partial IRC regularization. In any

189 case, the most meaningful comparisons between data and theory should use the same
 190 definition of a jet in the experimental analysis and the perturbative calculation, and
 191 perturbative calculations require IRC safe observables to preserve unitarity.

192 These considerations, and the desire for conical jets with a well-defined area in
 193 the $\eta\text{-}\phi$ plane, lead most CMS analyses (including this one) to use jets clustered with
 194 the anti- k_{T} algorithm [150, 151]. The anti- k_{T} algorithm defines the distance between
 195 two particles i and j as

$$d_{ij} = \min(p_{\text{T}i}^{-2}, p_{\text{T}j}^{-2}) \frac{\Delta_{ij}}{R}, \quad (5.2)$$

196 where Δ_{ij} is the distance in the rapidity-polar angle plane,

$$\Delta_{ij}^2 \equiv (y_i - y_j)^2 + (\phi_i - \phi_j)^2, \quad (5.3)$$

197 and R is a parameter setting the size of the resulting jets. The algorithm proceeds
 198 iteratively. At each iteration, if the smallest d_{ij} between any pair of particles in the
 199 event is smaller than the smallest p_{T}^{-2} of any single particle, the particles in the pair
 200 are merged into a single particle with their total four-momentum. If the minimum
 201 single-particle p_{T}^{-2} is smaller than the minimum d_{ij} , the single particle is labeled a
 202 jet and removed from further consideration. Iteration proceeds until all particles are
 203 part of a jet. In this analysis, the size parameter used is $R = 0.4$.

204 Charged hadrons from pileup interactions are not included in jet clustering [152].
 205 The contribution of neutral hadrons from pileup is estimated with a jet area tech-
 206 nique [153–155] in which the energy density of neutral hadrons from pileup is cal-
 207 culated event-by-event and multiplied by the area of the jet to estimate the neutral
 208 pileup contribution, which is subtracted from the jet energy. Jets in Monte Carlo
 209 samples have their energy shifted and stochastically smeared such that the overall
 210 energy scale and resolution match that of jets in data [153, 156].

211 5.2.3 Missing Transverse Energy

212 Neutrinos—or, hypothetically, WIMP dark matter or other new particles that do not
 213 decay or interact directly with the detector—escape and cannot be directly measured.
 214 Because the beams have no momentum in the x - y plane, the transverse momentum
 215 of the visible particles must balance the transverse momentum of the invisible ones.
 216 The missing transverse momentum is thus

$$\vec{p}_T^{\text{miss}} = - \sum_{\text{visible}} \vec{p}_T, \quad (5.4)$$

217 where the sum runs over the transverse momenta of all PF candidates in the event.
 218 The missing transverse energy, E_T^{miss} , is its magnitude. The E_T^{miss} is calibrated by
 219 propagating the jet energy scale corrections to the E_T^{miss} calculation [157–159]. PF
 220 candidates originating from pileup interactions are included in the sum in Eq. (5.4)
 221 because these soft collisions are very unlikely to produce neutrinos, so including them
 222 biases the measurement less than trying to determine which neutral particles should
 223 be considered pileup and which should not.

224 5.3 Object Identification and Selection

225 The reconstruction algorithms described above are general purpose in the sense that
 226 they can be used in nearly any analysis, but do not address the specific needs of
 227 any, so further selections are essentially always required to optimize object efficiency
 228 and purity for studying a specific physics process. The leptons used in this analysis
 229 are required to pass identification requirements on top of those imposed during PF
 230 reconstruction, and are required to be isolated from other particles in the event, to
 231 reject fake objects from jet fragmentation. Four-lepton processes have low reducible
 232 backgrounds, so the selections presented here are generally loose, optimized for high

233 efficiency compared to most CMS analyses.

234 5.3.1 Electrons

235 Electrons are required to have $p_T > 7\text{ GeV}$ and to be in the tracker acceptance,
 236 $|\eta| < 2.5$. They must be compatible with the PV, with minimum track-PV distance
 237 $d_z < 1\text{ cm}$ in the z direction and $d_{xy} < 5\text{ mm}$ in the plane transverse to the beam.
 238 Each electron's 3-dimensional impact parameter (IP) d_{3D} must satisfy a requirement
 239 on its significance,

$$\text{SIP}_{3D} \equiv \frac{d_{3D}}{\sigma_{d_{3D}}}, \quad (5.5)$$

240 where $\sigma_{d_{3D}}$ is the uncertainty on the IP. The SIP_{3D} requirement is $\text{SIP}_{3D} < 10$ for
 241 the ZZ and $Z \rightarrow 4\ell$ cross section measurements and the aTGC search, and $\text{SIP}_{3D} < 4$
 242 for the Higgs boson measurement and the VBS and aQGC searches. To remove fake
 243 electrons arising from muon tracks being associated to photons or other incidental
 244 ECAL energy clusters, electrons within $\Delta R < 0.05$ of a muon are vetoed.

245 To further reduce photon and jet fragment backgrounds while maintaining high
 246 prompt electron efficiency, a further selection is applied using a multivariate discrim-
 247 inator made with a boosted decision tree (BDT) [160, 161]. The BDT uses 21 input
 248 variables, which fall into three broad categories:

- 249 • Track-related observables like the number of hits and normalized χ^2 of the
 250 Kalman and GSF tracks and the energy lost to bremsstrahlung according to
 251 the GSF fit. These are intended to discriminate between electrons and charged
 252 hadrons.
- 253 • Calorimetric information including a number of supercluster shape observables
 254 and the amount of HCAL energy near the supercluster, to discriminate electrons
 255 from electromagnetically rich jets.

256 • Track-cluster observables comparing the positions and momenta of the particles
 257 seen in the tracker and by ECAL.

258 The BDT training and working point selection are done separately for electron can-
 259 didates with p_T above and below 10 GeV and in three bins of $|\eta|$ (0–0.8, 0.8–1.479,
 260 and 1.479–2.5). The working points are chosen to correspond to 98% efficiency for
 261 single signal electrons in each bin.

262 To ensure that electron candidates are not part of a jet, they are required to be
 263 isolated from other particles in the event. The relative isolation is defined as

$$R_{\text{Iso}} = \left(\sum_{\text{charged}} p_T + \max \left[0, \sum_{\text{neutral}} p_T + \sum_{\text{photons}} p_T - p_T^{\text{PU}}(\ell) \right] \right) / p_T^\ell \quad (5.6)$$

264 where the sums run over the p_T of PF hadrons and photons in a cone of $\Delta R < 0.3$
 265 around the electron trajectory. To mitigate the contribution of pileup to the isolation
 266 calculations, charged hadrons are included only if they originate from the event’s PV.
 267 The estimated neutral contribution to isolation from pileup, $p_T^{\text{PU}}(\ell)$, is defined for
 268 electrons as

$$p_T^{\text{PU}}(e) \equiv \rho \times A_{\text{eff}}, \quad (5.7)$$

269 where the average transverse-momentum flow density ρ is calculated in each event
 270 using the jet area method described above. The effective area A_{eff} is the geometric
 271 area of the isolation cone times an η -dependent correction factor that accounts for
 272 the residual dependence of the isolation on pileup. Electrons are considered isolated
 273 if their relative isolations satisfy $R_{\text{iso}} < 0.35$.

274 Efficiencies for GSF track reconstruction, electron reconstruction and identifica-
 275 tion, and electron isolation criteria, are found with a “tag-and-probe” method [162].
 276 In this technique, events are selected which contain at least one high- p_T “tag” electron
 277 passing strict ID and isolation requirements, and a “probe” track with the opposite
 278 sign that combines with the electron to have an invariant mass close to the Z boson

mass. The resulting sample is enriched with $Z \rightarrow e^+e^-$ events, so the track is likely to correspond to a real prompt electron. Unlike all background processes, $Z \rightarrow e^+e^-$ production forms a distinct resonance peak in the $m_{\ell\ell}$ distribution, so shape fits can be used to find the overall purity of the sample, and thus the number of prompt electrons among the probes. The selection efficiency is then the number of passing probes divided by the total number of prompt probes. This procedure is performed in bins of p_T and η for data and Monte Carlo events, and residual differences in efficiency in Monte Carlo samples are corrected to match data by weighting events by the ratio of data and Monte Carlo efficiency for each electron candidate.

5.3.2 Muons

Muon selection is similar to electron selection, but simpler because muon backgrounds are much smaller. Candidate muons are required to be tracker or global muons with $p_T > 5$ GeV within the muon system acceptance ($|\eta| < 2.4$). They are subject to the same PV compatibility criteria as electrons, $d_z < 1$ cm, $d_{xy} < 5$ mm, and $SIP_{3D} < 10$ or 4 depending on the analysis. Muon candidates are further subject to the so-called “PF ID” criteria, which require them to be isolated from calorimeter deposits or to have high-quality tracks with good fits [144].

Isolation is defined as in Eq. (5.6), the same as for electrons except for the definition of the neutral pileup contribution, which for muons is based on using the known charged pileup density to estimate the neutral pileup based on the average charge composition of pileup jets,

$$p_T^{\text{PU}}(\mu) \equiv 0.5 \sum_{\text{charged}} p_T^{\text{PU}}, \quad (5.8)$$

where the sum runs over the charged particles from all pileup vertices. As for electrons, the radius of the isolation cone is 0.3 in the $\eta\phi$ plane and the selection criterion

302 is $R_{\text{iso}} < 0.35$. Muon efficiencies are measured and corrected with the same tag-and-
 303 probe technique as used for electrons.

304 5.3.3 Final State Photon Radiation

305 Final-state radiation (FSR) photons emitted by muons are not included in the PF
 306 momentum reconstruction, and some photons emitted by electrons may be missed,
 307 degrading Z boson reconstruction. Photons are considered FSR candidates if they
 308 have $p_T > 2 \text{ GeV}$, $|\eta| < 2.4$, relative isolation $R_{\text{iso}} < 1.8$ as defined in Eq. (5.6) (with
 309 no neutral pileup correction), and $\Delta R(\ell, \gamma) < 0.5$ with respect to the nearest lepton.
 310 To avoid double counting, photons in electron superclusters are not considered. Be-
 311 cause FSR has a higher energy spectrum than photons from pileup and is expected
 312 to be quasi-collinear with the emitting leptons, a photon is accepted as FSR and
 313 included in the ZZ final state if $\Delta R(\ell, \gamma) / E_{T\gamma}^2 < 0.012$. FSR photons are omitted
 314 from the isolation determination for emitting leptons. In the rest of this thesis, the
 315 momentum of any FSR photons found is included in Z/ γ^* and ZZ four-momenta
 316 unless otherwise stated.

317 5.3.4 Jets

318 Jets are considered for analysis if they have $p_T > 30 \text{ GeV}$ and $|\eta| < 4.7$. Loose criteria
 319 are applied to reject spurious jets by requiring they contain multiple particles, and
 320 the particles be a mix of charged and neutral consistent with hadronic jets. Jets are
 321 removed from consideration in the event if a lepton or FSR photon is in its cone
 322 ($\Delta R < 0.4$ with respect to the jet's total momentum vector).

323 5.3.5 Misidentified Objects

324 The reducible background estimation method described in Section 6.1 requires the use
 325 of “loose” lepton candidates which are similar to candidates passing the full selection
 326 but much more likely to be jet fragments or other non-prompt objects. Loose lepton
 327 candidates pass the p_T and η cuts and vertex compatibility criteria, but the other
 328 identification criteria are reduced. The electron BDT discriminator is not applied to
 329 loose electrons. Loose muons must still be tracker or global muons, but the PF ID is
 330 not applied. Isolation requirements are not applied to loose candidates. Depending
 331 on their use, loose candidates may have no further requirements applied, or may be
 332 required to fail the tight ID and/or isolation requirements, as detailed in Section 6.1.
 333 Aside from the ID and isolation criteria, loose leptons are treated the same as their
 334 tight cousins, with FSR recovery performed with the same algorithm. Jets near loose
 335 leptons are only removed if the loose lepton is taken to be one of the four in the ZZ
 336 candidate in the final event interpretation.

337 5.4 ZZ Candidate and Event Selection

338 Online event selections used single, double, and triple lepton triggers. The double
 339 lepton triggers were the primary paths, with single and triple lepton triggers correct-
 340 ing for residual inefficiencies to bring the overall trigger efficiency above 99%. Exact
 341 HLT parameters changed over the course of datataking as instantaneous luminosities
 342 changed and trigger rates rose, so many thresholds are shown here as ranges.

- 343 • Single muon p_T thresholds were between 20 and 24 GeV for isolated muons.
 344 Nonisolated single muons were required to have $p_T > 50$ GeV or $p_T > 45$ GeV
 345 and $|\eta| < 2.1$. Single electron p_T thresholds were 25 or 27 GeV depending on
 346 ID criteria applied.

- 347 • Leading lepton p_T thresholds in double lepton paths were 17 or 23 GeV. Trail-
 348 ing lepton thresholds were 12 GeV and 8 GeV for electrons and muons, respec-
 349 tively. Isolation requirements and requirements on the z -axis distance between
 350 lepton track origins were added part way through datataking.
- 351 • The p_T requirements in triple lepton paths varied between 5 and 16 GeV, with
 352 no isolation or vertex requirements.

353 An event is considered for the analysis if any of these triggers fires.

354 Several distinct analyses fall under the four-lepton umbrella, each with different
 355 requirements and therefore different selection criteria. The sets of selections will be
 356 listed here with brief descriptions of their uses, and detailed in full below.

- 357 • The *full spectrum selection* picks a phase space that encompasses all four-lepton
 358 events, and all other selection sets yield strict subsets of the full spectrum phase
 359 space.
- 360 • The *singly resonant ($Z \rightarrow 4\ell$) selection* picks events with four-lepton mass
 361 around the Z boson resonance.
- 362 • The *Higgs selection* is that used for the Higgs boson discovery and properties
 363 measurements. It is similar to the full spectrum selection but with slightly
 364 tighter requirements on the second Z/γ^* candidate, because $Z \rightarrow 4\ell$ events are
 365 of less interest and some backgrounds may be reduced by excluding events with
 366 an on-shell Z boson and a low mass lepton pair that could be a decay of an Υ
 367 or similar meson.
- 368 • The *on-shell or doubly resonant* selection requires both Z candidates to be
 369 compatible with a resonant Z boson. It is used for the ZZ and ZZ + jets cross
 370 section measurements and the aTGC search.

- 371 • The *dijet (ZZjj) selection* uses the on-shell selection for the four-lepton system,
 372 and additionally requires at least two jets. It is used for the VBS and aQGC
 373 searches.

374 **5.4.1 Z/γ^* Candidate Selection**

375 A Z/γ^* candidate is built from a pair of opposite-sign, same-flavor leptons with
 376 invariant mass between 4 and 120 GeV. The Z/γ^* candidate with mass closest to the
 377 nominal Z boson mass is labeled Z_1 , the other is labeled Z_2 . Mass requirements on
 378 the Z/γ^* candidates are among the primary differences between the various analysis
 379 selections. The full spectrum, $Z \rightarrow 4\ell$, and Higgs selections require $m_{Z_1} > 40$ GeV.
 380 The Higgs selection additionally requires $m_{Z_2} > 12$ GeV. The on-shell and dijet
 381 selections require both Z_1 and Z_2 to have $m_{Z_i} > 60$ GeV. The mass range thus
 382 allowed, $60 < m_{Z_{1,2}} < 120$ GeV, serves as the definition of an on-shell Z boson for
 383 purposes of this analysis.

384 **5.4.2 ZZ Candidate Selection**

385 Four-lepton candidates are built from pairs of Z/γ^* candidates. Among the four lep-
 386 tons in the candidate, all opposite-sign pairs must have invariant mass $m_{\ell^+\ell'^-} > 4$ GeV
 387 regardless of flavor, to remove events in which decay products of a light, leptonically
 388 decaying particle like a J/ψ are erroneously paired with the two leptons from a real Z
 389 boson to form two false Z/γ^* candidates by chance when paired incorrectly. The re-
 390 quirement on all pairs does not include FSR photons, because the mesons that would
 391 cause such a problem are generally found in jets which include photons from π^0 decays,
 392 whcih are likely to be misidentified as FSR. All lepton pairs must have $\Delta R > 0.02$
 393 to avoid “ghost” leptons with shared tracks. The leading and lepton among the four

394 must have $p_T > 20 \text{ GeV}$, and the subleading lepton must have $p_T > 10 \text{ GeV}$ if it is
 395 an electron or $p_T > 12 \text{ GeV}$ if it is an electron. The $Z \rightarrow 4\ell$ selection requires the
 396 candidate to have $80 < m_{4\ell} < 100 \text{ GeV}$, consistent with resonant single-Z production.

397 All allowed pairings of leptons into Z/γ^* candidates are examined separately, so
 398 an event with two electrons and two positrons, for example, will yield two possible
 399 ZZ candidates, with the only difference being how the electrons are paired into Z_1
 400 and Z_2 . In the case that multiple interpretations of the same event pass the full
 401 selection, the one with Z_1 closest to the nominal Z mass is chosen. In the rare case of
 402 further ambiguity, which may arise in events with five or more leptons, Z_2 is chosen
 403 to maximize the scalar p_T sum of the four leptons. This best candidate selection is
 404 done after the full selection is applied, and the other analysis selections are applied to
 405 the disambiguated events in the full spectrum phase space. Like the mass cut on all
 406 opposite-sign lepton pairs, this prevents events with one on-shell Z and one lower-mass
 407 γ^* from passing the on-shell Z mass cuts with an erroneous lepton pairing.

408 5.4.3 Dijet and VBS Signal Selection

409 The dijet selection, used for the VBS and aQGC searches, requires the event to contain
 410 two or more jets. The two highest- p_T jets are called the “tagging jets.” The tagging
 411 dijet system must have $m_{jj} > 100 \text{ GeV}$. This criterion is not intended to preferentially
 412 select the EWK signal, which is concentrated at much higher dijet masses, but rather
 413 to provide a minimal selection for the sample on which to perform the multivariate
 414 VBS analysis described in Section 6.5 and the shape-based aQGC analysis described
 415 in Section 6.6.

⁰ Chapter 6

¹ Analysis Strategy

² 6.1 Background Estimation

3 Reducible backgrounds for four-lepton events typically have two or three prompt
 4 leptons and two or one other objects—typically jet fragments, sometimes photons—
 5 which are misidentified as prompt leptons. The largest source of background contam-
 6 ination is from events in which a Z boson is produced in association with a photon
 7 and a jet, a leptonically-decaying W boson and a jet, or two jets. There is also a
 8 contribution from $t\bar{t}$ events in which both top quarks decay to a lepton, a neutrino,
 9 and a b quark jet. For simplicity, the two sets of processes are not treated separately
 10 in what follows, and are collectively labeled “Z + X” events¹.

11 The contributions of the reducible backgrounds to the selected four-lepton sig-
 12 nal samples are evaluated using the tight-to-loose “fake rates” method, described in
 13 Ref. [163]. In this procedure, the likelihood of a nonprompt (“fake”) object to be
 14 misidentified as a prompt lepton is estimated and applied to control regions enriched
 15 with Z + X events to estimate their contribution to the signal region. The lepton

¹This is a bit of a misnomer, as “Z + X” does not accurately describe $t\bar{t}$ events, but the terminology is retained here for consistency with the CMS papers on these analyses.

16 misidentification rate $f_\ell(p_T^\ell, \eta^\ell)$ is measured from a sample of $Z + \ell_{\text{fake}}$ events, where
 17 the Z boson candidate is selected as in the signal region but with $|m_{\ell\ell} - m_Z| < 10 \text{ GeV}$,
 18 and the ℓ_{fake} object is a lepton candidate that passes relaxed ID requirements as de-
 19 fined in Section 5.3.5, with no isolation or tight ID requirements applied.

20 The misidentification rate is defined as the fraction of ℓ_{fake} candidates which pass
 21 full lepton identification and isolation criteria, in bins of p_T and η . One should note
 22 that the misidentification rate cannot be interpreted as a probability in the usual
 23 sense, and in fact there is no simple physical interpretation of it. Events with three
 24 prompt leptons can contaminate this control region and bias the misidentification
 25 rate, because the non- Z lepton is falsely assumed fake. To mitigate this bias, the
 26 $WZ \rightarrow 3\ell\nu$ yields in the numerator and denominator in each bin are estimated from
 27 a simulated sample and subtracted before the ratio of yields is taken. Figure 6.1
 28 shows the misidentification rates for electrons and muons separately as a function of
 29 p_T and η .

30 To estimate the total reducible background yield, the misidentification rates are
 31 applied to two $Z + X$ enriched control samples, each containing a Z boson candidate
 32 passing all signal region requirements plus two more lepton candidates which pass the
 33 relaxed identification criteria and would make a second Z boson candidate according
 34 to Section 5.4.1 except that one or both fail the full identification or isolation criteria.
 35 The sample with one failing lepton, called the “3P1F” sample for “3 prompt 1 fake,”
 36 covers the contribution from WZ events, while the sample with both leptons in the
 37 second Z boson failing (“2P2F”) covers $Z + \text{jets}$ and $t\bar{t}$ events. The fake object transfer
 38 factor

$$F_\ell(p_T^\ell, \eta^\ell) = \frac{f_\ell(p_T^\ell, \eta^\ell)}{1 - f_\ell(p_T^\ell, \eta^\ell)} \quad (6.1)$$

39 is the ratio of nonprompt objects passing the relaxed and full selection criteria, and
 40 thus serves as a per-lepton extrapolation factor between control sample yields and

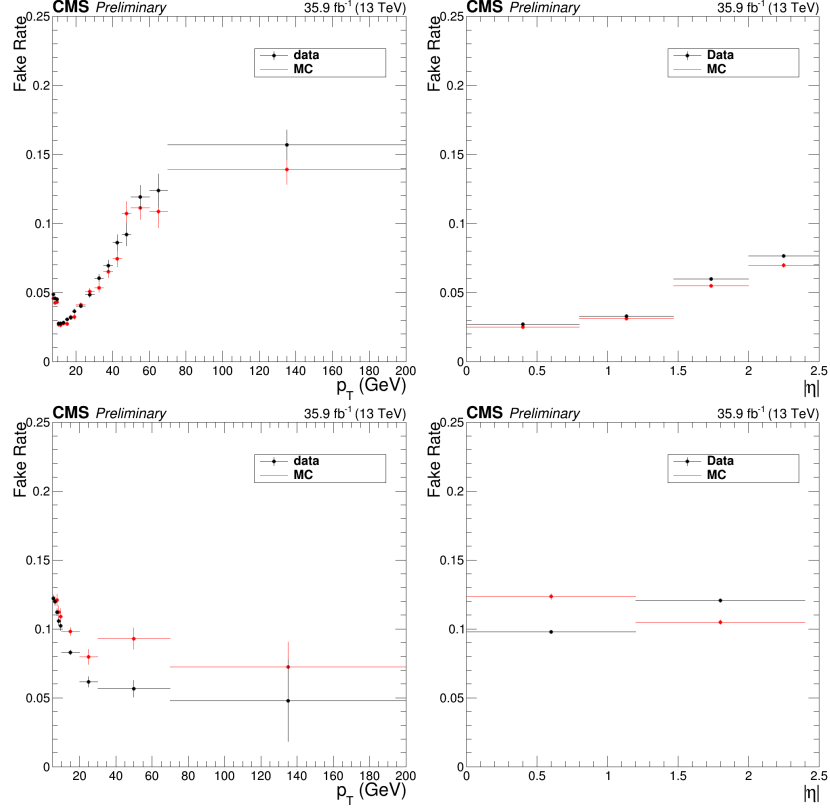


Figure 6.1: Fake rate for electrons (top) and muons (bottom) as a function of p_T (left) and η (right).

41 signal sample yields.

42 The total reducible background yield is thus

$$N_{\text{bkg}} = \sum_{\ell \in 3\text{P1F}} F_\ell(p_T^\ell, \eta^\ell) - \sum_{\ell_1, \ell_2 \in 2\text{P2F}} F_{\ell_1}(p_T^{\ell_1}, \eta^{\ell_1}) F_{\ell_2}(p_T^{\ell_2}, \eta^{\ell_2}). \quad (6.2)$$

43 The minus sign prevents double-counting of Z+2jets events in which one jet fragment
 44 is misidentified. The failing lepton candidates in the 3P1F and 2P2F control samples
 45 are assumed to truly be jet fragments or other nonprompt objects, but selection
 46 inefficiencies may cause prompt leptons to fail and contaminate the control regions
 47 with signal events. The yield of such signal events in the background control regions is
 48 estimated by applying the same fake factors to failing events in the ZZ signal Monte
 49 Carlo samples, and subtracted from the result of Eq. (6.2).

50 There are also irreducible background contributions from $t\bar{t}Z$ and WWZ events,
 51 which can have four prompt leptons. Expected yields for these processes are taken
 52 from simulation.

53 6.2 Systematic Uncertainties

54 Systematic uncertainties for trigger efficiency are taken to be the difference between
 55 trigger efficiencies in data and in simulated signal events, found to be around 2%
 56 of the final event yield. Because leptons in $Z \rightarrow 4\ell$ events generally have lower p_T ,
 57 the uncertainty increases to 4% for $Z \rightarrow 4e$ events. In both data and simulated
 58 events, trigger efficiencies are found with a tag-and-probe technique [162], performed
 59 on four-lepton events.

60 The lepton identification and isolation efficiencies in simulation are corrected with
 61 scaling factors derived with the tag-and-probe method, performed on $Z \rightarrow \ell^+\ell^-$ events
 62 in data and a single-Z Monte Carlo sample. To find the uncertainties associated with
 63 these corrections, the total yield is recomputed with the scaling factors varied up and
 64 down by one standard deviation of the uncertainties from the tag-and-probe method,
 65 treating all bins as correlated. The resulting changes in the $ZZ \rightarrow 4\ell$ yield, taken to
 66 be the one sigma variations resulting from lepton efficiency uncertainties, are found
 67 to be 6% in the 4e final state, 3% in the 2e2 μ final state, and 2% in the 4 μ final state.
 68 Leptons in $Z \rightarrow 4\ell$ events tend to have lower p_T , and the tag-and-probe samples
 69 for leptons with p_T below about 15 GeV are smaller and more contaminated with
 70 nonprompt objects, so the uncertainties are larger; they are found to be 10%, 6%,
 71 and 7% for the 4e, 2e μ , and 4 μ final states, respectively.

72 The uncertainty on the integrated luminosity of the data sample is 2.5% [124].

73 The uncertainty on lepton fake rates is 40%, which includes both statistical un-

74 certainty and systematic uncertainties associated with the loosened lepton selections
 75 defined in Section 5.3.5 and the differences in the underlying physics processes be-
 76 tween events in the $Z + \ell_{\text{fake}}$, 3P1F, and 2P2F control samples [55]. Statistical uncer-
 77 tainties arising from the limited size of the $Z + X$ control samples are also included
 78 as a systematic uncertainty on the background yield. The total uncertainty on the
 79 background yield varies by channel but is below 1% of the expected total yield.

80 Uncertainties due to the effect of QCD scale on the $ZZ \rightarrow 4\ell$ acceptance are
 81 evaluated with POWHEG and MCFM, by varying the QCD scales up and down by a
 82 factor of two with respect to the default $\mu_R = \mu_F = m_{ZZ}$. Parametric uncertainties
 83 ($\text{PDF} + \alpha_s$) are evaluated according to the PDF4LHC prescription in the acceptance
 84 calculation [164], and with NNPDF3.0 in the cross section calculations. An additional
 85 theoretical uncertainty arises from scaling the $q\bar{q} \rightarrow ZZ$ and $gg \rightarrow ZZ$ simulated
 86 samples to their NNLO and NLO predicted cross sections, respectively, as described
 87 in Chapter 4. The corresponding change in the acceptance, 1.1%, is added to the
 88 previous theoretical errors in quadrature.

89 Systematic uncertainties on expected signal yield are summarized in Table 6.1. To
 90 obtain uncertainties in the inclusive cross sections, each uncertainty source is treated
 91 as a nuisance parameter in the fits described in Section 6.3.1. For differential cross
 92 section and other shape uncertainties, the calculation is fully redone for each uncer-
 93 tainty source, with the inputs shifted by one standard deviation in each direction.
 94 Variations across bins are taken to be fully correlated for each uncertainty source.
 95 Lepton and jet momentum scale and resolution uncertainties are taken to be trivial
 96 for the overall yield, but they are considered among the shape uncertainties.

Table 6.1: The contributions of each source of signal systematic uncertainty in the total yields. The integrated luminosity uncertainty and the PDF and scale uncertainties are considered separately. All other uncertainties are added in quadrature into a single systematic uncertainty. Uncertainties that vary by decay channel are listed as a range.

Uncertainty	$Z \rightarrow 4\ell$	$ZZ \rightarrow 4\ell$
Lepton efficiency	6–10%	2–6%
Trigger efficiency	2–4%	2%
MC statistics	1–2%	0.5%
Background	0.6–1.3%	0.5–1%
Pileup	1–2%	1%
PDF	1%	1%
QCD Scales	1%	1%
Integrated luminosity	2.5%	2.5%

97 6.3 Fiducial and Total Cross Section Calculation

98 Inclusive cross section measurements can be treated as simple binned counting experiments,
99 where the bins are the three decay channels ($4e$, $2e2\mu$, and 4μ). If ν events are
100 expected in a given bin, the probability of observing n events is given by the Poisson
101 distribution,

$$f(n; \nu) = e^{-\nu} \frac{\nu^n}{n!}. \quad (6.3)$$

102 In a particle physics analysis like this one, ν takes the form

$$\nu = \nu_s(\vec{\theta}_s) + \nu_b(\vec{\theta}_b) = \mu(\vec{\theta}_s) \mathcal{L}_{int} \sigma_{SM} \epsilon + \nu_b(\vec{\theta}_b) \quad (6.4)$$

103 where ν_s and ν_b are respectively the expected signal and background yields, σ_{SM} is
104 the standard model expectation for the cross section of the signal process and ϵ is our
105 efficiency for detecting and identifying its events. The signal and background nuisance
106 parameter vectors $\vec{\theta}_s$ and $\vec{\theta}_b$ represent hidden quantities that we do not measure
107 directly but which affect our yields, i.e. systematic effects. The signal strength μ

108 compares our expectation to what we actually measure:

$$\mu = \frac{\sigma_{meas}}{\sigma_{SM}}. \quad (6.5)$$

109 Of the variables in Eqs. (6.3) and (6.4), σ_{SM} is known from theoretical calculations,
 110 and ϵ is determined from simulation. The CMS detector is designed to measure n
 111 and \mathcal{L}_{int} , ν_b is estimated from data or simulation, and inferring σ_{meas} is a matter of
 112 finding the most likely value of the signal strength μ given the observed data. Then
 113 the measured cross section is simply

$$\sigma_{meas} = \mu \sigma_{SM}. \quad (6.6)$$

114 One interesting feature of this method is that σ_{SM} is used in the calculation of μ
 115 (Eq. (6.4)) and in the final cross section (Eq. (6.6)) in such a way that it cancels out,
 116 and in fact anything proportional to the true cross section may be used. In practice,
 117 this means that the order at which σ_{SM} is calculated does not matter to the extent
 118 that higher order corrections to the kinematics of the events do not affect ϵ .

119 Typically, σ_{meas} in Eq. (6.6) is the fiducial cross section, the cross section for the
 120 process in a phase space similar to (typically, slightly larger than) the phase space
 121 in which the experimental analysis can in principle detect events. In the four-lepton
 122 case, the fiducial phase space is a space of $2\ell 2\ell'$ ($\ell, \ell' \in e, \mu$) events defined by criteria
 123 on lepton kinematics, dilepton invariant masses, and four-lepton mass. Table 6.2
 124 shows the fiducial definitions for both the $Z \rightarrow 4\ell$ and $ZZ \rightarrow 4\ell$ cross section mea-
 125 surements. Lepton kinematic requirements and an invariant mass requirement on
 126 all opposite-sign, same-flavor lepton pairs in the event are common to both mea-
 127 surements; requirements on the invariant masses of Z/γ^* boson candidates and the
 128 four-lepton system are different.

129 The total ZZ cross section is defined subject to no constraints except the require-
 130 ment that m_{Z_1} and m_{Z_2} be between 60 and 120 GeV, which serves as the definition

131 of a Z boson. The fiducial cross section is related to the total cross section by the
 132 branching fraction \mathcal{B} to the final state in question—here, two factors of the Z/γ^*
 133 branching ratio to electron and muon pairs—and an acceptance factor \mathcal{A} which is the
 134 fraction of events falling in the fiducial phase space,

$$\sigma_{fid} = \mathcal{A}\sigma_{tot} (\mathcal{B}(Z \rightarrow 2\ell))^2. \quad (6.7)$$

135 The acceptance factor \mathcal{A} is determined entirely from theory, and is well known [39], so
 136 it is straightforward to calculate the total cross section once the fiducial cross section
 137 is known. Calculating both fiducial and total cross sections is interesting because
 138 it effectively factorizes experimental and theoretical uncertainties. The experimental
 139 uncertainties are contained entirely in the uncertainties on ϵ , \mathcal{L}_{int} , and ν_b in Eq. (6.4),
 140 which have little or no dependence on theory, while the theoretical uncertainties are
 141 contained entirely in the uncertainty on \mathcal{A} , which is determined with no experimental
 142 input. Thus the uncertainty on σ_{fid} is entirely experimental, and the theoretical
 143 uncertainties enter only in the uncertainty on σ_{tot} .

Table 6.2: Fiducial phase space definitions for the $Z \rightarrow 4\ell$ and $ZZ \rightarrow 4\ell$ cross section measurements. The common requirements apply to both. The $m_{\ell^+\ell'^-}$ criterion is applied to all opposite-sign same-flavor lepton pairs in the event.

Measurement	Fiducial requirements
Common	$p_T^{\ell_1} > 20 \text{ GeV}$, $p_T^{\ell_2} > 10 \text{ GeV}$, $p_T^{\ell_{3,4}} > 5 \text{ GeV}$, $ \eta^\ell < 2.5$, $m_{\ell^+\ell'^-} > 4 \text{ GeV}$
$Z \rightarrow 4\ell$	$m_{Z_1} > 40 \text{ GeV}$, $80 < m_{4\ell} < 100 \text{ GeV}$
$ZZ \rightarrow 4\ell$	$60 < m_{Z_1}, m_{Z_2} < 120 \text{ GeV}$

¹⁴⁴ **6.3.1 Signal Strength Extraction**

¹⁴⁵ The signal strength is found by the method of maximum likelihood [39, 165]. The
¹⁴⁶ likelihood function is the product of the probability distributions across all bins,

$$L \left(\vec{\theta}_s, \vec{\theta}_b \right) = \prod_{bins} f \left(n; \nu \left(\vec{\theta}_s, \vec{\theta}_b \right) \right). \quad (6.8)$$

¹⁴⁷ The most likely value of ν is the one that maximizes L . In practice, $\log L$ is typically
¹⁴⁸ maximized instead because it is easier to work with,

$$\frac{\partial^2 \log L}{\partial \vec{\theta}_s \partial \vec{\theta}_b} = 0. \quad (6.9)$$

¹⁴⁹ This maximization is performed simultaneously for all bins, yielding a single signal
¹⁵⁰ strength across all channels. Systematic uncertainties enter as log-normal constraints
¹⁵¹ imposed on the fit, encoded in $\vec{\theta}_s$ and $\vec{\theta}_b$. The fit is performed numerically.

¹⁵² **6.3.2 $Z \rightarrow 4\ell$ Branching Fraction**

¹⁵³ The total Z cross section can be calculated from the $Z \rightarrow 4\ell$ fiducial cross section
¹⁵⁴ with Eq. (6.7), but it is better measured in the 2ℓ channel, where the larger branching
¹⁵⁵ fraction yields samples several orders of magnitude larger than the $Z \rightarrow 4\ell$ sample
¹⁵⁶ used here. It is therefore more interesting to use $\sigma_{fid}(Z \rightarrow 4\ell)$ for a measurement of the
¹⁵⁷ four-lepton branching fraction $\mathcal{B}(Z \rightarrow 4\ell)$. After applying the acceptance correction
¹⁵⁸ to obtain $\sigma_{tot}(Z \rightarrow 4\ell) = \sigma_{fid}(Z \rightarrow 4\ell) / \mathcal{A}$, the four-lepton branching fraction is given
¹⁵⁹ by

$$\mathcal{B}(Z \rightarrow 4\ell) = \frac{\sigma_{tot}(Z \rightarrow 4\ell)}{\mathcal{C}_{80-100}^{60-120} \sigma(Z \rightarrow 2\ell)} \mathcal{B}(Z \rightarrow 2\ell), \quad (6.10)$$

¹⁶⁰ where $\sigma(Z \rightarrow 2\ell)$ is the dileptonic Z cross section in the 60–120 GeV mass range and
¹⁶¹ $\mathcal{C}_{80-100}^{60-120}$ corrects for the fact that $\sigma(Z \rightarrow 4\ell)$ is found in a mass range of 80–100 GeV.

162 6.4 Differential Cross Sections

163 Measurement of a differential fiducial cross section is also a problem of finding the
164 most likely true distribution given observed yields in multiple bins, estimated back-
165 ground yields, and detector effects understood through simulation. Unlike the inclu-
166 sive cross section, however, finite detector resolution leads to “smearing” effects that
167 cause events to migrate across bins, in addition to the same inefficiencies. The mean
168 detector-level distribution $\vec{\delta}$ is related to the true distribution $\vec{\theta}$ by a response matrix
169 \mathbf{R} :

$$\vec{\delta} = \mathbf{R}\vec{\theta}. \quad (6.11)$$

170 The observed distribution in data \vec{d} is sampled from the Poisson distribution with
171 mean $\vec{\delta}$ independently in each bin. CMS simulation software is sufficiently sophis-
172 ticated to give a good estimate of R , reproducing the real detector’s resolution and
173 smearing effects at the level of a few per cent or better for all distributions of interest.

174 If \mathbf{R} is square and invertible, the maximum likelihood estimate (MLE) of the true
175 distribution, $\hat{\vec{\theta}}$, is given by

$$\hat{\vec{\theta}} = \mathbf{R}^{-1}\vec{d}. \quad (6.12)$$

176 Even when \mathbf{R} is invertible, however, it is frequently ill-conditioned, giving $\hat{\vec{\theta}}$ unphysical
177 features like large bin-by-bin fluctuations or even negative bins as a consequence of the
178 stochastic nature of \vec{d} . It is therefore necessary to use a more sophisticated procedure
179 to ensure the differential cross section distributions obey physics-inspired constraints.

180 The variables used for differential cross sections in this analysis are in general well-
181 measured, so bin-to-bin fluctuations are small and the response matrices are nearly
182 diagonal, but some bins have low occupancy which can still cause pathologies.

183 **6.4.1 Unfolding**

184 The technique used here is an iterative frequentist method developed in high energy
 185 physics by D'Agostini [166] and independently in other fields [167–170], as imple-
 186 mented in ROOUNFOLD [171]. At iteration k , bin j of the predicted true distribution
 187 is set based on its expected contribution to all other bins, weighted by the observed
 188 data yield in each:

$$\begin{aligned}\theta_j^{(k+1)} &= \sum_i \mathbf{R}_{ij} \theta_j^{(k)} \frac{d_i}{\delta_i} \\ &= \sum_i \mathbf{R}_{ij} \theta_j^{(k)} \frac{d_i}{\sum_m \mathbf{R}_{im} \theta_m^{(k)}}.\end{aligned}\tag{6.13}$$

189 After several iterations, $\vec{\theta}^{(k)}$ depends only weakly on the ansatz $\vec{\theta}^{(0)}$.

190 The sequence will converge to the MLE for any non-pathological choice of $\vec{\theta}^{(0)}$ [172]
 191 but again the MLE often displays unphysical behavior. If $\vec{\theta}^{(0)}$ is strictly positive, $\vec{\theta}^{(k)}$
 192 will be strictly positive for all k , and in this case $\hat{\vec{\theta}}$ (as defined in Eq. (6.12)) will be
 193 the asymptotic unfolded distribution as long as it is also strictly positive. Choosing a
 194 smooth function for $\vec{\theta}^{(0)}$ will generally lead to smooth $\vec{\theta}^{(k)}$ for small k ; typical choices
 195 include a flat initial distribution and the truth-level distribution used to construct \mathbf{R}
 196 (used in this analysis). What constitutes “small” k depends on the condition of \mathbf{R} ,
 197 but for most physics distributions of interest, including all those used in this analysis,
 198 nonphysical fluctuations do not arise until after $\vec{\theta}^{(k)}$ is close to convergence. Full
 199 regularization is therefore imposed by ceasing iteration early. For all distributions
 200 shown here, stopping after four iterations was found to obtain a result close to the
 201 asymptotic distribution without artificially increasing the bin-to-bin variance.

202 **6.4.2 Uncertainties**

203 The largest uncertainties in the unfolded distributions arise from the unfolding pro-
 204 cedure itself, which can inflate statistical uncertainties present in the detector-level
 205 distributions. The correlation matrix which gives the full uncertainty—considered
 206 the statistical uncertainty of the unfolded distribution—does not have a closed form
 207 due to the nonlinearity of the method. The covariance matrix is therefore estimated
 208 by propagating the statistical error of the inputs at each iteration of the method, as
 209 laid out in Ref. [166] and improved in Ref. [171]. This procedure does not account for
 210 the bias introduced by regularization, but this is expected to be negligible relative to
 211 other systematic uncertainties for the well-modeled processes studied here.

212 Most systematic uncertainties are propagated through unfolding by recomputing
 213 the response matrix with the training sample shifted or reweighted to reflect a 1σ
 214 shift in the quantity in question. The uncertainty related to that quantity is taken
 215 to be the resulting shape difference in the final unfolded distribution. Systematic
 216 uncertainties are negligible compared to statistical uncertainties in most bins.

217 **6.5 VBS Signal Extraction**

218 The VBS signal search considers events passing the selections described in Sec-
 219 tion 5.4.3. The electroweak yield is insufficient to have sensitivity at 35.9 fb^{-1} , even
 220 with further cut optimization, so a gradient-boosted decision tree (GBDT), imple-
 221 mented with the SCIKIT-LEARN package [173], is used to extract the signal. Hyper-
 222 parameters of the GBDT are optimized with a grid search. Each Monte Carlo sample
 223 used in the VBS search (c.f. Chapter 4) is split into a “training” subsample, used to
 224 train the GBDT, and a “test” subsample used to evaluate its performance and make
 225 templates for use in the statistical analysis. The GBDT performance is nearly the

226 same for the test and training samples, a sign that the algorithm is not overtrained.

227 A number of observables have been proposed to discriminate VBS events from
 228 background [41], of which m_{jj} and $\Delta\eta_{jj}$ are the most powerful. Other commonly-used
 229 variables include $m_{4\ell}$, $\eta^{j_1} \times \eta^{j_2}$, $\Delta\phi_{Z_1 Z_2}$, and the so-called Zeppenfeld variables, defined
 230 as

$$\eta_P^* = \eta_P - \frac{\eta_{j_1} - \eta_{j_2}}{2}, \quad (6.14)$$

231 where P may stand for Z_1 , Z_2 , or j_3 , the highest- p_T untagged jet in the event. In ad-
 232 dition to these “traditional” quantities, several other groups of observables have been
 233 examined, including production angles, decay angles, measures of total hadronic ac-
 234 tivity in the event, properties of individual leptons and jets and of the ZZjj system, and
 235 a discriminator designed to distinguish jets originating from quarks and gluons [174].

236 The hadronic activity and quark-gluon tagging variables have some discriminating
 237 power, but they differ significantly depending on the Monte Carlo generator used
 238 and were therefore considered too poorly-modeled to use. New GBDTs were trained,
 239 each with the traditional observables and one other group of observables, and the
 240 groups that improved the GBDT discrimination power significantly were retained.
 241 This procedure yielded 17 observables, including the hard process relative transverse
 242 momentum, defined as the ratio of the p_T of the ZZjj system to the scalar sum of the
 243 p_T of each object,

$$p_T^{rel. hard} = \frac{p_T^{ZZjj}}{\sum_{Z_1, Z_2, j_1, j_2} p_T}, \quad (6.15)$$

244 and the dijet relative transverse momentum,

$$p_T^{rel. jj} = \frac{p_T^{jj}}{\sum_{j_1, j_2} p_T}. \quad (6.16)$$

245 The list of observables was further optimized by retraining the GBDT once with
 246 each variable dropped and eliminating the one with the least discriminating power.
 247 This pruning was repeated until seven observables remained, namely m_{jj} , $\Delta\eta_{jj}$, $m_{4\ell}$,

248 $\eta_{Z_1}^*$, $\eta_{Z_2}^*$, $p_T^{rel.\ hard}$, and $p_T^{rel.\ jj}$. The resulting GBDT performs only marginally worse
 249 (0.2 σ less expected significance on the VBS signal) than a version with all observables
 250 included, and is faster and easier to train, simpler, and less susceptible to biases and
 251 systematic uncertainties from mismodeling.

252 The signal and background yields are extracted from the GBDT output spectrum
 253 with a binned maximum likelihood fit to templates from the test Monte Carlo samples.
 254 To obtain templates with better fit convergence properties, the GBDT output is
 255 mapped to the range [0, 1] with the logistic transformation

$$x \rightarrow \frac{1}{1 - e^{-x}}. \quad (6.17)$$

256 This provides better separation between signal and background and allows uniform
 257 binning in the templates.

258 6.6 Anomalous Gauge Coupling Searches

259 The new physics represented by aGCs would generally manifest as an increase in
 260 events with high invariant mass, so it is natural to use the shape of the $m_{4\ell}$ distribution
 261 for the search. For the aTGC search, the doubly on-shell ZZ selection is used, while
 262 the aQGC search is performed with the ZZjj selection described in Section 5.4.3.

263 Monte Carlo samples with nonzero aTGCs are generated at grids of points in the
 264 $f_4^Z-f_4^\gamma$ and $f_5^Z-f_5^\gamma$ planes. In each bin of the $m_{4\ell}$ distribution, the yields at the various
 265 working points are fit to a function of the form

$$y(f^Z, f^\gamma) = x_0 + x_1 f^Z + x_2 f^\gamma + x_3 f^Z f^\gamma + x_4 (f^Z)^2 + x_5 (f^\gamma)^2 \quad (6.18)$$

266 where $y(f^Z, f^\gamma)$ is the yield in the bin, f^V can be f_4^Z and f_4^γ or f_5^Z and f_5^γ , and x_i
 267 are the parameters to be fit.

268 A similar procedure is performed for the aQGC search. Rather than simulating a
 269 full sample for each working point, which is computationally expensive, events from
 270 `MADGRAPH5_AMC` produced at LO are used to obtain samples for nonzero values
 271 of f_{T0}/Λ^4 , f_{T1}/Λ^4 , f_{T2}/Λ^4 , f_{T8}/Λ^4 , and f_{T9}/Λ^4 by matrix element reweighting [127].
 272 The yields in each $m_{4\ell}$ bin are fit to parabolas as a function of the five aQGC param-
 273 eters separately.

274 A binned profile likelihood method [39] is used to derive the limits. Systematic
 275 uncertainties are taken into account by varying the number of signal and background
 276 events within their uncertainties. Exclusion limits are found by comparing the p-
 277 values of the signal hypothesis and the background only hypothesis

$$CL_s = \frac{p_{s+b}}{1 - p_b} \quad (6.19)$$

278 to set thresholds. Further details on the method can be found in Ref. [175]. The
 279 software for setting limits, implemented with `RooStats`, has been validated and
 280 used extensively by the CMS and ATLAS collaborations [176].

⁰ Chapter 7

¹ Results

2 A number of measurements and analyses fall under the umbrella of four-lepton
3 physics, and results presented in this thesis were originally made public in several
4 journal articles and Physics Analysis Summary documents released by the CMS col-
5 laboration. The first CMS measurement of the ZZ inclusive cross section at 13 TeV
6 used roughly half the 2015 dataset (1.34 fb^{-1}) and was made public in Ref. [177] in
7 December 2015 as one of the first measurements done on 13 TeV collision data. That
8 analysis was expanded to use the whole 2.6 fb^{-1} collected in 2015, and to include
9 the $Z \rightarrow 4\ell$ branching fraction measurement, as reported in Ref. [178], submitted in
10 July 2016 and published the following December. With the full 2016 dataset, the ZZ
11 cross section and $Z \rightarrow 4\ell$ branching ratio were measured again to greater precision in
12 Ref. [61], which also included differential cross section measurements and aTGC lim-
13 its, made public in March 2017. An upcoming paper including these measurements
14 will also include a combination of the 2015 and 2016 inclusive cross section measure-
15 ments. Differential cross sections with respect to jet-related observables, and searches
16 for EWK ZZ production and aTGCs, were reported in May 2017 in Ref. [179], which
17 will be split into two papers—one for the cross section measurements, one for the

18 searches—for final journal publication. The Higgs boson was studied in the four-
 19 lepton final state in Refs. [180–182]. In the following, results for each topic are only
 20 shown for 2016 data, which are taken to supersede 2015 data.

21 **7.1 Four-Lepton Yield and Distributions**

22 **7.1.1 Full Spectrum**

23 The full four-lepton invariant mass spectrum is shown in Fig. 7.1. The single-Z
 24 resonance can be seen below 100 GeV, the Higgs resonance is visible—though it is
 25 not sharply resolved with this binning—in the Z/γ^* region below $2m_Z$, where doubly
 26 resonant ZZ continuum production begins. The dilepton invariant mass spectrum is
 27 shown for both Z/γ^* candidates in Fig. 7.2 and for the Z/γ^* candidate closest to the
 28 nominal Z boson mass (Z_1) in Fig. 7.3. Figure 7.4 shows m_{Z_2} plotted against m_{Z_1}
 29 for data events representative of all four-lepton production. Clusters of events with
 30 zero ($Z \rightarrow 4\ell$ and nonresonant $\gamma^*\gamma^*$ production), one ($H \rightarrow ZZ^*$ and nonresonant $Z\gamma^*$
 31 production), and two (nonresonant ZZ production) on-shell Z bosons can be clearly
 32 seen.

33 **7.1.2 $Z \rightarrow 4\ell$ Resonance**

34 Expected and observed yields for events satisfying the $Z \rightarrow 4\ell$ selection criteria
 35 ($80 < m_{4\ell} < 100$ GeV) are shown in Table 7.1. The invariant mass distribution of
 36 these events is shown in Fig. 7.5. Figure 7.6 shows m_{Z_2} plotted against m_{Z_1} for
 37 all data events consistent with $Z \rightarrow 4\ell$ production. Predictions from Monte Carlo
 38 samples generally agree well with the data.

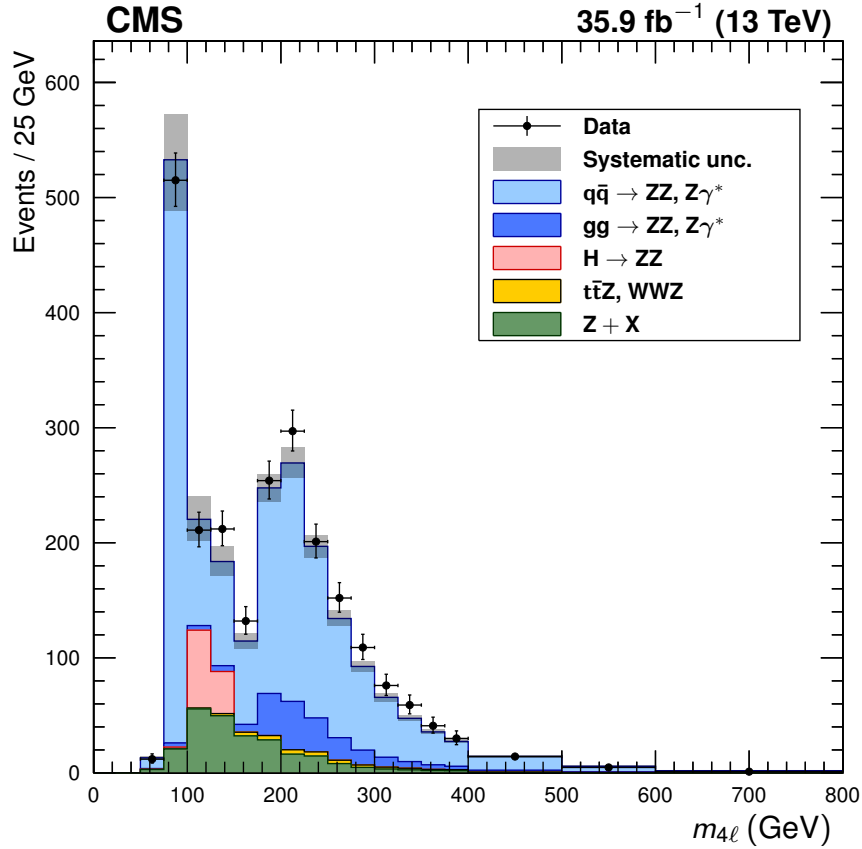


Figure 7.1: Distribution of the four-lepton invariant mass $m_{4\ell}$ of all events in the full spectrum selection. Points represent data, with statistical uncertainty bars. The stack of filled histograms represents the SM signal prediction and background estimate, with a grey band showing the sum in quadrature of the statistical and systematic uncertainties on the total expected yield.

Table 7.1: Observed and expected yields of $Z \rightarrow 4\ell$ events, including expected background yields, shown for each final state and summed to the total. Uncertainties are statistical, then systematic, not including the integrated luminosity uncertainty.

Final state	Expected $N_{4\ell}$	Background	Total expected	Observed
4μ	$224 \pm 1 \pm 16$	$7 \pm 1 \pm 2$	$231 \pm 2 \pm 17$	225
$2e2\mu$	$207 \pm 1 \pm 14$	$9 \pm 1 \pm 2$	$216 \pm 2 \pm 14$	206
4e	$68 \pm 1 \pm 8$	$4 \pm 1 \pm 2$	$72 \pm 1 \pm 8$	78
Total	$499 \pm 2 \pm 32$	$19 \pm 2 \pm 5$	$518 \pm 3 \pm 33$	509

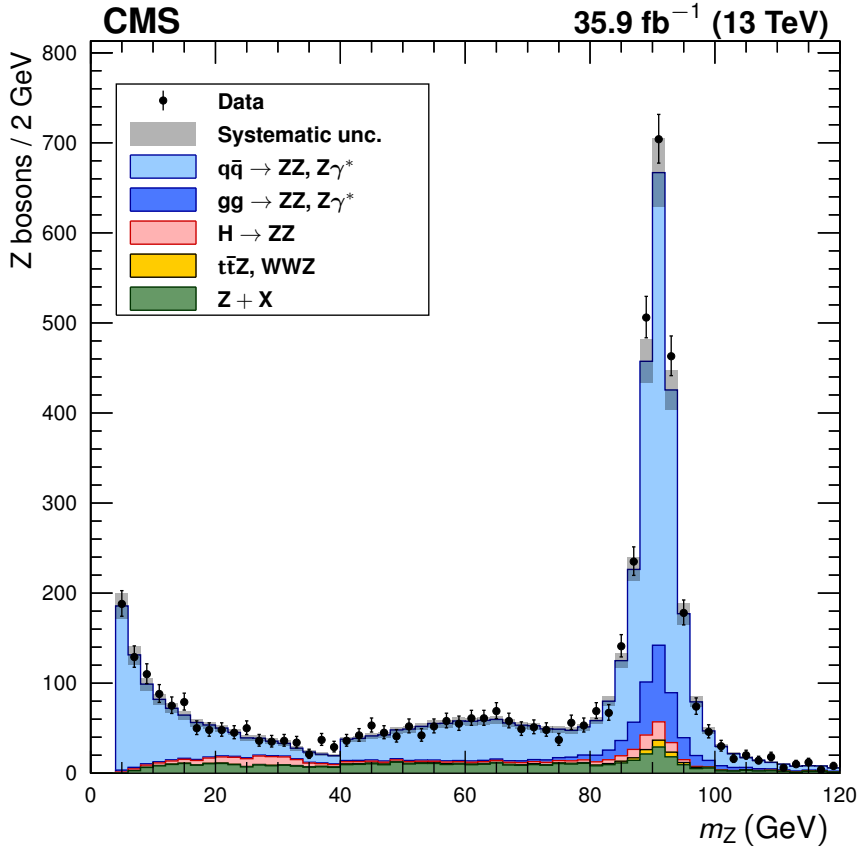


Figure 7.2: Distribution of the dilepton invariant mass of Z/γ^* candidates in all events in the full spectrum selection, regardless of whether the lepton pair is labeled Z_1 or Z_2 . Points represent data, with statistical uncertainty bars. The stack of filled histograms represents the SM signal prediction and background estimate, with a grey band showing the sum in quadrature of the statistical and systematic uncertainties on the total expected yield.

³⁹ 7.1.3 Higgs Resonance

⁴⁰ Figure 7.7 shows the four-lepton invariant mass around the Higgs resonance, which
⁴¹ can be clearly seen above the SM continuum background, for events passing the Higgs
⁴² selection ($m_{Z_2} > 12 \text{ GeV}$, $\text{SIP}_{3D} < 4$ for all leptons). Table 7.2 shows the observed
⁴³ and expected yields in the mass range $118 < m_{4\ell} < 130 \text{ GeV}$. Here, SM continuum
⁴⁴ production—considered signal in all other parts of this analysis—is considered back-
⁴⁵ ground. Figures 7.8–7.10 show the Z_1 mass, the Z_2 mass, and the scatter plot of

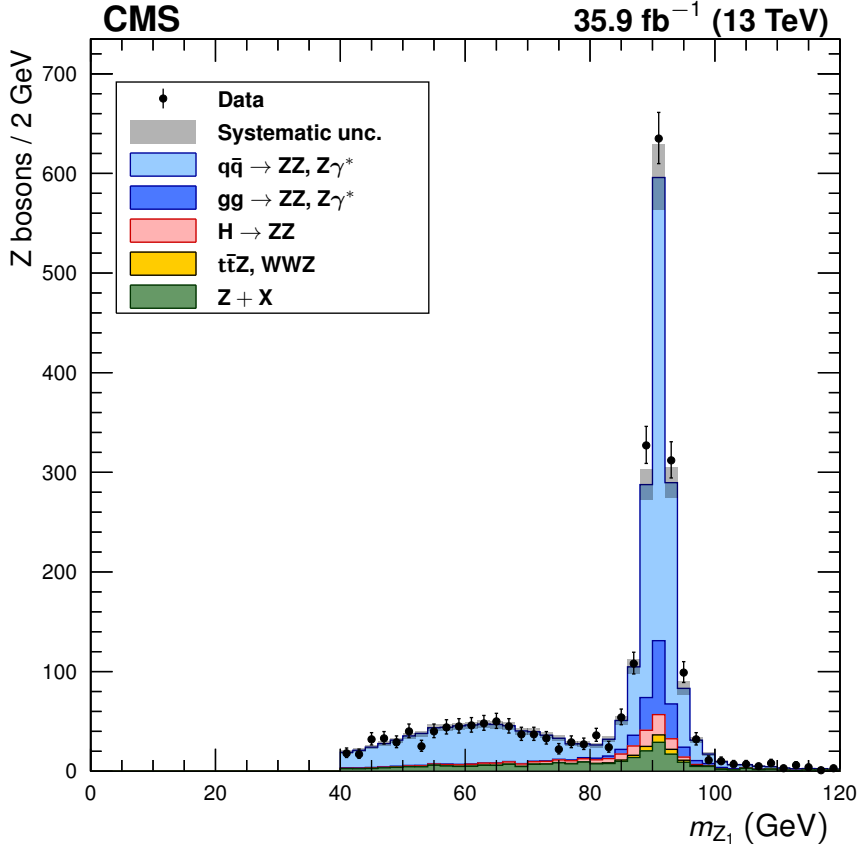


Figure 7.3: Distribution of the dilepton invariant mass of Z_1 , the Z/γ^* candidate in each event closest to the nominal m_Z , in the full spectrum selection. Points represent data, with statistical uncertainty bars. The stack of filled histograms represents the SM signal prediction and background estimate, with a grey band showing the sum in quadrature of the statistical and systematic uncertainties on the total expected yield.

46 m_{Z_2} against m_{Z_1} , for events in the same four-lepton mass region around the Higgs
 47 resonance. Agreement between predictions and data is again good.

48 7.1.4 ZZ Production

49 Expected and observed yields for on-shell ZZ events are shown in Table 7.3. The corre-
 50 sponding four-lepton and Z boson candidate invariant masses are shown in Figs. 7.11
 51 and 7.12, respectively. Figure 7.13 shows the distribution of the number of jets (N_{jets})

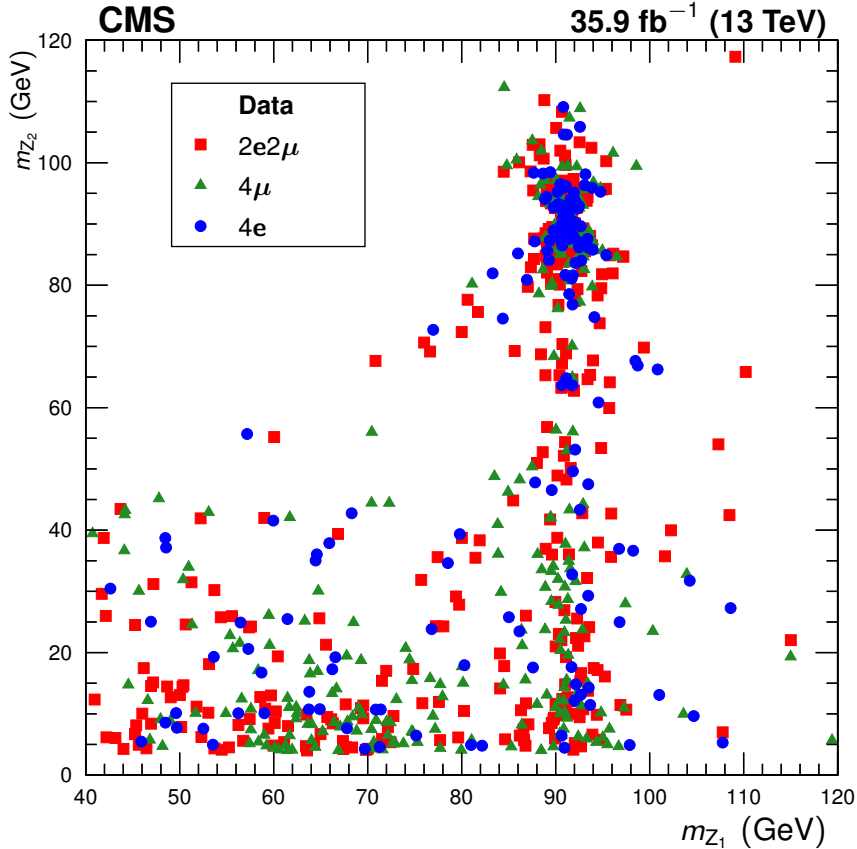


Figure 7.4: The reconstructed m_{Z_2} plotted against the reconstructed m_{Z_1} for data events in the full spectrum selection, with distinctive markers for each final state. For readability, only every fourth event is drawn. Clusters of events from different production modes are visible, as discussed in the text.

Table 7.2: Observed and expected yields of $H \rightarrow ZZ^* \rightarrow 4\ell$ events, including expected background yields, for events passing the Higgs selection in the mass range $118 < m_{4\ell} < 130$ GeV, shown for each final state and summed to the total. Uncertainties are statistical and systematic combined.

Final state	Expected N_H	SM continuum background	$Z + X$	Total expected	Observed
4μ	21.6 ± 1.9	$9.4^{+0.6}_{-0.7}$	$4.7^{+2.0}_{-1.8}$	35.8 ± 2.9	34
$2e2\mu$	26.5 ± 2.3	$11.0^{+0.7}_{-0.8}$	$6.9^{+3.1}_{-2.9}$	$44.4^{+3.7}_{-3.6}$	41
$4e$	10.2 ± 1.1	3.6 ± 0.3	$1.9^{+0.8}_{-1.0}$	15.8 ± 1.6	19
Total	58.3 ± 5.0	$24.1^{+1.5}_{-1.6}$	$13.5^{+3.7}_{-3.5}$	96.0 ± 6.7	94

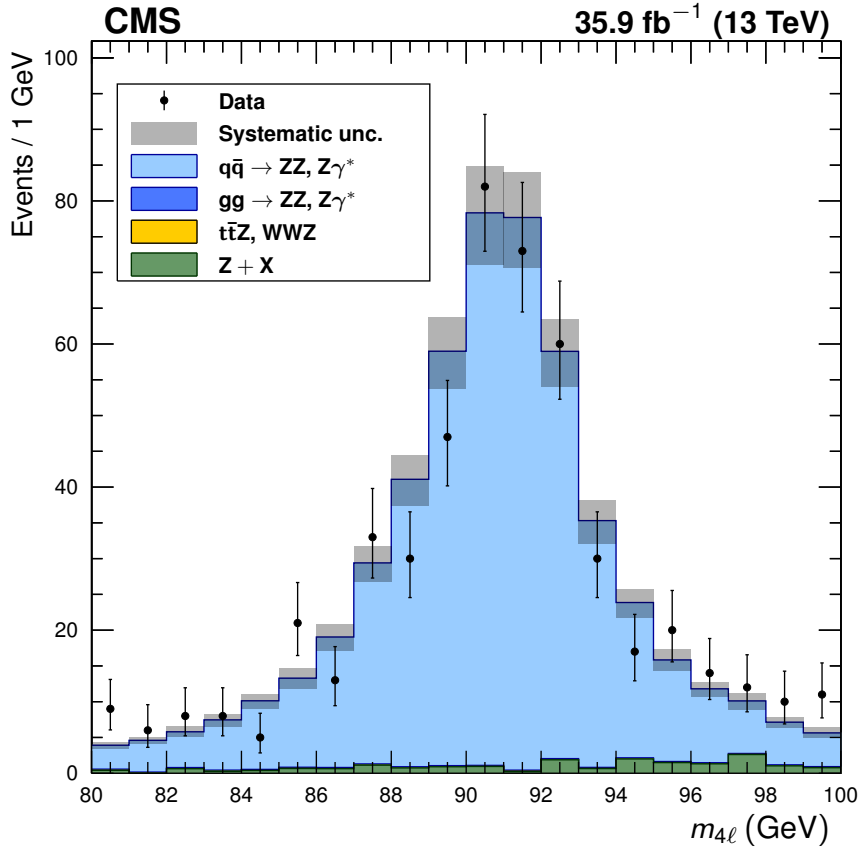


Figure 7.5: Distribution of the four-lepton invariant mass $m_{4\ell}$ of all events in the mass range $80 < m_{4\ell} < 100$ GeV, the $Z \rightarrow 4\ell$ selection. Points represent data, with statistical uncertainty bars. The stack of filled histograms represents the SM signal prediction and background estimate, with a grey band showing the sum in quadrature of the statistical and systematic uncertainties on the total expected yield.

52 in these events. The leading and subleading jet p_T are shown separately in Fig. 7.14,
 53 and the leading and subleading jet $|\eta|$ are shown separately in Fig. 7.15, for all events
 54 with at least one (leading) or two (subleading) jets. Figures 7.16 and 7.17 show the
 55 m_{jj} and $|\Delta\eta_{jj}|$ distributions for tagging jet pairs in the dijet selection. Agreement is,
 56 again, overall good.

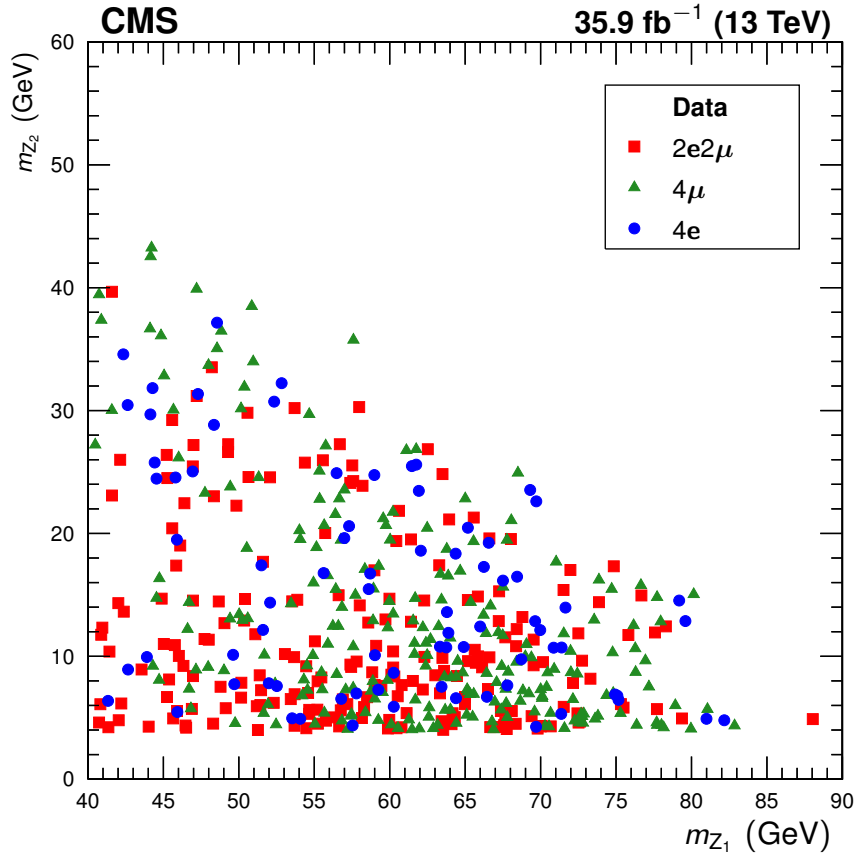


Figure 7.6: The reconstructed m_{Z_2} plotted against the reconstructed m_{Z_1} for all data events with $80 < m_{4\ell} < 100$ GeV, with distinctive markers for each final state.

Table 7.3: Observed and expected yields of ZZ events, including expected background yields, in the on-shell selection, shown for each final state and summed to the total. Uncertainties are statistical, then systematic, not including the integrated luminosity uncertainty.

Final state	Expected N_{ZZ}	Background	Total expected	Observed
4μ	$301 \pm 2 \pm 9$	$10 \pm 1 \pm 2$	$311 \pm 2 \pm 9$	335
$2e2\mu$	$503 \pm 2 \pm 19$	$31 \pm 2 \pm 4$	$534 \pm 3 \pm 20$	543
$4e$	$205 \pm 1 \pm 12$	$20 \pm 2 \pm 2$	$225 \pm 2 \pm 13$	220
Total	$1009 \pm 3 \pm 36$	$60 \pm 3 \pm 8$	$1070 \pm 4 \pm 37$	1098

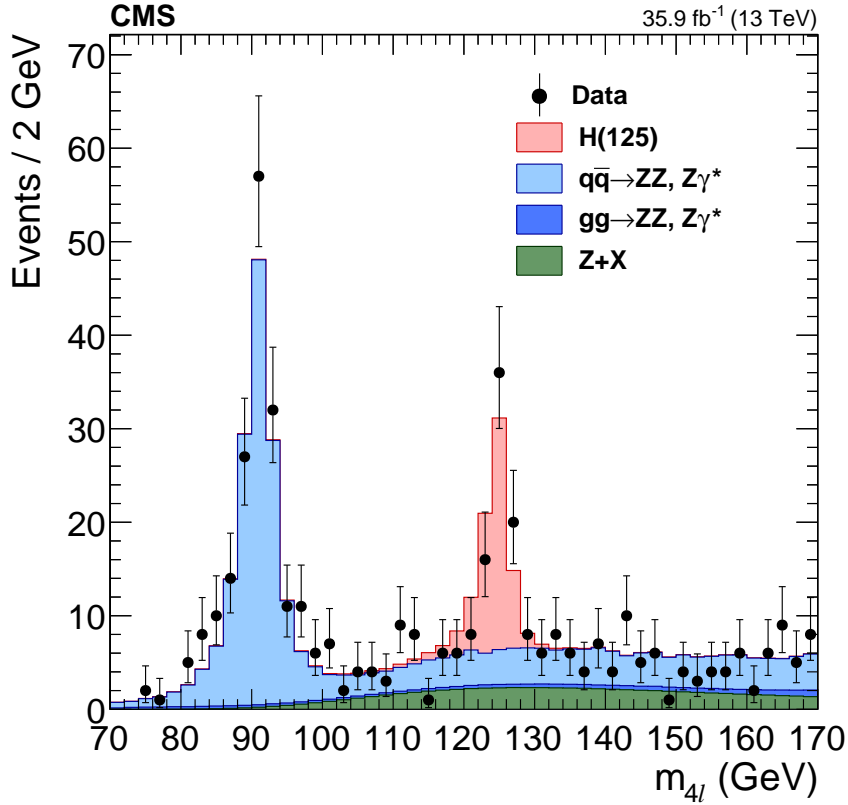


Figure 7.7: Distribution of the four-lepton invariant mass m_{4l} for events in the Higgs selection. Points represent data, with statistical uncertainty bars. The stack of filled histograms represents the signal and SM background predictions and the reducible background estimate.

⁵⁷ 7.2 ZZ Fiducial and Total Cross Section

⁵⁸ The yields shown in Table 7.3 and the systematic uncertainties of Table 6.1 are used
⁵⁹ as inputs to the maximum likelihood method described in Section 6.3.1 to obtain the
⁶⁰ on-shell ZZ signal strength across all channels,

$$\mu = 1.040^{+0.033}_{-0.032} \text{ (stat)}^{+0.037}_{-0.035} \text{ (syst)} \pm 0.026 \text{ (lumi)}, \quad (7.1)$$

⁶¹ which gives a fiducial cross section

$$\sigma_{\text{fid}}(\text{pp} \rightarrow \text{ZZ} \rightarrow 4\ell) = 40.9 \pm 1.3 \text{ (stat)} \pm 1.4 \text{ (syst)} \pm 1.0 \text{ (lumi)} \text{ fb}, \quad (7.2)$$

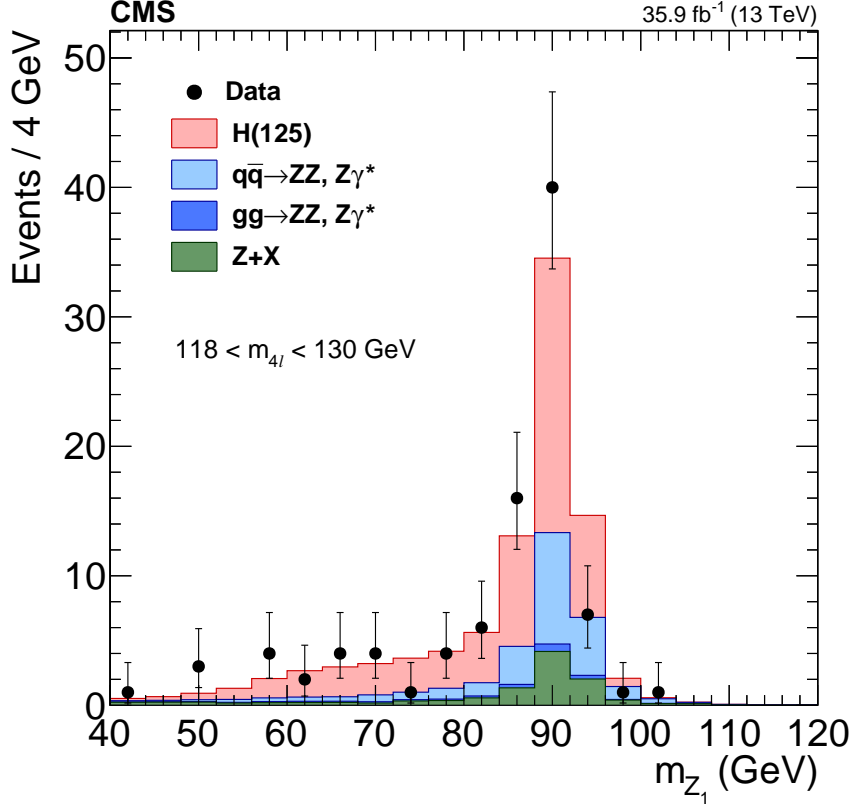


Figure 7.8: Distribution of the dilepton invariant mass of Z_1 , the dilepton candidate in each event closest to the nominal m_Z , in events in the Higgs selection with $118 < m_{4\ell} < 130 \text{ GeV}$. Points represent data, with statistical uncertainty bars. The stack of filled histograms represents the signal and SM background predictions and the reducible background estimate.

62 in the $ZZ \rightarrow 4\ell$ fiducial phase space of Table 6.2. The corresponding total cross
 63 section is

$$\sigma(pp \rightarrow ZZ) = 17.5^{+0.6}_{-0.5} (\text{stat}) \pm 0.6 (\text{syst}) \pm 0.4 (\text{theo}) \pm 0.4 (\text{lumi}) \text{ pb.} \quad (7.3)$$

64 This measurement, on 2016 data, agrees with the result of the 2015 measure-
 65 ment [178],

$$\sigma(pp \rightarrow ZZ) = 14.6^{+1.9}_{-1.8} (\text{stat})^{+0.3}_{-0.5} (\text{syst}) \pm 0.2 (\text{theo}) \pm 0.4 (\text{lumi}) \text{ pb.} \quad (7.4)$$

66 One may combine the measurements by doing a six-bin simultaneous fit with the bins

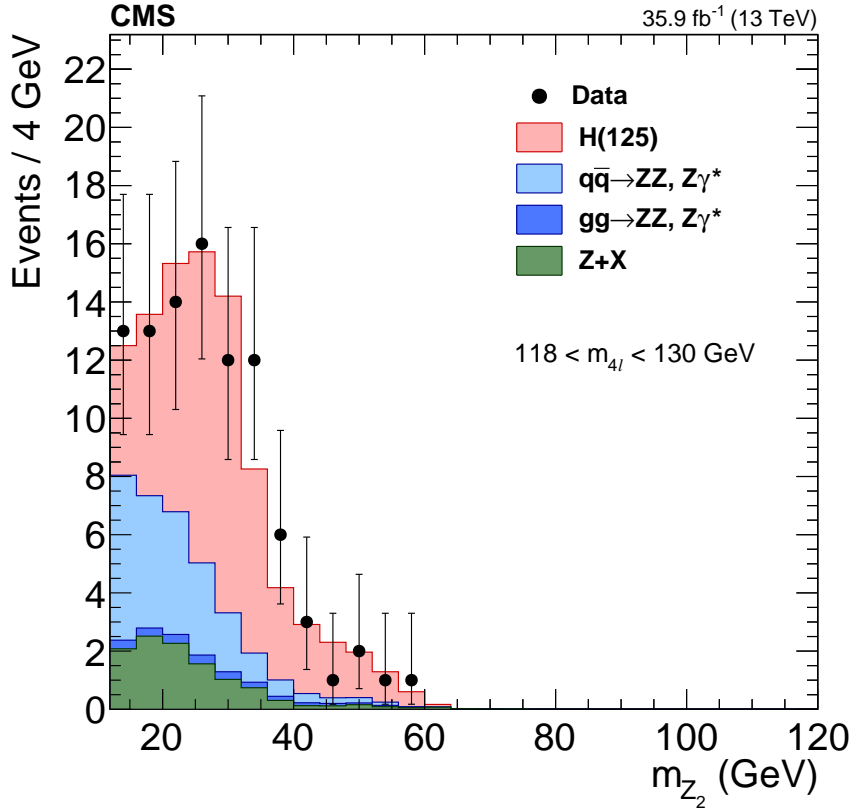


Figure 7.9: Distribution of the dilepton invariant mass of Z_2 , the dilepton candidate in each event farther from the nominal m_Z , in events in the Higgs selection with $118 < m_{4\ell} < 130 \text{ GeV}$. Points represent data, with statistical uncertainty bars. The stack of filled histograms represents the signal and SM background predictions and the reducible background estimate.

representing the same channel in 2015 and 2016 considered separate. The degree of correlation between the systematic uncertainties in the 2015 and 2016 runs is not known, but the 2015 contribution is small enough that the systematic uncertainties are dominated by those in the 2016 dataset, and the degree of correlation will have only a small effect on the measurement. We therefore do the fit twice, once treating the experimental uncertainties as fully correlated between the datasets, and again treating them as fully uncorrelated. The small difference in the central value obtained is added linearly to the systematic error of the result. After the full combination, the

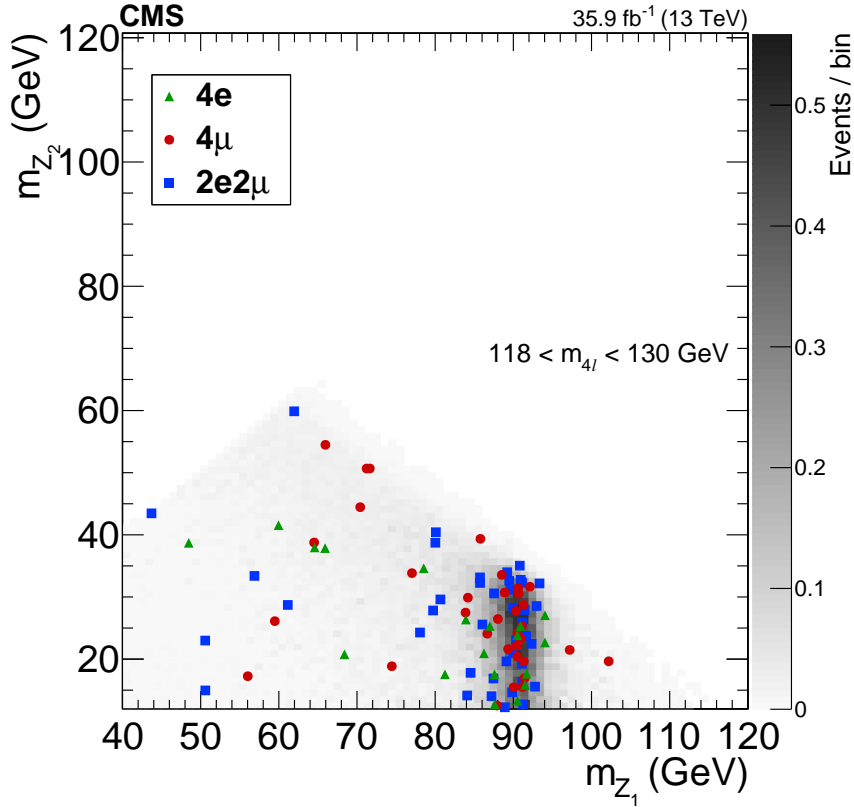


Figure 7.10: The reconstructed m_{Z_2} mass plotted against the reconstructed m_{Z_1} for data events in the Higgs selection with $118 < m_{4\ell} < 130$ GeV, with distinctive markers for each final state. The shading represents the expected number of events in the bin.

75 “2015 + 2016” total cross section is found to be

$$\sigma(pp \rightarrow ZZ) = 17.2 \pm 0.5 \text{ (stat)} \pm 0.7 \text{ (syst)} \pm 0.4 \text{ (theo)} \pm 0.4 \text{ (lumi)} \text{ pb.} \quad (7.5)$$

76 These results can be compared to the MATRIX prediction of $16.2^{+0.6}_{-0.4}$ pb, computed
 77 at NNLO in QCD, or the MCFM prediction of $15.0^{+0.7}_{-0.6} \pm 0.2$ pb, calculated at NLO
 78 in QCD with LO gg \rightarrow ZZ diagrams included. Both predictions use the NNPDF3.0
 79 PDF sets and fixed scales $\mu_F = \mu_R = m_Z$.

80 The total cross section is shown as a function of \sqrt{s} in Fig. 7.18. Measure-
 81 ments from CMS [54–56, 178] and ATLAS [58, 59, 87] are compared to NLO pre-
 82 dictions made with MCFM (with contributions from leading order gluon-gluon fusion

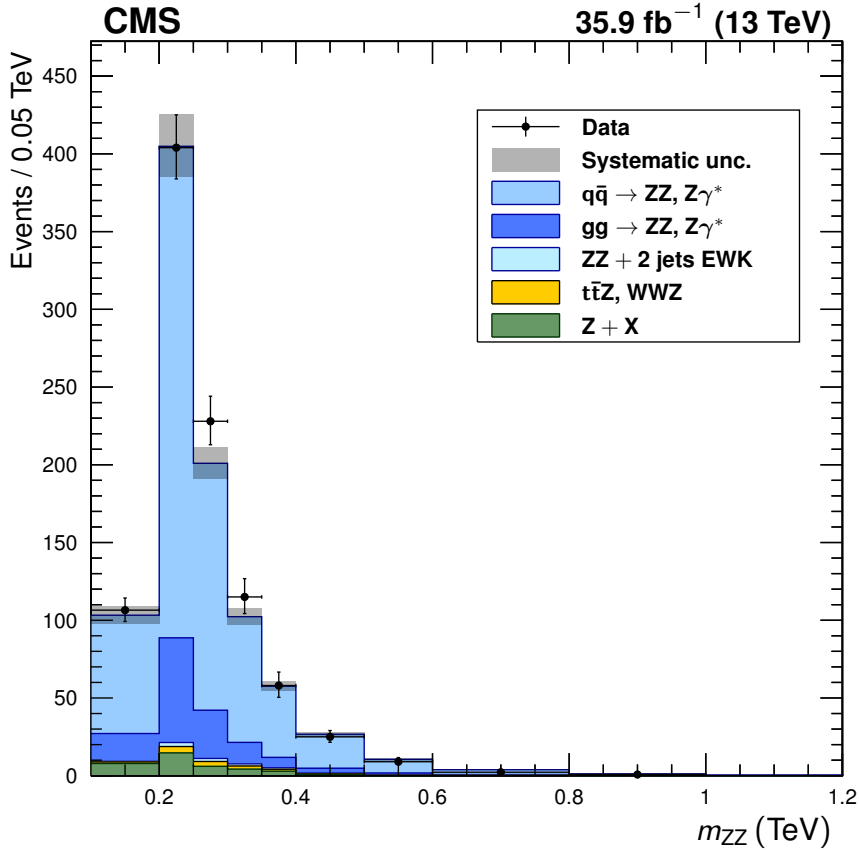


Figure 7.11: Distribution of the four-lepton invariant mass m_{ZZ} of all events in the on-shell selection. Points represent data, with statistical uncertainty bars. The stack of filled histograms represents the SM signal prediction and background estimate, with a grey band showing the sum in quadrature of the statistical and systematic uncertainties on the total expected yield.

83 diagrams), and NNLO predictions made with MATRIX. Results from both experi-
 84 ments agree with the predictions.

85 7.2.1 $Z \rightarrow 4\ell$ Branching Fraction

86 The signal strength in the $Z \rightarrow 4\ell$ selection is

$$\mu = 0.980^{+0.046}_{-0.044} (\text{stat})^{+0.065}_{-0.059} (\text{syst}) \pm 0.025 (\text{lumi}), \quad (7.6)$$

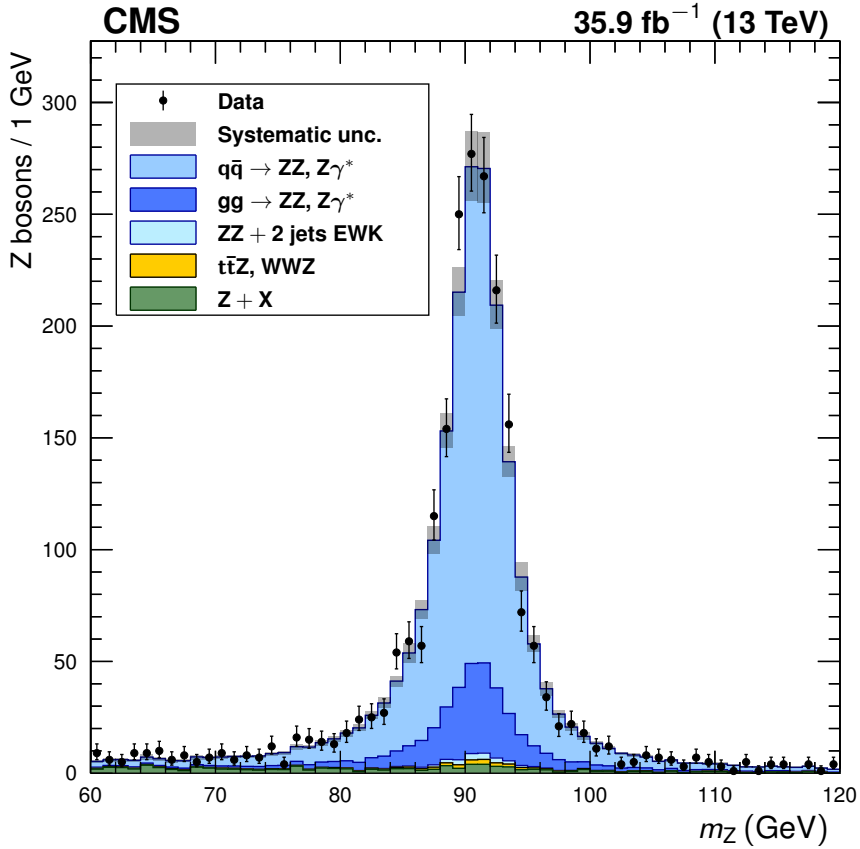


Figure 7.12: Distribution of the dilepton invariant mass of Z candidates in all events in the on-shell selection, regardless of whether the lepton pair is labeled Z_1 or Z_2 . Points represent data, with statistical uncertainty bars. The stack of filled histograms represents the SM signal prediction and background estimate, with a grey band showing the sum in quadrature of the statistical and systematic uncertainties on the total expected yield.

87 yielding a fiducial cross section

$$\sigma_{\text{fid}} (\text{pp} \rightarrow Z \rightarrow 4\ell) = 31.2^{+1.5}_{-1.4} (\text{stat})^{+2.1}_{-1.9} (\text{syst}) \pm 0.8 (\text{lumi}) \text{ fb.} \quad (7.7)$$

88 This is scaled by an acceptance correction factor $\mathcal{A} = 0.125 \pm 0.002$, estimated with
89 POWHEG, to the total $Z \rightarrow 4\ell$ cross section times branching ratio,

$$\sigma(\text{pp} \rightarrow Z) \times \mathcal{B}(Z \rightarrow 4\ell) = 249 \pm 8 (\text{stat})^{+9}_{-8} (\text{syst}) \pm 4 (\text{theo}) \pm 6 (\text{lumi}) \text{ fb.} \quad (7.8)$$

90 Equation (6.10) is used to calculate the branching fraction. The Z cross section

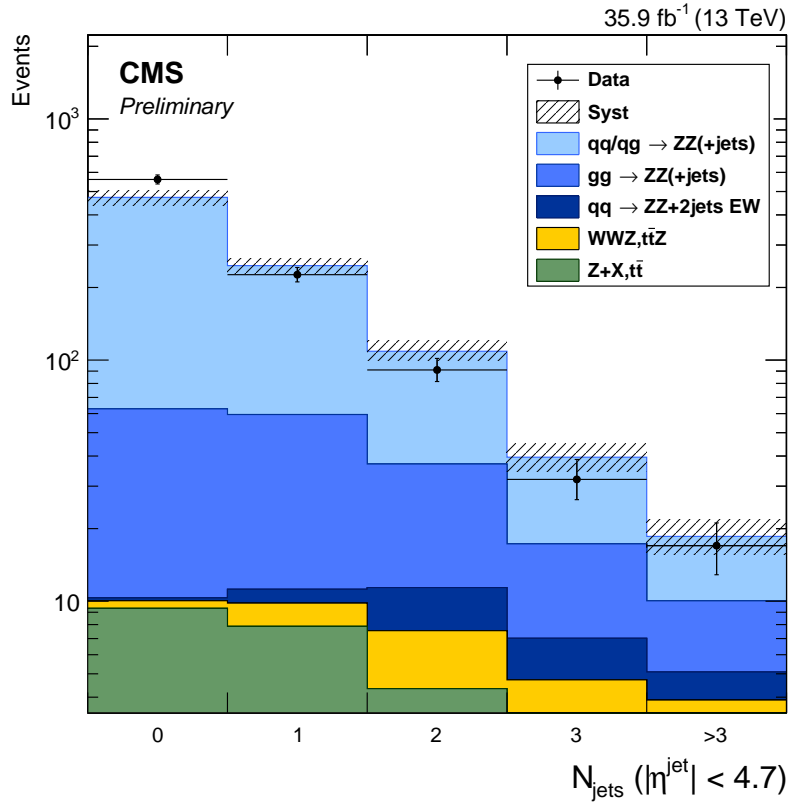


Figure 7.13: Distribution of jet multiplicity in ZZ events. Points represent data, with statistical uncertainty bars. The stack of filled histograms represents the SM signal prediction and background estimate, with a hatched band showing the sum in quadrature of the statistical and systematic uncertainties on the total expected yield.

91 times dilepton branching ratio is calculated with FEWZ v2.0 [183] at NNLO in QCD
 92 to be $\sigma(Z \rightarrow 2\ell) = 1870^{+50}_{-40}$ pb. The Z mass window correction factor is calculated
 93 with POWHEG and found to be $C_{80-100}^{60-120} = 0.926 \pm 0.001$. Its uncertainty includes scale
 94 and PDF variations. The nominal Z to dilepton branching fraction is $\mathcal{B}(Z \rightarrow 2\ell) =$
 95 0.03366 [39]. The four-lepton branching fraction is measured to be

$$\mathcal{B}(Z \rightarrow 4\ell) = 4.8 \pm 0.2 \text{ (stat)} \pm 0.2 \text{ (syst)} \pm 0.1 \text{ (theo)} \pm 0.1 \text{ (lumi)} \times 10^{-6}. \quad (7.9)$$

96 This value is consistent with the theoretical value of 4.6×10^{-6} , calculated with MAD-
 97 GRAPH5_AMC@NLO, and with previous measurements from CMS and ATLAS [71,

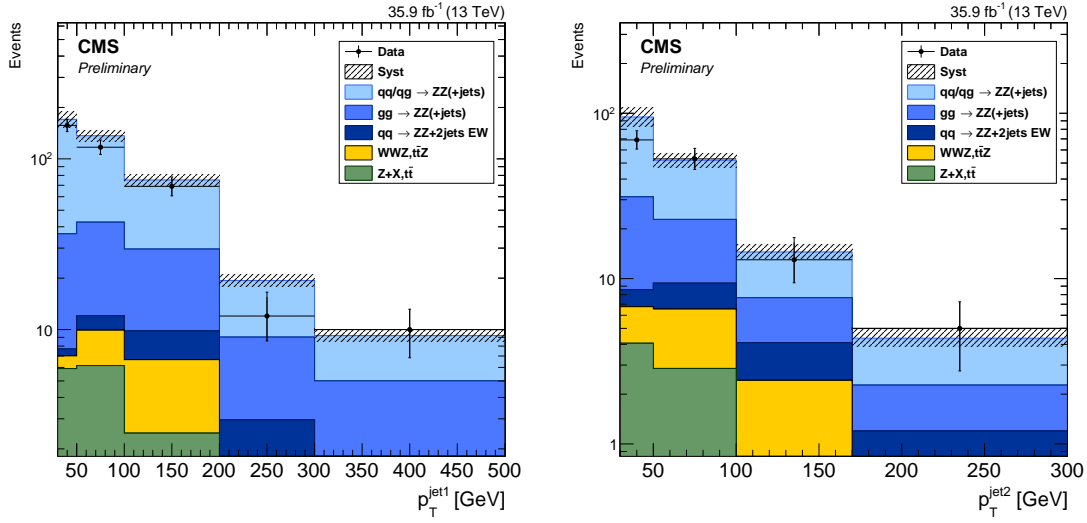


Figure 7.14: Distribution of leading (left) and subleading (right) jet p_T for all ZZ events with at least one jet and at least two jets, respectively. Points represent data, with statistical uncertainty bars. The stack of filled histograms represents the SM signal prediction and background estimate, with a hatched band showing the sum in quadrature of the statistical and systematic uncertainties on the total expected yield.

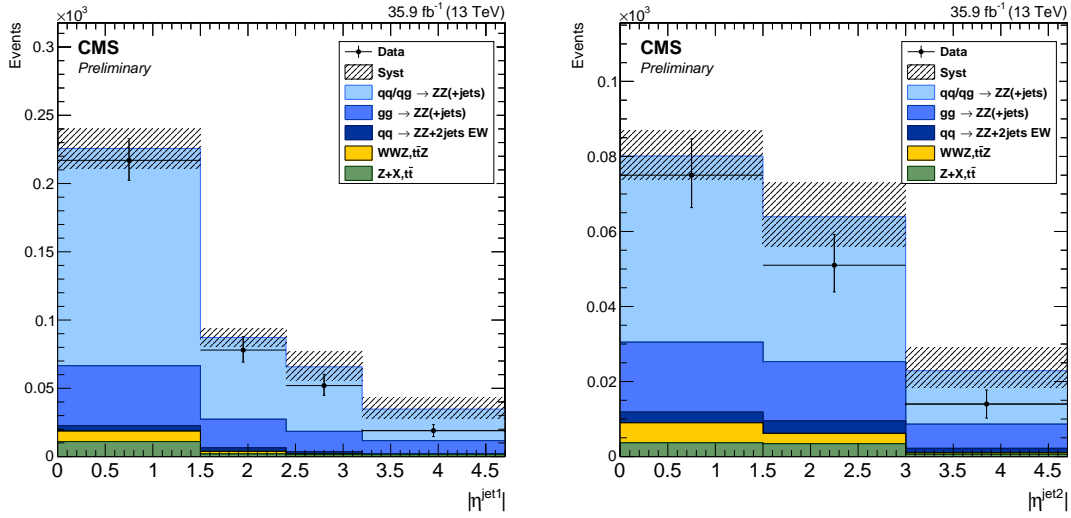


Figure 7.15: Distribution of leading (left) and subleading (right) jet $|\eta|$ for all ZZ events with at least one jet and at least two jets, respectively. Points represent data, with statistical uncertainty bars. The stack of filled histograms represents the SM signal prediction and background estimate, with a hatched band showing the sum in quadrature of the statistical and systematic uncertainties on the total expected yield.

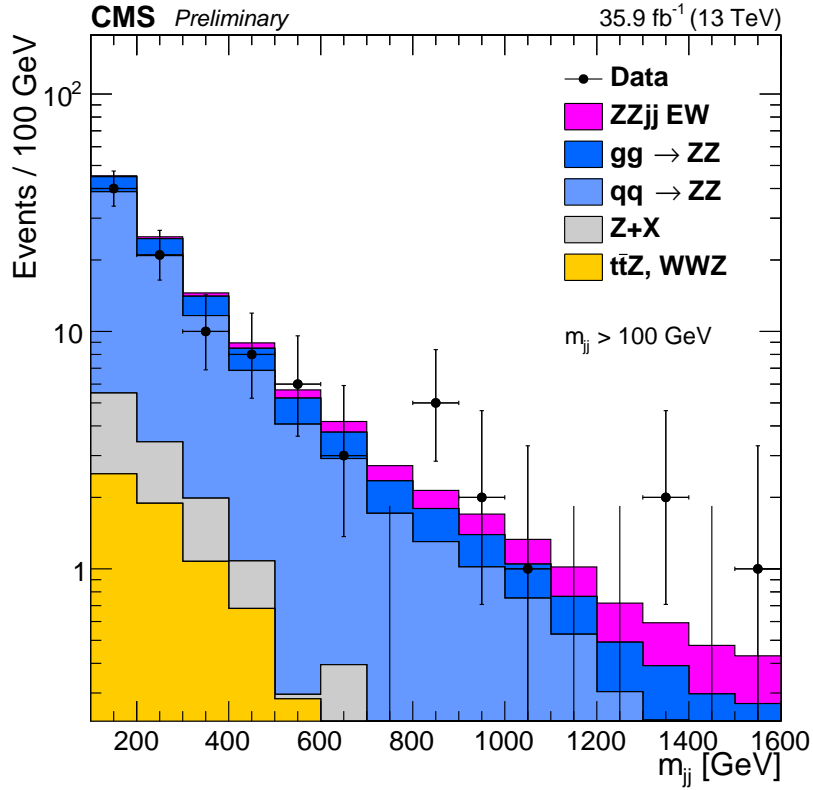


Figure 7.16: Dijet invariant mass m_{jj} of the tag jets in ZZ events passing the dijet selection ($m_{jj} > 100$ GeV). Points represent data, with statistical uncertainty bars. The stack of filled histograms represents the SM signal prediction, including EWK production, and background estimate.

⁹⁸ 72, 178].

⁹⁹ 7.3 Differential Cross Sections

¹⁰⁰ Detector-level distributions are unfolded to calculate differential cross sections as de-
¹⁰¹ scribed in Section 6.4. Figures 7.19–7.30 show measured differential cross sections
¹⁰² and corresponding theory predictions, as functions of different observables. All dis-
¹⁰³ tributions are normalized to the inclusive fiducial cross section, such that the integral
¹⁰⁴ of each is unity, including overflow bins (not shown). The observables in Figs. 7.19–

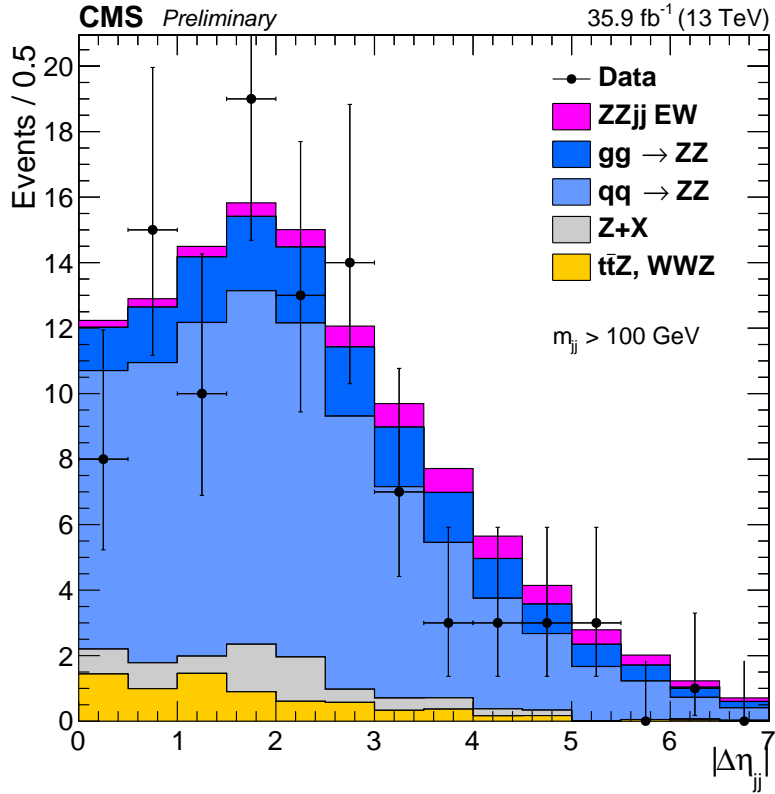


Figure 7.17: Pseudorapidity separation $|\Delta\eta_{jj}|$ of tag jets in ZZ events passing the dijet selection ($m_{jj} > 100 \text{ GeV}$). Points represent data, with statistical uncertainty bars. The stack of filled histograms represents the SM signal prediction, including EWK production, and background estimate.

105 7.24 consider only the four-lepton system. For the calculation of these distributions,
 106 as well as the differential cross section as a function of N_{jets} (Fig. 7.25), all events
 107 passing the on-shell selection are used. Figures 7.26 and 7.27 show m_{jj} and $|\Delta\eta_{jj}|$
 108 for all ZZ events with at least two jets, while Figs 7.28 and 7.29 show p_T and η ,
 109 respectively, for the leading jet in events with $N_{\text{jets}} \geq 1$ on the left and the subleading
 110 jet in events with $N_{\text{jets}} \geq 2$ on the right. In Fig. 7.30, the phase space is expanded to
 111 the full spectrum selection at both detector and true level, to show the four-lepton
 112 differential cross section through all production modes as a function of $m_{4\ell}$. Measured
 113 cross sections overall agree with the theoretical predictions within their uncertainties,

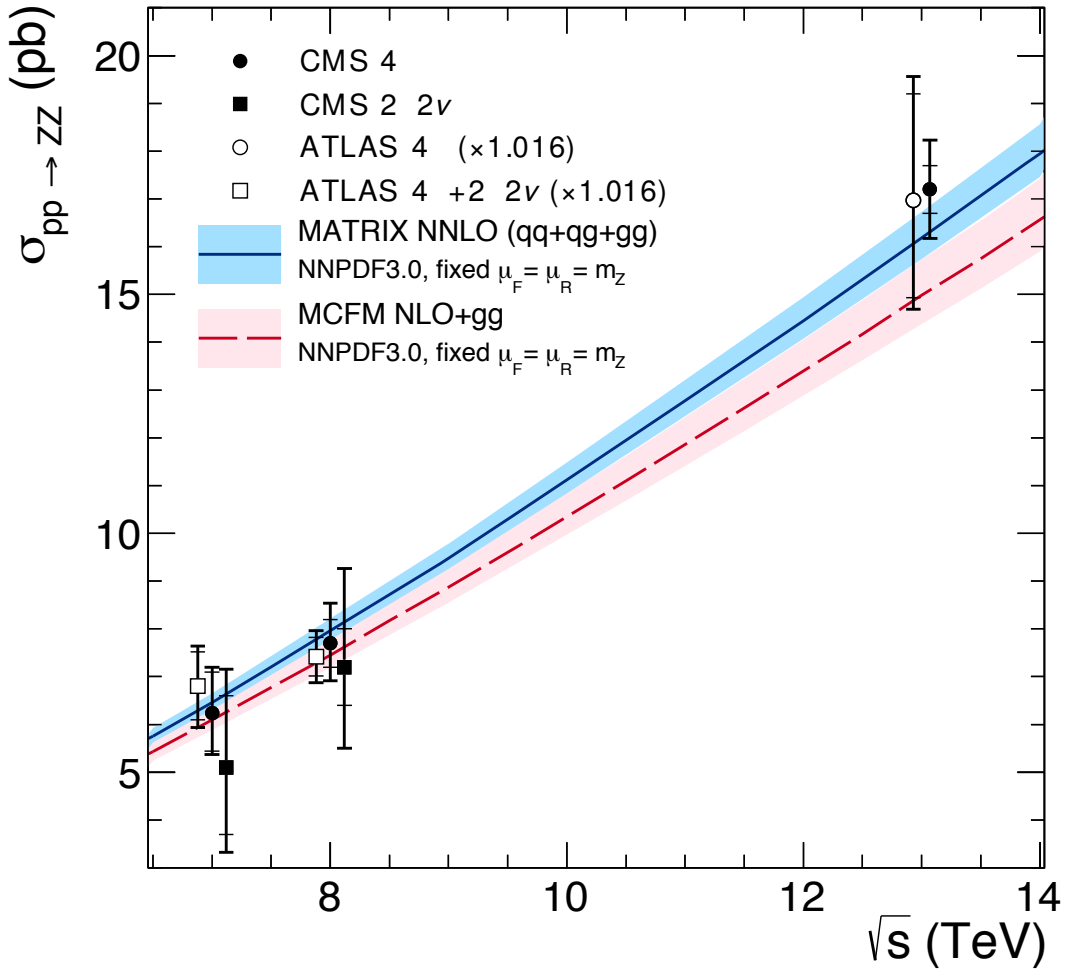


Figure 7.18: The total ZZ cross section is shown as a function of \sqrt{s} . Measurements from CMS and ATLAS are both shown, with the ATLAS numbers adjusted upward by 1.6% to account for differences in Z mass window choice. Points at the same center-of-mass energy are shifted slightly in the horizontal direction for clarity. Experimental measurements are compared to predictions from MCFM at NLO in QCD with additional contributions from LO gluon-gluon fusion diagrams, and MATRIX at NNLO in QCD. Both sets of predictions use the NNPDF3.0 PDF sets and fixed scales $\mu_F = \mu_R = m_Z$.

114 which are dominated by statistical uncertainties.

115 7.4 Vector Boson Scattering

116 Figure 7.31 shows the output of the GBDT discussed in Section 6.5 for events in the
 117 dijet selection. The search procedure finds a modest excess of VBS signal, at the
 118 level of 2.7 standard deviations over the null hypothesis of the SM without VBS ZZ
 119 production. The expected significance is 1.6 standard deviations. This corresponds
 120 to a VBS fiducial cross section of

$$\sigma_{\text{fid}}(\text{pp} \rightarrow \text{ZZjj(EWK)} \rightarrow 4\ell\text{jj}) = 0.40^{+0.21}_{-0.16} (\text{stat})^{+0.13}_{-0.09} (\text{syst}) \text{ fb}, \quad (7.10)$$

121 which is consistent with the SM prediction of $0.29^{+0.02}_{-0.03}$ fb.

122 7.5 Anomalous Coupling Limits

123 The ZZ invariant mass is shown in Fig. 7.32 for all events in the on-shell selection,
 124 with example distributions shown for potential scenarios with nonzero aTGCs. The
 125 limit setting procedure described in Section 6.6 is applied to each aTGC parameter,
 126 with all other couplings fixed to their SM values, to yield one-dimensional 95% CL
 127 limits,

$$\begin{aligned} -0.0012 < f_4^Z < 0.0010, \quad -0.0010 < f_5^Z < 0.0013, \\ -0.0012 < f_4^\gamma < 0.0013, \quad -0.0012 < f_5^\gamma < 0.0013. \end{aligned} \quad (7.11)$$

128 These results improve the previous CMS limits by factors of 3–4 [55] are the most
 129 stringent limits to date on the parameters in question. Two-dimensional limits are
 130 set in the f_4^γ - f_4^Z and f_5^γ - f_5^Z planes, holding all other parameters to the SM values in
 131 each calculation. One- and two-dimensional 95% CL limits are shown in Fig. 7.33.

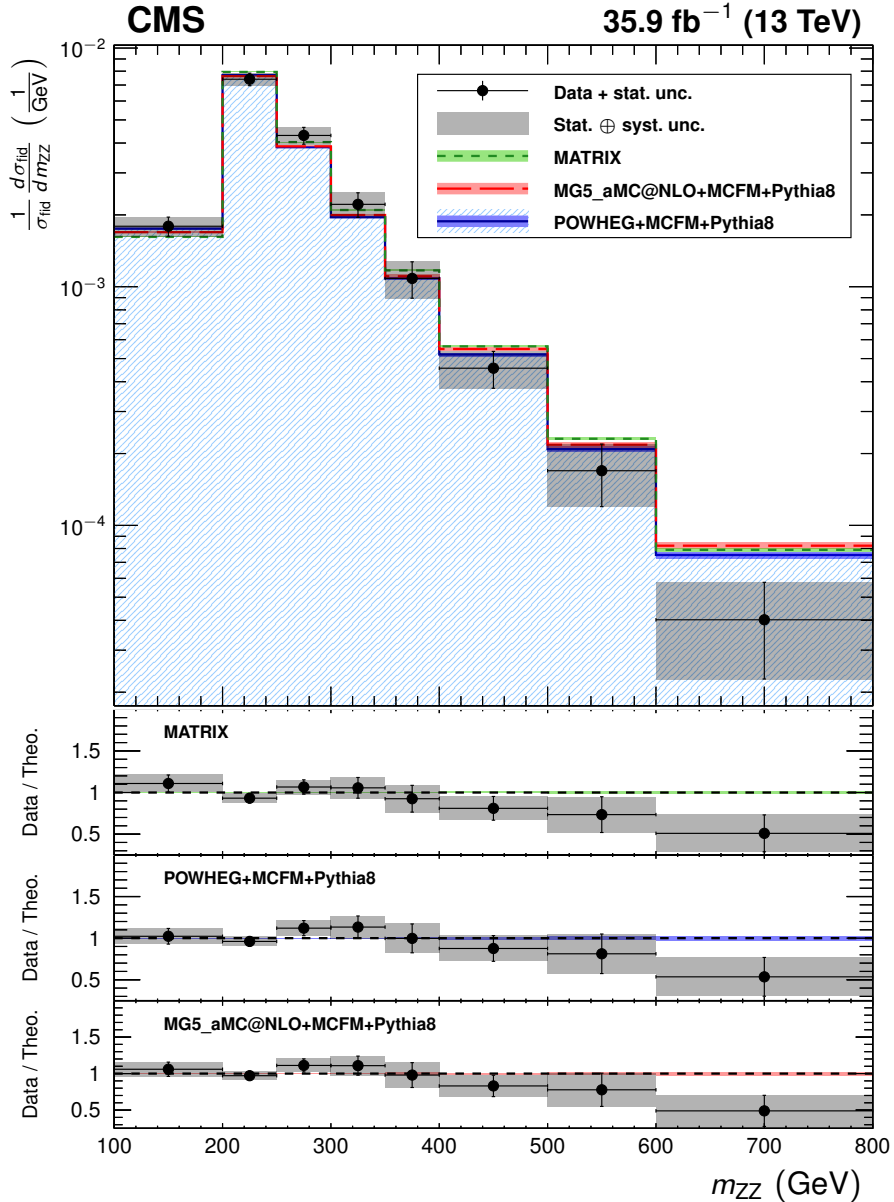


Figure 7.19: The ZZ differential cross section as a function of m_{ZZ} , normalized to the inclusive fiducial cross section. Points represent the unfolded data, with vertical bars showing the statistical uncertainty and a grey band showing the sum in quadrature of the statistical and systematic uncertainties. Blue, red, and green histograms represent the POWHEG+MCFM, MADGRAPH5_AMC@NLO+MCFM, and MATRIX predictions, respectively, with bands around each which represent their combined statistical, scale, and PDF uncertainties. The lower sections of the plot represents the ratio of the measured cross section to each of the predictions.

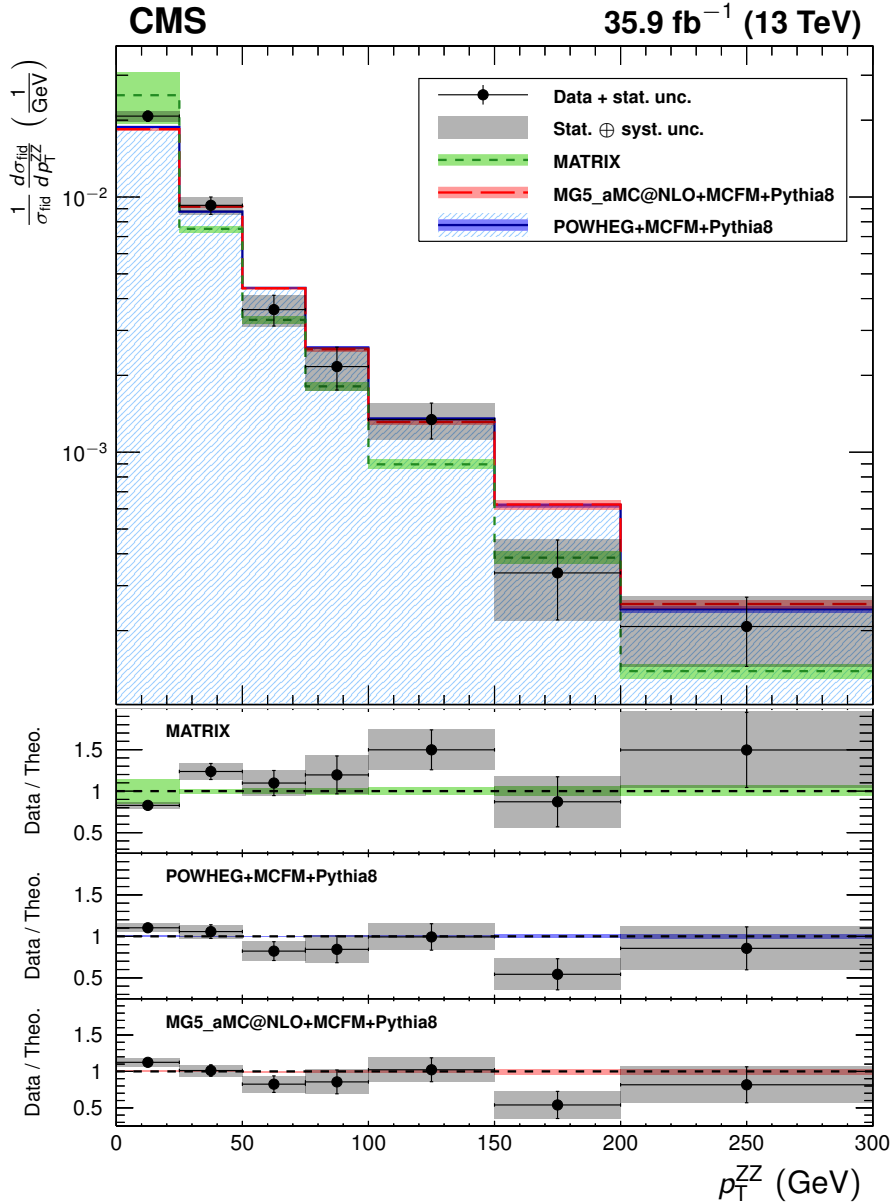


Figure 7.20: The ZZ differential cross section as a function of the four-lepton p_T , normalized to the inclusive fiducial cross section. Points represent the unfolded data, with vertical bars showing the statistical uncertainty and a grey band showing the sum in quadrature of the statistical and systematic uncertainties. Blue, red, and green histograms represent the POWHEG+MCFM, MADGRAPH5_AMC@NLO+MCFM, and MATRIX predictions, respectively, with bands around each which represent their combined statistical, scale, and PDF uncertainties. The lower sections of the plot represents the ratio of the measured cross section to each of the predictions.

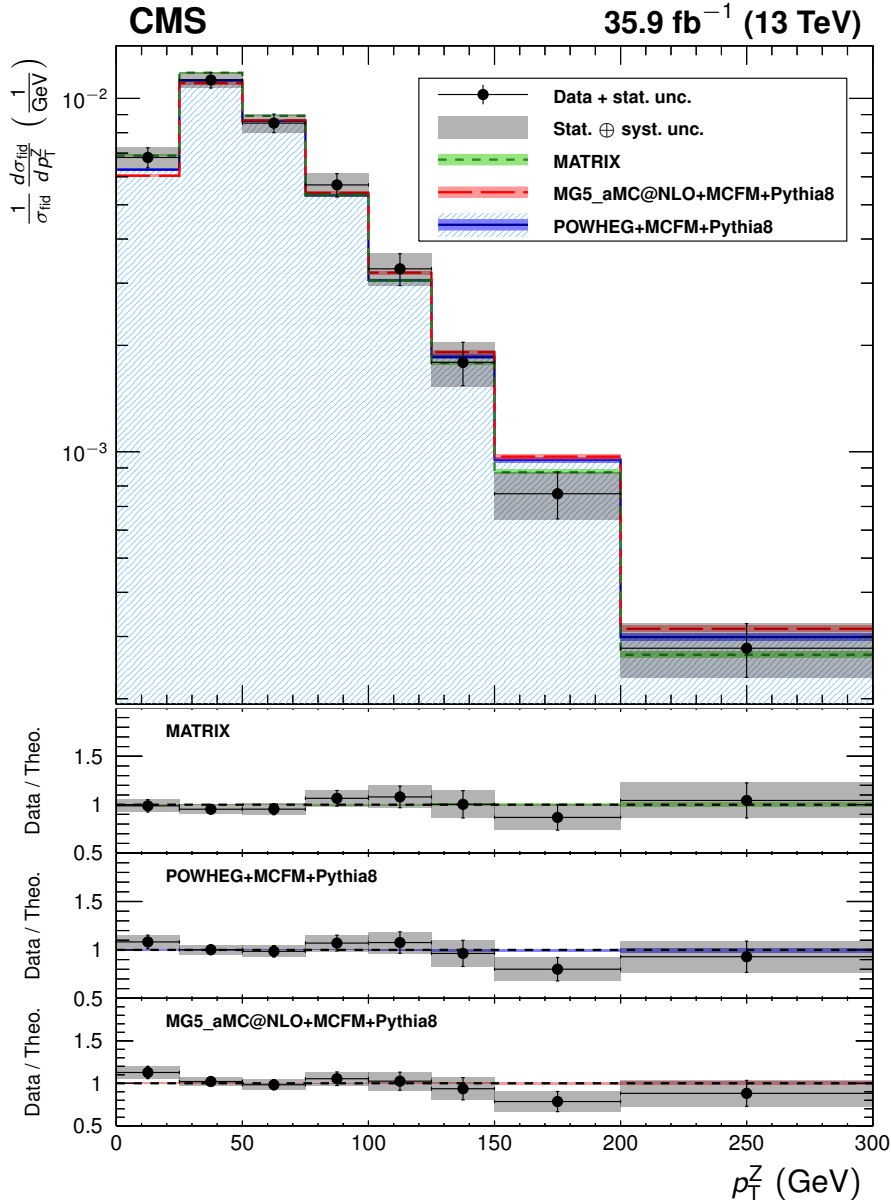


Figure 7.21: The ZZ differential cross section as a function of the p_T of both Z boson candidates, regardless of which one is Z_1 and which is Z_2 , normalized to the inclusive fiducial cross section. Points represent the unfolded data, with vertical bars showing the statistical uncertainty and a grey band showing the sum in quadrature of the statistical and systematic uncertainties. Blue, red, and green histograms represent the POWHEG+MCFM, MADGRAPH5_AMC@NLO+MCFM, and MATRIX predictions, respectively, with bands around each which represent their combined statistical, scale, and PDF uncertainties. The lower sections of the plot represents the ratio of the measured cross section to each of the predictions.

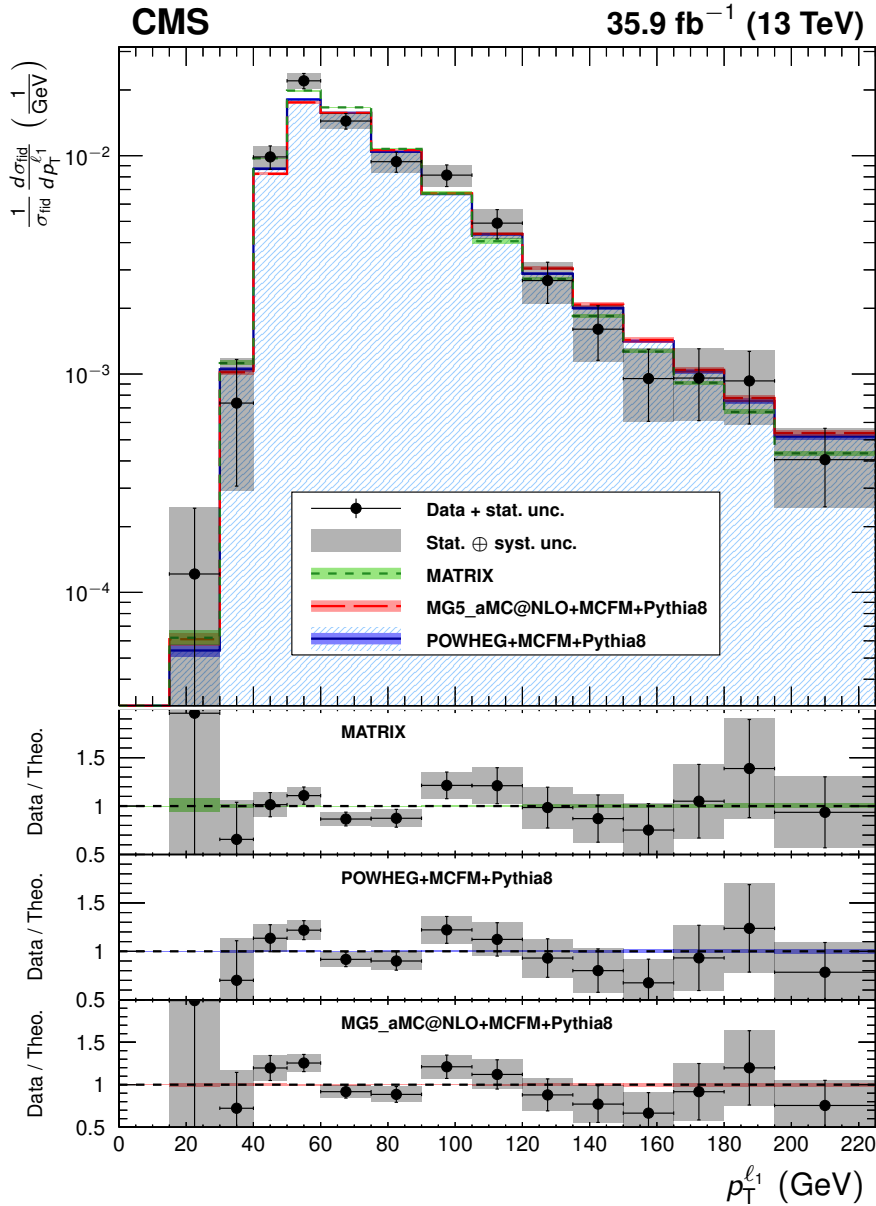


Figure 7.22: The ZZ differential cross section as a function of leading lepton p_T , normalized to the inclusive fiducial cross section. Points represent the unfolded data, with vertical bars showing the statistical uncertainty and a grey band showing the sum in quadrature of the statistical and systematic uncertainties. Blue, red, and green histograms represent the POWHEG+MCFM, MADGRAPH5_AMC@NLO+MCFM, and MATRIX predictions, respectively, with bands around each which represent their combined statistical, scale, and PDF uncertainties. The lower sections of the plot represents the ratio of the measured cross section to each of the predictions.

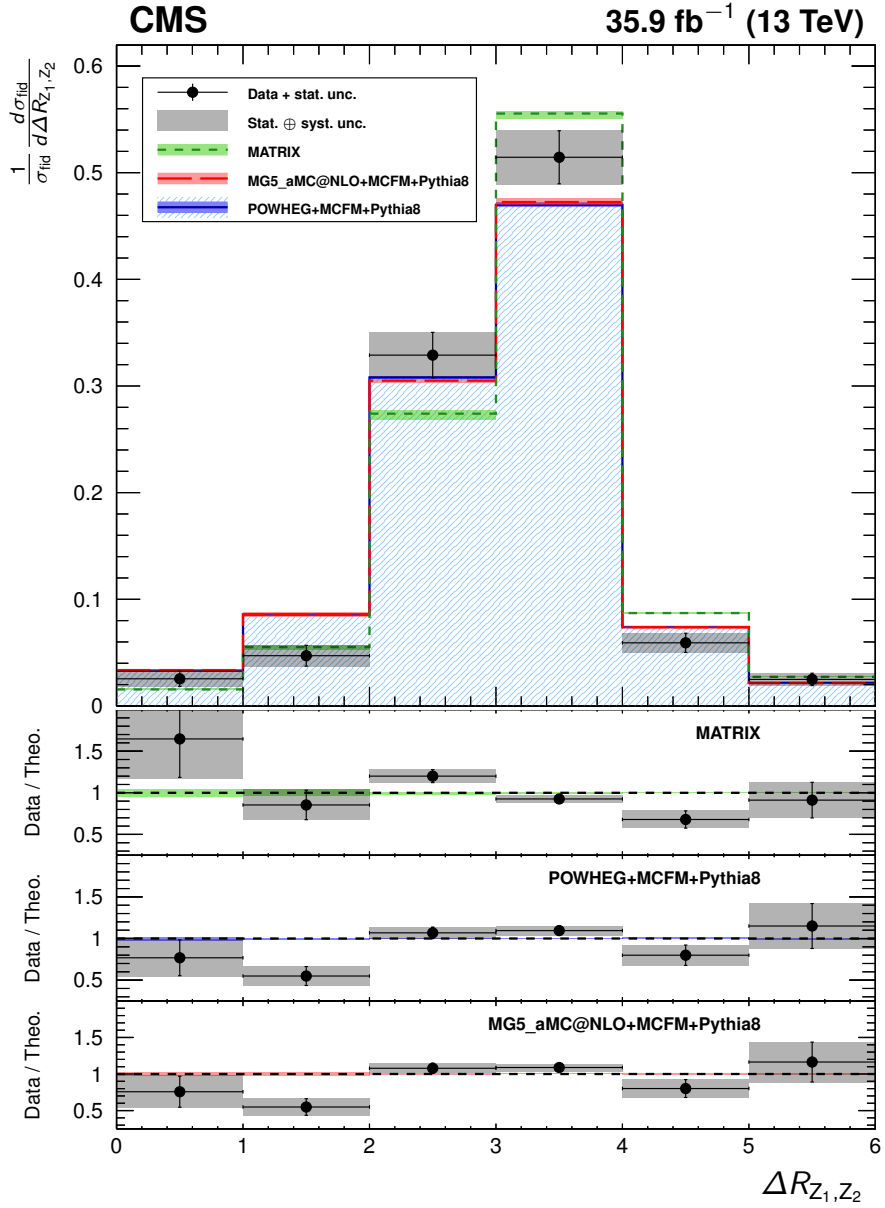


Figure 7.23: The ZZ differential cross section as a function of ΔR between the two Z bosons, normalized to the inclusive fiducial cross section. Points represent the unfolded data, with vertical bars showing the statistical uncertainty and a grey band showing the sum in quadrature of the statistical and systematic uncertainties. Blue, red, and green histograms represent the POWHEG+MCFM, MADGRAPH5_AMC@NLO+MCFM, and MATRIX predictions, respectively, with bands around each which represent their combined statistical, scale, and PDF uncertainties. The lower sections of the plot represents the ratio of the measured cross section to each of the predictions.

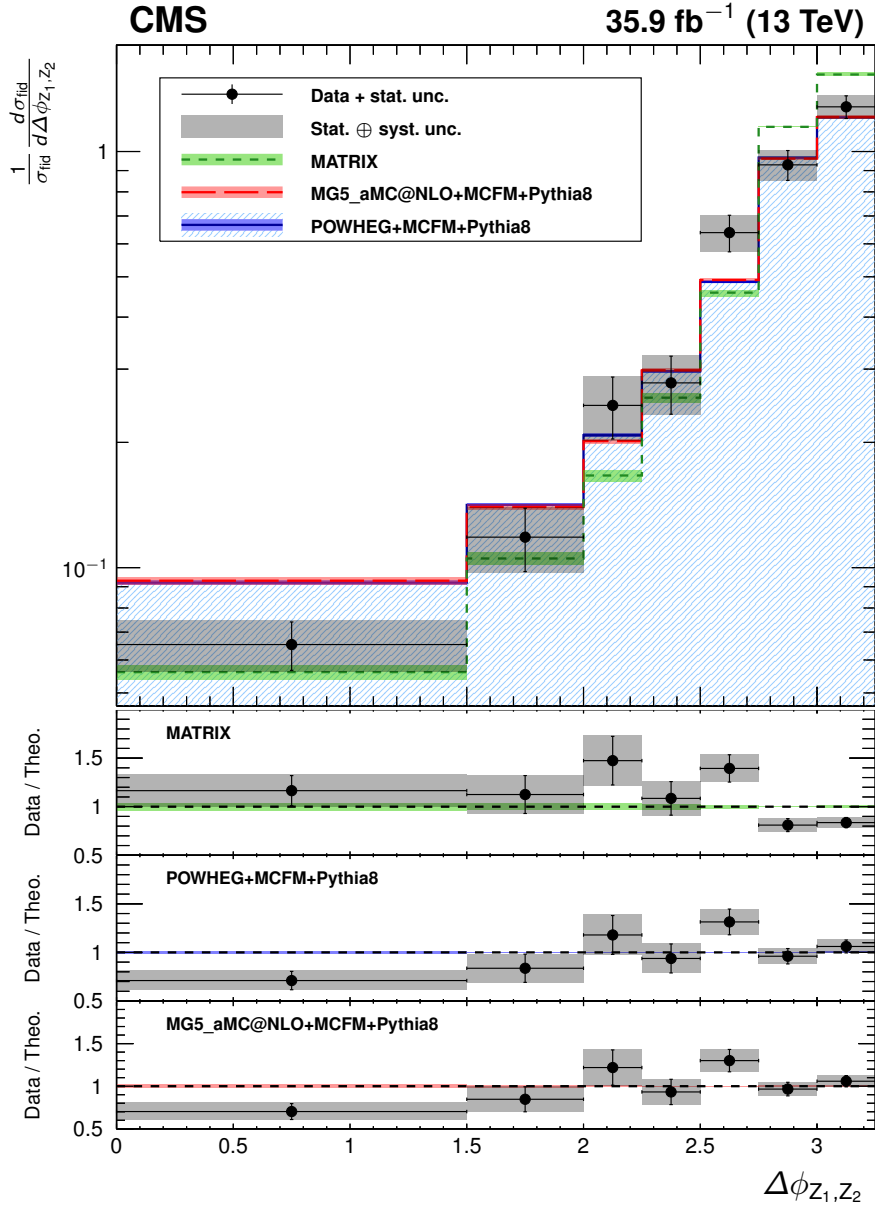


Figure 7.24: The ZZ differential cross section as a function of $\Delta\phi$ between the two Z bosons, normalized to the inclusive fiducial cross section. Points represent the unfolded data, with vertical bars showing the statistical uncertainty and a grey band showing the sum in quadrature of the statistical and systematic uncertainties. Blue, red, and green histograms represent the POWHEG+MCFM, MADGRAPH5_AMC@NLO+MCFM, and MATRIX predictions, respectively, with bands around each which represent their combined statistical, scale, and PDF uncertainties. The lower sections of the plot represents the ratio of the measured cross section to each of the predictions.

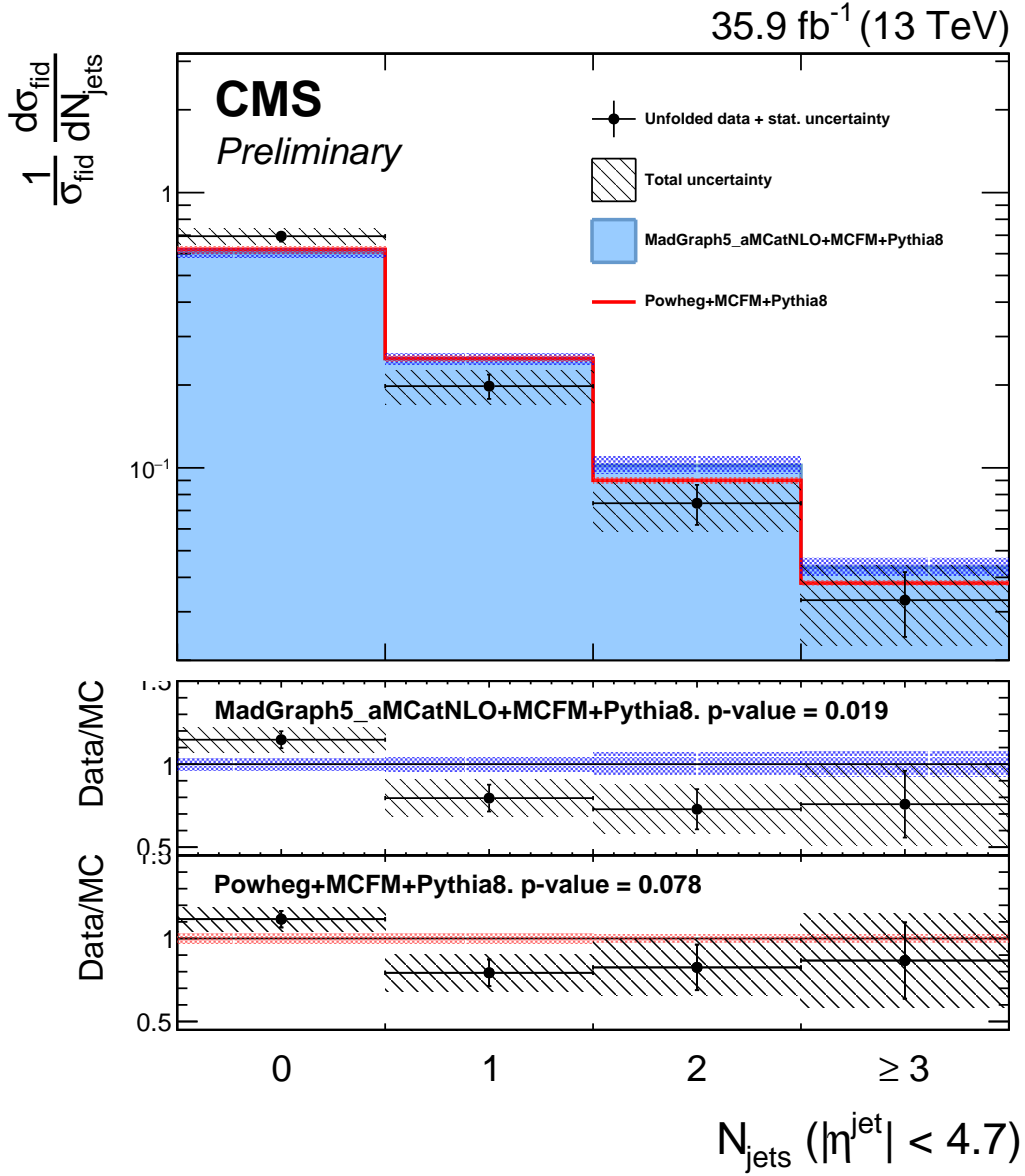


Figure 7.25: The ZZ differential cross section as a function of the jet multiplicity N_{jets} , normalized to the inclusive fiducial cross section. Points represent the unfolded data, with vertical bars showing the statistical uncertainty and a hatched band showing the sum in quadrature of the statistical and systematic uncertainties. Red and blue histograms represent the POWHEG+MCFM and MADGRAPH5_AMC@NLO+MCFM predictions, respectively, with bands around each which represent their combined statistical, scale, and PDF uncertainties. The lower sections of the plot represents the ratio of the measured cross section to each of the predictions.

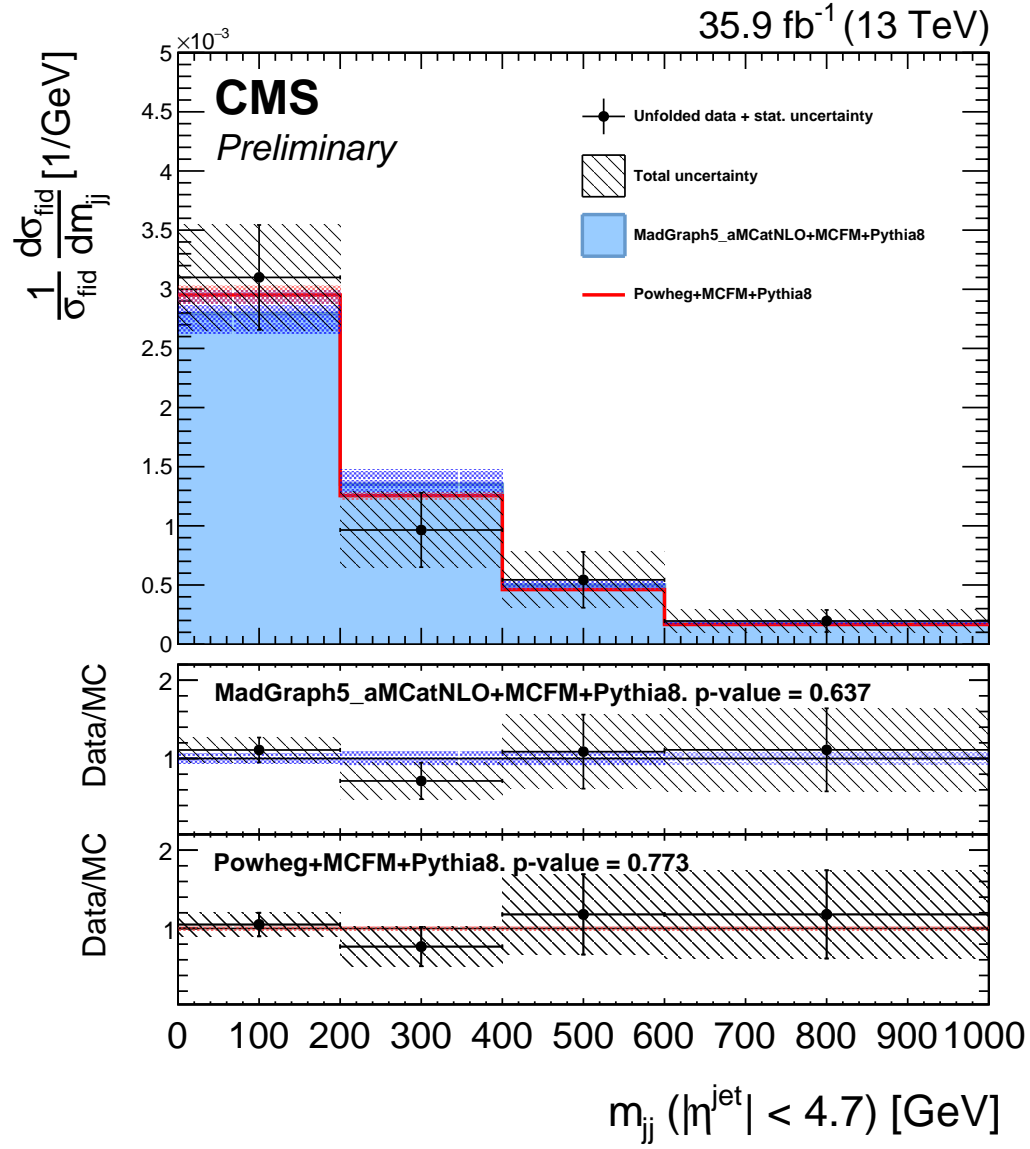


Figure 7.26: The ZZ differential cross section as a function of the invariant mass of the two highest- p_T jets m_{jj} , including all ZZ events with at least two jets, normalized to the inclusive fiducial cross section. Points represent the unfolded data, with vertical bars showing the statistical uncertainty and a hatched band showing the sum in quadrature of the statistical and systematic uncertainties. Red and blue histograms represent the POWHEG+MCFM and MADGRAPH5_AMC@NLO+MCFM predictions, respectively, with bands around each which represent their combined statistical, scale, and PDF uncertainties. The lower sections of the plot represents the ratio of the measured cross section to each of the predictions.

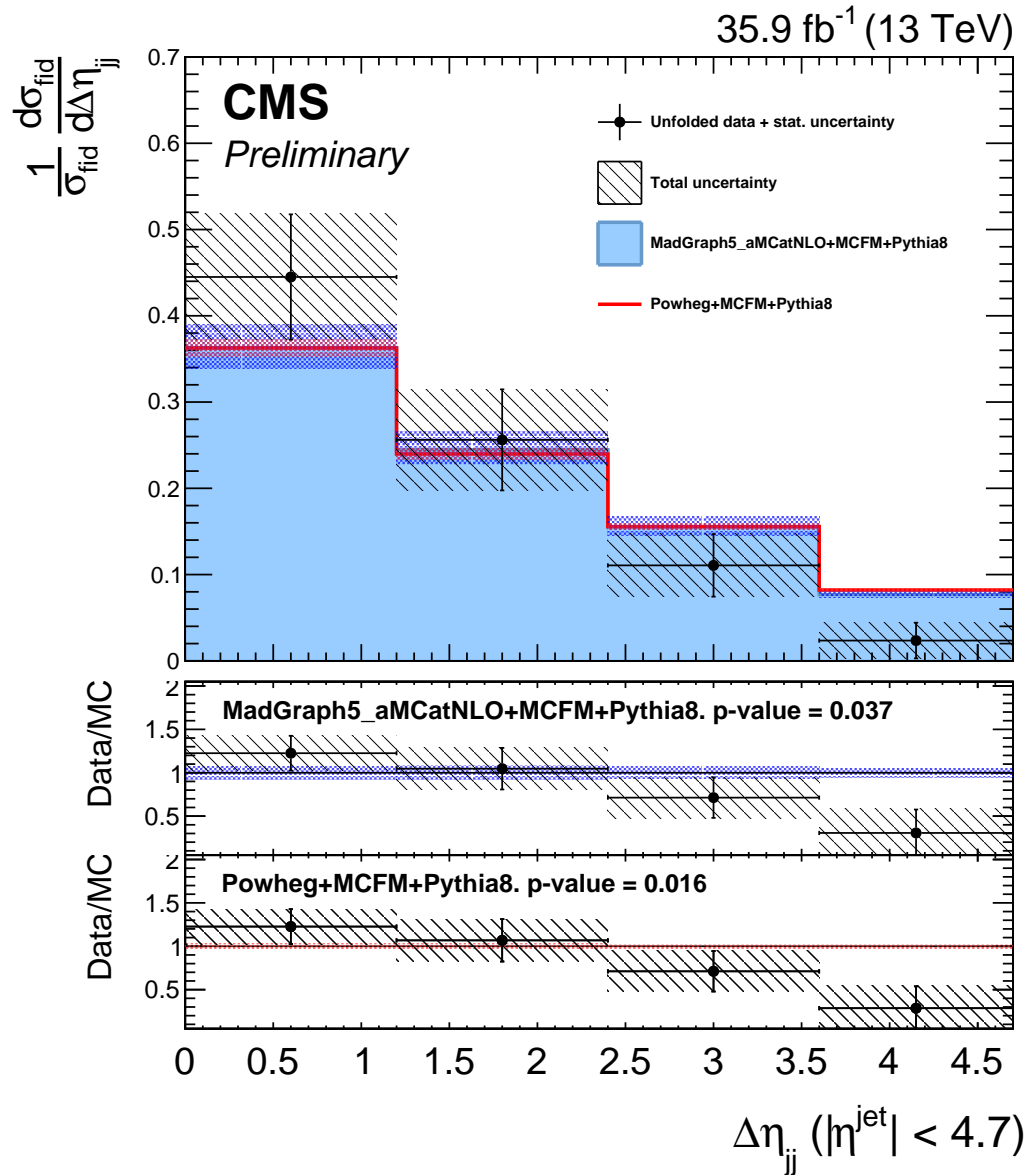


Figure 7.27: The ZZ differential cross section as a function of the absolute pseudorapidity separation of the two highest- p_T jets $|\Delta\eta_{jj}|$, including all ZZ events with at least two jets, normalized to the inclusive fiducial cross section. Points represent the unfolded data, with vertical bars showing the statistical uncertainty and a hatched band showing the sum in quadrature of the statistical and systematic uncertainties. Red and blue histograms represent the POWHEG+MCFM and MADGRAPH5_AMC@NLO+MCFM predictions, respectively, with bands around each which represent their combined statistical, scale, and PDF uncertainties. The lower sections of the plot represents the ratio of the measured cross section to each of the predictions.

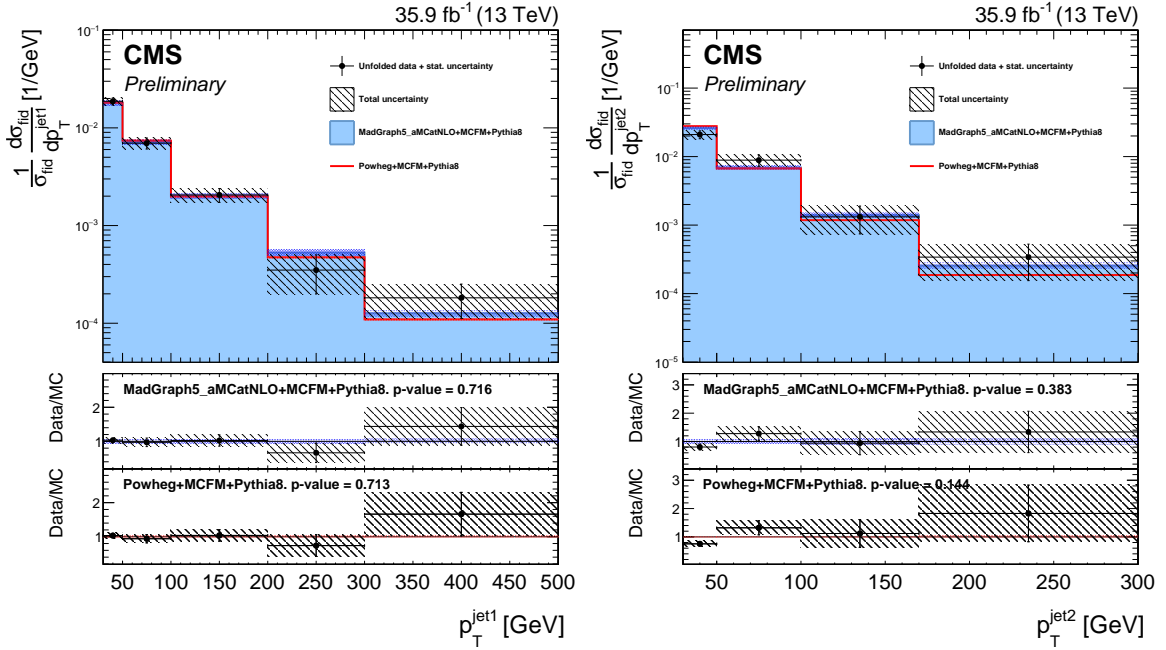


Figure 7.28: The ZZ differential cross section as a function of the leading (left) and subleading (right) jet p_T , in ZZ events with at least one jet and at least two jets respectively, normalized to the inclusive fiducial cross section. Points represent the unfolded data, with vertical bars showing the statistical uncertainty and a hatched band showing the sum in quadrature of the statistical and systematic uncertainties. Red and blue histograms represent the POWHEG+MCFM and MADGRAPH5_AMC@NLO+MCFM predictions, respectively, with bands around each which represent their combined statistical, scale, and PDF uncertainties. The lower sections of the plots represent the ratio of the measured cross section to each of the predictions.

132 No unitarizing form factor is applied when calculating the limits of Eq. (7.11). One
 133 way to enforce unitarity would be to restrict the maximum ZZ invariant mass used
 134 to set limits, which would then depend on the cutoff chosen. The limit computations
 135 are repeated with multiple cutoff values, and the resulting expected and observed
 136 limits are shown in Fig. 7.34 as a function of the maximum m_{ZZ} used.

137 The aQGC search proceeds the same way, but using events in the dijet selection.
 138 The observable used for limit setting is again m_{ZZ} , which is shown for these events
 139 along with example distributions for scenarios with nonzero aQGCs, in Fig. 7.35. In

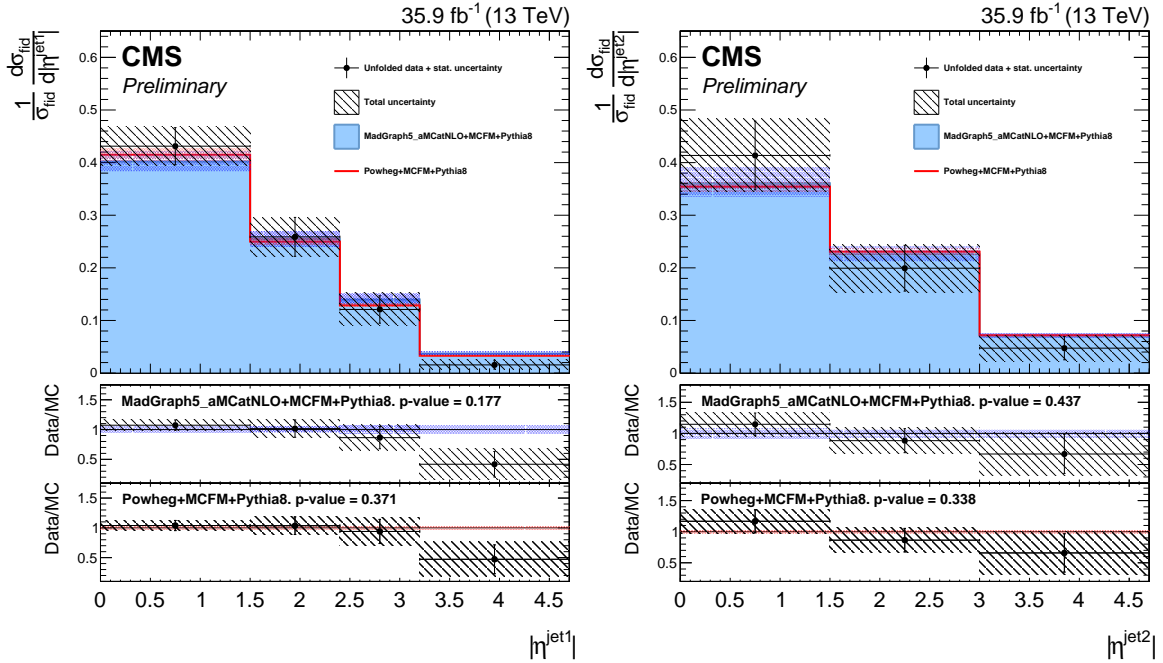


Figure 7.29: The ZZ differential cross section as a function of the leading (left) and subleading (right) jet η , in ZZ events with at least one jet and at least two jets respectively, normalized to the inclusive fiducial cross section. Points represent the unfolded data, with vertical bars showing the statistical uncertainty and a hatched band showing the sum in quadrature of the statistical and systematic uncertainties. Red and blue histograms represent the POWHEG+MCFM and MADGRAPH5_AMC@NLO+MCFM predictions, respectively, with bands around each which represent their combined statistical, scale, and PDF uncertainties. The lower sections of the plots represent the ratio of the measured cross section to each of the predictions.

140 the aQGC search, a unitarity bound is imposed, chosen with VBFNLO [184] to be the
 141 value of m_{ZZ} at which the scattering amplitude would violate unitarity if the aQGC
 142 parameter in question were set to its 95% CL limit value. While limits are set for
 143 each parameter, all other parameters and their unitarity bounds are set to zero. The

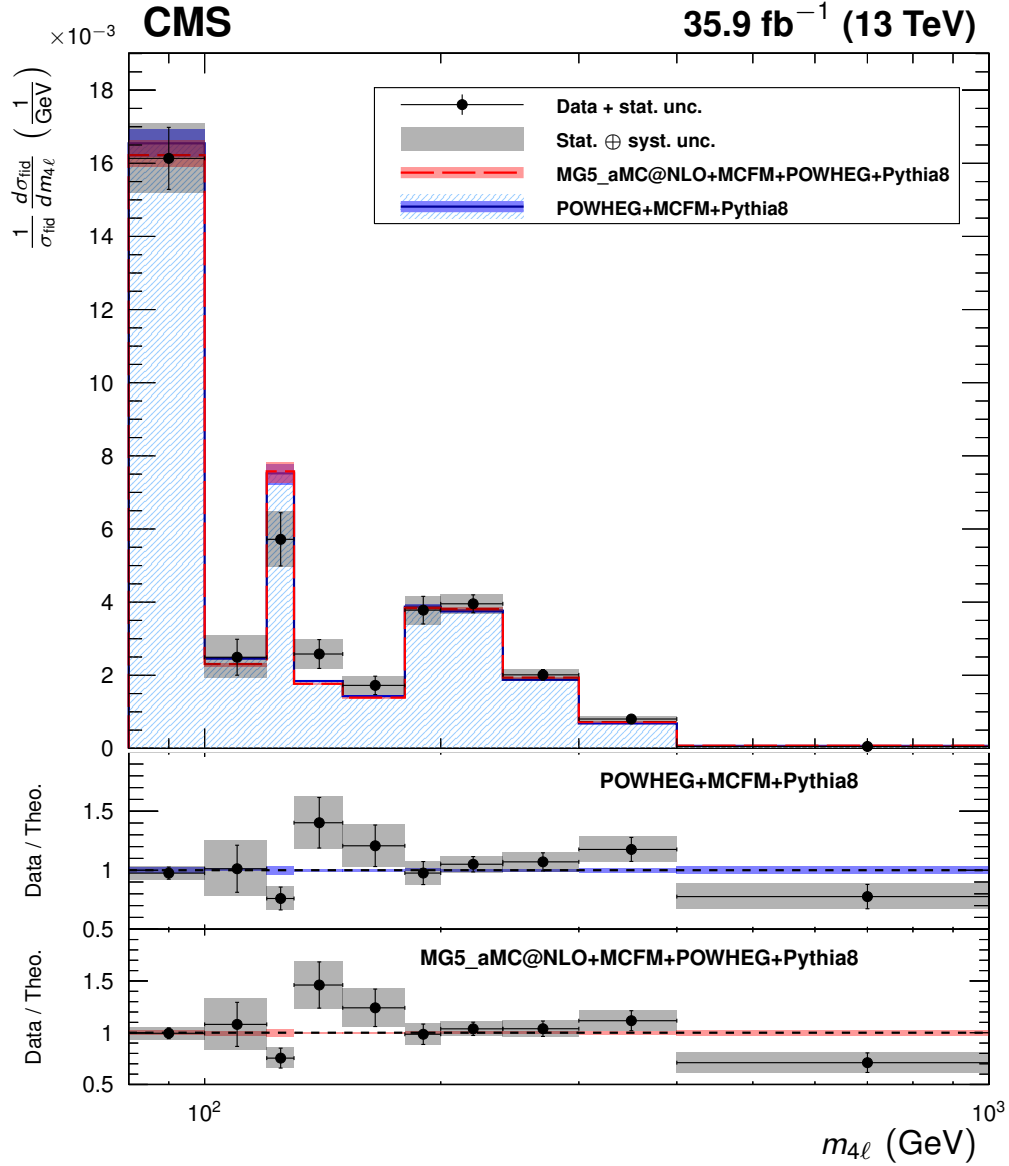


Figure 7.30: The four-lepton differential cross section as a function of $m_{4\ell}$ under the full spectrum selections, normalized to the inclusive fiducial cross section. Points represent the unfolded data, with vertical bars showing the statistical uncertainty and a grey band showing the sum in quadrature of the statistical and systematic uncertainties. Blue and red histograms represent the POWHEG+MCFM and MADGRAPH5_AMC@NLO+MCFM predictions, respectively, with bands around each which represent their combined statistical, scale, and PDF uncertainties. The lower sections of the plot represents the ratio of the measured cross section to each of the predictions.

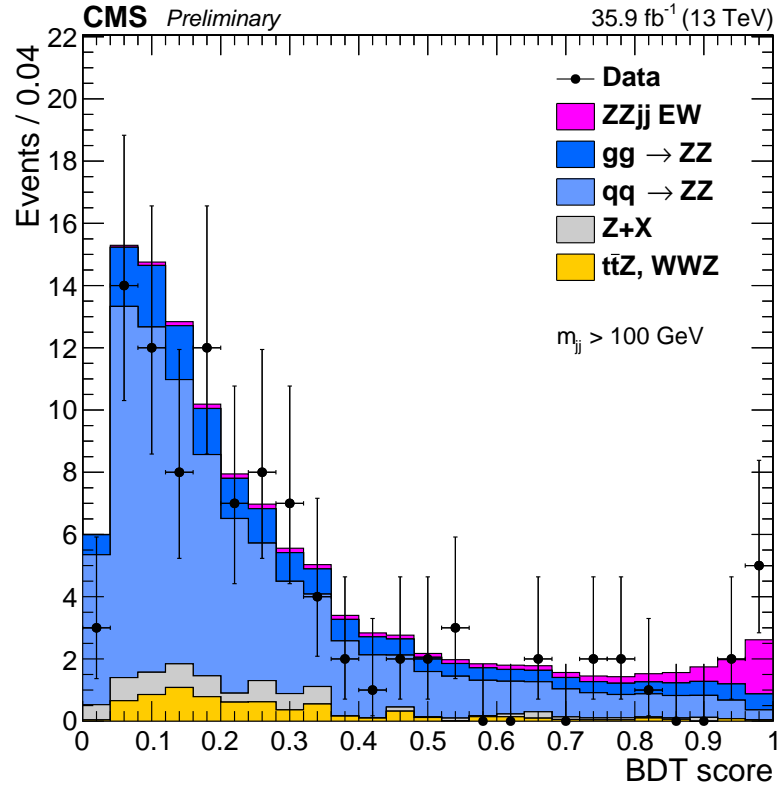


Figure 7.31: Output distribution of the VBS signal extraction GBDT, for events in the dijet selection. Points represent data, with statistical uncertainty bars. The stack of filled histograms represents the SM signal prediction and background estimate.

¹⁴⁴ observed 95% CL limits are

$$\begin{aligned}
 -0.46 &< f_{T0}/\Lambda^4 < 0.44 \text{ TeV}^{-4}, \\
 -0.61 &< f_{T1}/\Lambda^4 < 0.61 \text{ TeV}^{-4}, \\
 -1.2 &< f_{T2}/\Lambda^4 < 1.2 \text{ TeV}^{-4}, \\
 -0.84 &< f_{T8}/\Lambda^4 < 0.84 \text{ TeV}^{-4}, \\
 -1.8 &< f_{T9}/\Lambda^4 < 1.8 \text{ TeV}^{-4}.
 \end{aligned} \tag{7.12}$$

¹⁴⁵ These are the most stringent constraints to date on all five parameters.

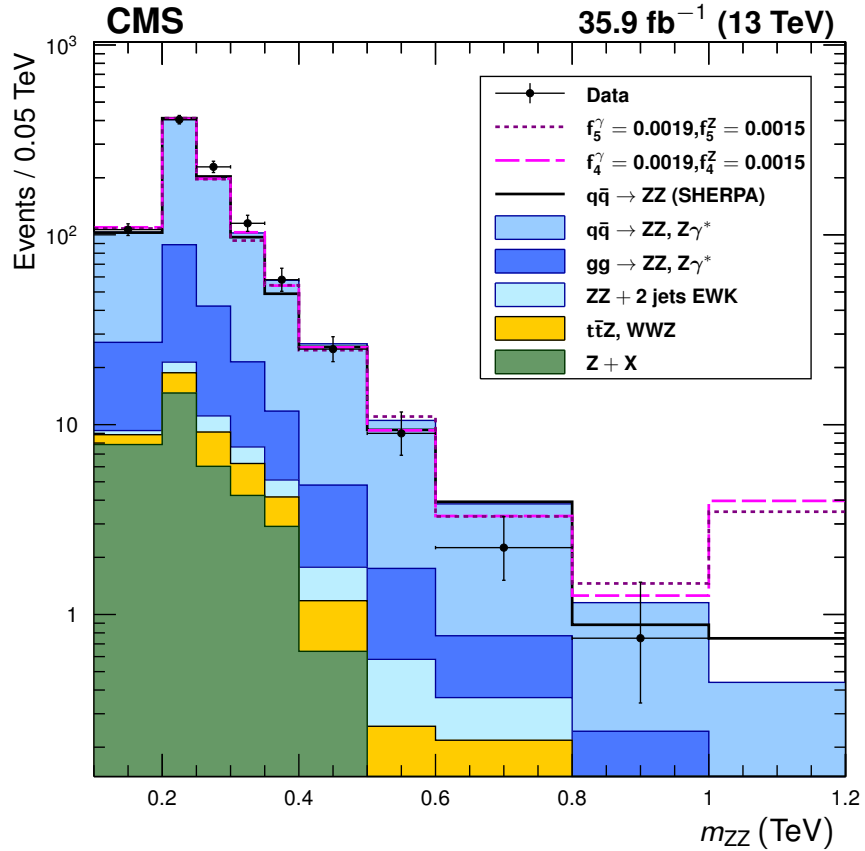


Figure 7.32: Distribution of ZZ invariant mass for all events in the on-shell selection. Points represent data, with statistical uncertainty bars. The stack of filled histograms represents the SM signal prediction and background estimate. The unfilled histograms represent two example SHERPA predictions for nonzero aTGC hypotheses (dashed) and the SHERPA SM prediction (solid), included to illustrate the shape differences between the SHERPA and POWHEG+MCFM SM predictions. The SHERPA distributions are normalized such that the SM prediction's total yield matches that of the other generators. The last bin includes the overflow contributions from events at masses above 1.2 TeV.

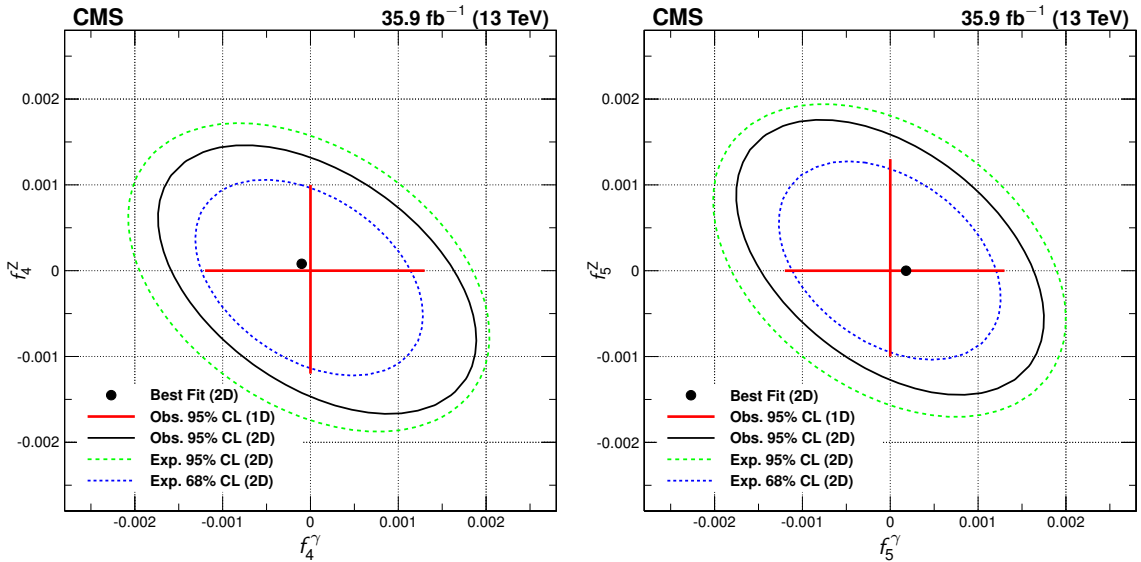


Figure 7.33: Two-dimensional observed 95% CL limits (solid contour) and expected 68 and 95% CL limits (dashed contours) in the f_4^γ - f_4^Z (left) and f_5^γ - f_5^Z (right) planes. The regions outside the contours are excluded at the corresponding confidence level. The dot is the point of maximum likelihood in the two-dimensional fits. Solid, straight lines at the center show the observed one-dimensional 95% CL limits for $f_{4,5}^\gamma$ (horizontal) and $f_{4,5}^Z$ (vertical). No form factor is used.

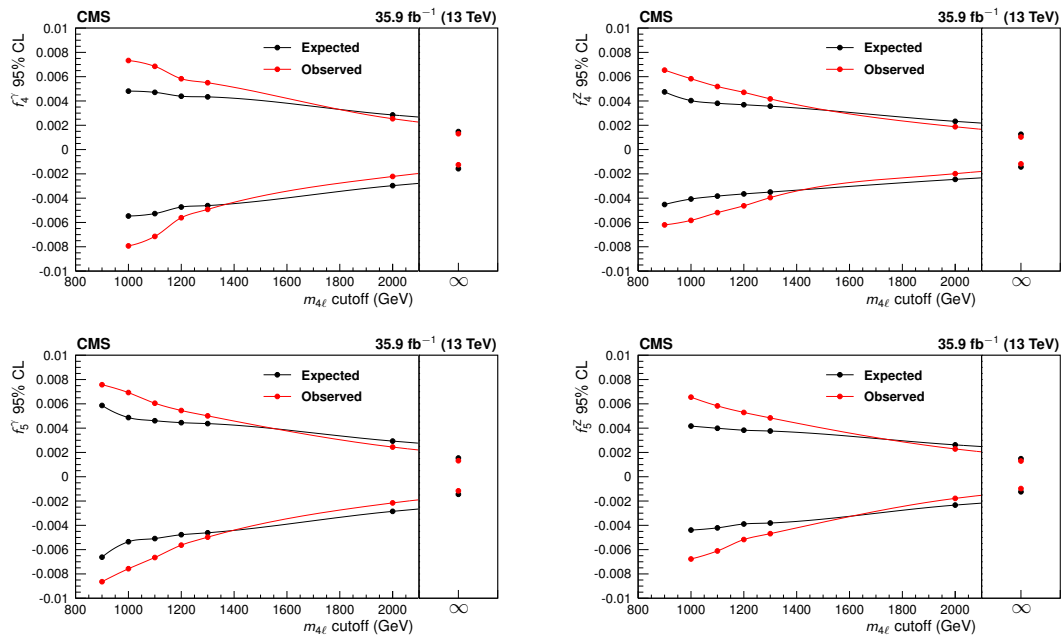


Figure 7.34: Expected and observed one-dimensional limits on the four aTGC parameters, as functions of the m_{ZZ} cutoff used to enforce unitarity. No form factor is used.

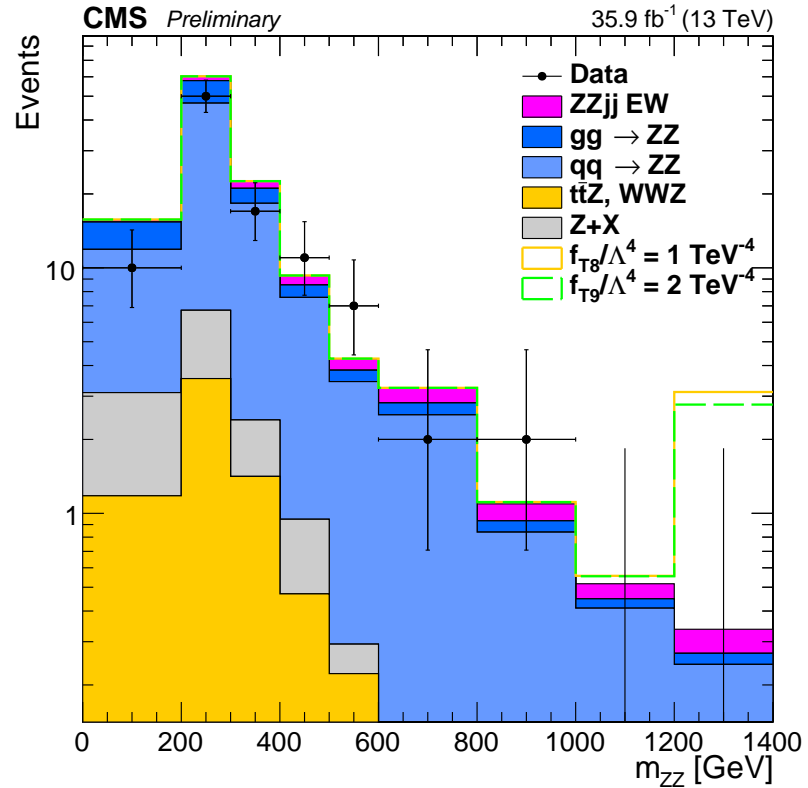


Figure 7.35: Distribution of ZZ invariant mass for events in the dijet selection. Points represent data, with statistical uncertainty bars. The stack of filled histograms represents the SM signal prediction and background estimate. The unfilled histograms represent two example MADGRAPH5_AMC@NLO distributions for nonzero aQGC hypotheses. The last bin includes the overflow contributions from events at masses above 1.4 TeV.

0 Chapter 8

1 Conclusions

2 8.1 Summary

3 8.2 Outlook

4 Bibliography

- 5 [1] D. J. Griffiths, *Introduction to elementary particles; 2nd rev. version*, ser.
6 Physics textbook. New York, NY: Wiley, 2008.
- 7 [2] F. Halzen and A. Martin, *Quarks & Leptons: An introductory course in*
8 *modern particle physics*. New York, USA: John Wiley & Sons, 1984.
- 9 [3] V. Barger and R. Phillips, *Collider Physics*, ser. Frontiers in physics. Avalon
10 Publishing, 1997, ISBN: 9780201149456.
- 11 [4] M. E. Peskin and D. V. Schroeder, *An Introduction to quantum field theory*.
12 Reading, USA: Addison-Wesley, 1995, ISBN: 9780201503975, 0201503972.
- 13 [5] J. F. Donoghue, E. Golowich, and B. R. Holstein, *Dynamics of the Standard*
14 *Model*, ser. Cambridge monographs on particle physics, nuclear physics, and
15 cosmology. Cambridge: Cambridge Univ. Press, 1992.
- 16 [6] Super-Kamiokande Collaboration, “Evidence for oscillation of atmospheric
17 neutrinos,” *Phys. Rev. Lett.*, vol. 81, pp. 1562–1567, 1998. DOI: 10.1103/
18 PhysRevLett.81.1562. arXiv: hep-ex/9807003 [hep-ex].
- 19 [7] SNO Collaboration, “Measurement of the rate of $\nu_e + d \rightarrow p + p + e^-$ interac-
20 tions produced by 8B solar neutrinos at the Sudbury Neutrino Observatory,”
21 *Phys. Rev. Lett.*, vol. 87, p. 071301, 2001. DOI: 10.1103/PhysRevLett.87.
22 071301. arXiv: nucl-ex/0106015 [nucl-ex].
- 23 [8] SNO Collaboration, “Direct evidence for neutrino flavor transformation from
24 neutral current interactions in the Sudbury Neutrino Observatory,” *Phys. Rev.*
25 *Lett.*, vol. 89, p. 011301, 2002. DOI: 10.1103/PhysRevLett.89.011301. arXiv:
26 nucl-ex/0204008 [nucl-ex].
- 27 [9] J. H. Christenson, J. W. Cronin, V. L. Fitch, and R. Turlay, “Evidence for
28 the 2π decay of the K_2^0 meson,” *Phys. Rev. Lett.*, vol. 13, p. 138, 4 Jul. 1964.
29 DOI: 10.1103/PhysRevLett.13.138.

- 30 [10] M. Kobayashi and T. Maskawa, “CP-violation in the renormalizable theory
31 of weak interaction,” *Progress of Theoretical Physics*, vol. 49, no. 2, p. 652,
32 1973. DOI: 10.1143/PTP.49.652.
- 33 [11] KTeV Collaboration, “Observation of direct CP violation in $K_{S,L} \rightarrow \pi\pi$
34 decays,” *Phys. Rev. Lett.*, vol. 83, p. 22, 1999. DOI: 10.1103/PhysRevLett.
35 83.22. arXiv: hep-ex/9905060 [hep-ex].
- 36 [12] NA48 Collaboration, “A new measurement of direct CP violation in two
37 pion decays of the neutral kaon,” *Phys. Lett. B*, vol. 465, p. 335, 1999. DOI:
38 10.1016/S0370-2693(99)01030-8. arXiv: hep-ex/9909022 [hep-ex].
- 39 [13] BaBar Collaboration, “Measurement of CP violating asymmetries in B^0
40 decays to CP eigenstates,” *Phys. Rev. Lett.*, vol. 86, p. 2515, 2001. DOI: 10.
41 1103/PhysRevLett.86.2515. arXiv: hep-ex/0102030 [hep-ex].
- 42 [14] Belle Collaboration, “Observation of large CP violation in the neutral B
43 meson system,” *Phys. Rev. Lett.*, vol. 87, p. 091802, 2001. DOI: 10.1103/
44 PhysRevLett.87.091802. arXiv: hep-ex/0107061 [hep-ex].
- 45 [15] LHCb Collaboration, “Observation of CP violation in $B^\pm \rightarrow DK^\pm$ de-
46 cays,” *Phys. Lett. B*, vol. 712, p. 203, 2012, [Corrigendum: DOI: 110.1016/j.j.
47 physletb.2012.05.060]. DOI: 10.1016/j.physletb.2012.04.060. arXiv:
48 1203.3662 [hep-ex].
- 49 [16] LHCb Collaboration, “First observation of CP violation in the decays of B_s^0
50 mesons,” *Phys. Rev. Lett.*, vol. 110, no. 22, p. 221601, 2013. DOI: 10.1103/
51 PhysRevLett.110.221601. arXiv: 1304.6173 [hep-ex].
- 52 [17] E. Noether, “Invariant variation problems,” trans. by M. A. Tavel, *Gott.
53 Nachr.*, p. 235, 1918, [*Transp. Theory Statist. Phys.*, vol. 1, p. 186, 1971]. DOI:
54 10.1080/00411457108231446. arXiv: physics/0503066 [physics].
- 55 [18] M. Srednicki, *Quantum Field Theory*. Cambridge: Cambridge Univ. Press,
56 2007.
- 57 [19] S. L. Glashow, “Partial symmetries of weak interactions,” *Nucl. Phys.*, vol.
58 22, p. 579, 1961. DOI: 10.1016/0029-5582(61)90469-2.
- 59 [20] S. Weinberg, “A model of leptons,” *Phys. Rev. Lett.*, vol. 19, p. 1264, 1967.
60 DOI: 10.1103/PhysRevLett.19.1264.

- 61 [21] A. Salam, “Weak and electromagnetic interactions,” *Conf. Proc.*, vol. C680-
62 519, p. 367, 1968.
- 63 [22] F. Englert and R. Brout, “Broken symmetry and the mass of gauge vec-
64 tor mesons,” *Phys. Rev. Lett.*, vol. 13, p. 321, 9 Aug. 1964. DOI: 10.1103/
65 PhysRevLett.13.321. [https://link.aps.org/doi/10.1103/PhysRevLett.
66 13.321](https://link.aps.org/doi/10.1103/PhysRevLett.13.321).
- 67 [23] P. W. Higgs, “Broken symmetries and the masses of gauge bosons,” *Phys.*
68 *Rev. Lett.*, vol. 13, p. 508, 16 Oct. 1964. DOI: 10.1103/PhysRevLett.13.508.
69 <https://link.aps.org/doi/10.1103/PhysRevLett.13.508>.
- 70 [24] G. S. Guralnik, C. R. Hagen, and T. W. B. Kibble, “Global conservation
71 laws and massless particles,” *Phys. Rev. Lett.*, vol. 13, p. 585, 20 Nov. 1964.
72 DOI: 10.1103/PhysRevLett.13.585. [https://link.aps.org/doi/10.1103/
73 PhysRevLett.13.585](https://link.aps.org/doi/10.1103/PhysRevLett.13.585).
- 74 [25] A. Alboteanu, W. Kilian, and J. Reuter, “Resonances and unitarity in weak
75 boson scattering at the LHC,” *JHEP*, vol. 11, p. 010, 2008. DOI: 10.1088/
76 1126-6708/2008/11/010. arXiv: 0806.4145 [hep-ph].
- 77 [26] K. Hagiwara, R. D. Peccei, D. Zeppenfeld, and K. Hikasa, “Probing the weak
78 boson sector in $e^+e^- \rightarrow W^+W^-$,” *Nucl. Phys. B*, vol. 282, p. 253, 1987. DOI:
79 10.1016/0550-3213(87)90685-7.
- 80 [27] G. J. Gounaris, J. Layssac, and F. M. Renard, “New and standard physics
81 contributions to anomalous z and γ self-couplings,” *Phys. Rev. D*, vol. 62,
82 p. 073013, 2000. DOI: 10.1103/PhysRevD.62.073013. arXiv: hep-ph/
83 0003143 [hep-ph].
- 84 [28] U. Baur and D. L. Rainwater, “Probing neutral gauge boson self-interactions
85 in zz production at hadron colliders,” *Phys. Rev. D*, vol. 62, p. 113011, 2000.
86 DOI: 10.1103/PhysRevD.62.113011. arXiv: hep-ph/0008063 [hep-ph].
- 87 [29] U. Baur and E. L. Berger, “Probing the weak boson sector in $Z\gamma$ production
88 at hadron colliders,” *Phys. Rev. D*, vol. 47, p. 4889, 1993. DOI: 10.1103/
89 PhysRevD.47.4889.
- 90 [30] C. Degrande, N. Greiner, W. Kilian, O. Mattelaer, H. Mebane, T. Stelzer,
91 S. Willenbrock, and C. Zhang, “Effective field theory: a modern approach to
92 anomalous couplings,” *Annals Phys.*, vol. 335, p. 21, 2013. DOI: 10.1016/j.
93 aop.2013.04.016. arXiv: 1205.4231 [hep-ph].

- 94 [31] O. J. P. Éboli, M. C. Gonzalez-Garcia, and J. K. Mizukoshi, “ $pp \rightarrow jje^\pm\mu^\pm\nu\nu$
 95 and $jje^\pm\mu^\mp\nu\nu$ at $\mathcal{O}(\alpha_{\text{em}}^6)$ and $\mathcal{O}(\alpha_{\text{em}}^4\alpha_s^2)$ for the study of the quartic electroweak
 96 gauge boson vertex at LHC,” *Phys. Rev. D*, vol. 74, p. 073 005, 2006. DOI:
 97 10.1103/PhysRevD.74.073005. arXiv: hep-ph/0606118 [hep-ph].
- 98 [32] NNPDF Collaboration, “Parton distributions from high-precision collider
 99 data,” 2017. arXiv: 1706.00428 [hep-ph].
- 100 [33] A. Lazopoulos, K. Melnikov, and F. Petriello, “QCD corrections to tri-boson
 101 production,” *Phys. Rev. D*, vol. 76, p. 014 001, 2007. DOI: 10.1103/PhysRevD.
 102 76.014001. arXiv: hep-ph/0703273 [hep-ph].
- 103 [34] T. Binoth, G. Ossola, C. G. Papadopoulos, and R. Pittau, “NLO QCD
 104 corrections to tri-boson production,” *JHEP*, vol. 06, p. 082, 2008. DOI: 10.
 1088/1126-6708/2008/06/082. arXiv: 0804.0350 [hep-ph].
- 106 [35] V. Hankele and D. Zeppenfeld, “QCD corrections to hadronic wwz production
 107 with leptonic decays,” *Phys. Lett. B*, vol. 661, p. 103, 2008. DOI: 10.1016/j.
 108 physletb.2008.02.014. arXiv: 0712.3544 [hep-ph].
- 109 [36] F. J. Hasert *et al.*, “Search for elastic ν_μ electron scattering,” *Phys. Lett. B*,
 110 vol. 46, p. 121, 1973. DOI: 10.1016/0370-2693(73)90494-2.
- 111 [37] UA1 Collaboration, “Experimental observation of lepton pairs of invariant
 112 mass around $95 \text{ GeV}/c^2$ at the CERN SPS collider,” *Phys. Lett. B*, vol. 126,
 113 p. 398, 1983. DOI: 10.1016/0370-2693(83)90188-0.
- 114 [38] SLD Electroweak Group, DELPHI Collaboration, ALEPH Collaboration,
 115 SLD Collaboration, SLD Heavy Flavour Group, OPAL Collaboration, LEP
 116 Electroweak Working Group, L3 Collaboration, “Precision electroweak mea-
 117 surements on the z resonance,” *Phys. Rept.*, vol. 427, p. 257, 2006. DOI: 10.
 118 1016/j.physrep.2005.12.006. arXiv: hep-ex/0509008 [hep-ex].
- 119 [39] Particle Data Group, C. Patrignani, *et al.*, “Review of particle physics,”
 120 *Chin. Phys. C*, vol. 40, no. 10, p. 100 001, 2016. DOI: 10.1088/1674-1137/
 121 40/10/100001.
- 122 [40] F. Cascioli, T. Gehrmann, M. Grazzini, S. Kallweit, P. Maierhöfer, A. von
 123 Manteuffel, S. Pozzorini, D. Rathlev, L. Tancredi, and E. Weihs, “ ZZ produc-
 124 tion at hadron colliders in NNLO QCD,” *Phys. Lett. B*, vol. 735, p. 311, 2014.
 125 DOI: 10.1016/j.physletb.2014.06.056. arXiv: 1405.2219 [hep-ph].

- 126 [41] D. Rainwater, R. Szalapski, and D. Zeppenfeld, “Probing color-singlet ex-
127 change in Z + 2-jet events at the CERN LHC,” *Phys. Rev. D*, vol. 54, p. 6680,
128 11 Dec. 1996. DOI: 10.1103/PhysRevD.54.6680.
- 129 [42] ALEPH Collaboration, “Measurement of the $e^+e^- \rightarrow ZZ$ production cross-
130 section at center-of-mass energies of 183 GeV and 189 GeV,” *Phys. Lett. B*,
131 vol. 469, p. 287, 1999. DOI: 10.1016/S0370-2693(99)01288-5. arXiv: hep-
132 ex/9911003 [hep-ex].
- 133 [43] OPAL Collaboration, “Z boson pair production in e^+e^- collisions at $\sqrt{s} =$
134 183 GeV and 189 GeV,” *Phys. Lett. B*, vol. 476, p. 256, 2000. DOI: 10.1016/
135 S0370-2693(00)00197-0. arXiv: hep-ex/0003016 [hep-ex].
- 136 [44] L3 Collaboration, “Z boson pair production at LEP,” *Phys. Lett. B*, vol.
137 572, p. 133, 2003. DOI: 10.1016/j.physletb.2003.08.023. arXiv: hep-
138 ex/0308013 [hep-ex].
- 139 [45] DELPHI Collaboration, “ZZ production in e^+e^- interactions at $\sqrt{s} = 183-$
140 209 GeV,” *Eur. Phys. J. C*, vol. 30, p. 447, 2003. DOI: 10.1140/epjc/s2003-
141 01287-0. arXiv: hep-ex/0307050 [hep-ex].
- 142 [46] OPAL Collaboration, “Study of z pair production and anomalous couplings in
143 e^+e^- collisions at \sqrt{s} between 190 GeV and 209 GeV,” *Eur. Phys. J. c*, vol. 32,
144 p. 303, 2003. DOI: 10.1140/epjc/s2003-01467-x. arXiv: hep-ex/0310013
145 [hep-ex].
- 146 [47] ALEPH Collaboration, “Measurement of z-pair production in e^+e^- collisions
147 and constraints on anomalous neutral gauge couplings,” *JHEP*, vol. 04, p. 124,
148 2009. DOI: 10.1088/1126-6708/2009/04/124.
- 149 [48] CDF Collaboration, “First measurement of zz production in $\bar{p}p$ collisions at
150 $\sqrt{s} = 1.96$ TeV,” *Phys. Rev. Lett.*, vol. 100, p. 201801, 2008. DOI: 10.1103/
151 PhysRevLett.100.201801. arXiv: 0801.4806 [hep-ex].
- 152 [49] D0 Collaboration, “ $ZZ \rightarrow \ell^+\ell^-\nu\bar{\nu}$ production in $p\bar{p}$ collisions at $\sqrt{s} =$
153 1.96 TeV,” *Phys. Rev. D*, vol. 78, p. 072002, 2008. DOI: 10.1103/PhysRevD.
154 78.072002. arXiv: 0808.0269 [hep-ex].
- 155 [50] D0 Collaboration, “Observation of zz production in $p\bar{p}$ collisions at $\sqrt{s} =$
156 1.96 TeV,” *Phys. Rev. Lett.*, vol. 101, p. 171803, 2008, DOI: 10.1103/PhysRev
157 Lett.101.171803. arXiv: 0808.0703 [hep-ex].

- 158 [51] D0 Collaboration, “Measurement of the zz production cross section in $p\bar{p}$
159 collisions at $\sqrt{s} = 1.96$ TeV,” *Phys. Rev. D*, vol. 84, p. 011103, 2011. DOI:
160 10.1103/PhysRevD.84.011103. arXiv: 1104.3078 [hep-ex].
- 161 [52] CDF Collaboration, “Measurement of zz production in leptonic final states
162 at \sqrt{s} of 1.96 TeV at CDF,” *Phys. Rev. Lett.*, vol. 108, p. 101801, 2012. DOI:
163 10.1103/PhysRevLett.108.101801. arXiv: 1112.2978 [hep-ex].
- 164 [53] J. M. Campbell and R. K. Ellis, “An update on vector boson pair production
165 at hadron colliders,” *Phys. Rev. D*, vol. 60, p. 113006, 1999. DOI: 10.1103/
166 PhysRevD.60.113006. arXiv: hep-ph/9905386 [hep-ph].
- 167 [54] CMS Collaboration, “Measurement of the zz production cross section and
168 search for anomalous couplings in $2\ell 2\ell'$ final states in pp collisions at $\sqrt{s} =$
169 7 TeV,” *JHEP*, vol. 01, p. 063, 2013. DOI: 10.1007/JHEP01(2013)063. arXiv:
170 1211.4890 [hep-ex].
- 171 [55] CMS Collaboration, “Measurement of the $pp \rightarrow ZZ$ production cross section
172 and constraints on anomalous triple gauge couplings in four-lepton final states
173 at $\sqrt{s} = 8$ TeV,” *Phys. Lett. B*, vol. 740, p. 250, 2015, [Corrigendum: DOI: 10.
174 1016/j.physletb.2016.04.010]. DOI: 10.1016/j.physletb.2014.11.059.
175 arXiv: 1406.0113 [hep-ex].
- 176 [56] CMS Collaboration, “Measurements of the zz production cross sections in the
177 $2\ell 2\nu$ channel in proton–proton collisions at $\sqrt{s} = 7$ and 8 TeV and combined
178 constraints on triple gauge couplings,” *Eur. Phys. J. C*, vol. 75, no. 10, p. 511,
179 2015. DOI: 10.1140/epjc/s10052-015-3706-0. arXiv: 1503.05467 [hep-ex].
- 180 [57] CMS Collaboration Collaboration, “Measurement of the differential cross
181 sections for pairs of z bosons produced in association with jets in pp collisions
182 at $\sqrt{s} = 8$ TeV,” CERN, Geneva, Tech. Rep. CMS-PAS-SMP-15-012, 2016.
183 <https://cds.cern.ch/record/2209215>.
- 184 [58] ATLAS Collaboration, “Measurement of zz production in pp collisions at
185 $\sqrt{s} = 7$ TeV and limits on anomalous zzz and $ZZ\gamma$ couplings with the ATLAS
186 detector,” *JHEP*, vol. 03, p. 128, 2013. DOI: 10.1007/JHEP03(2013)128.
187 arXiv: 1211.6096 [hep-ex].
- 188 [59] ATLAS Collaboration, “Measurements of four-lepton production in pp colli-
189 sions at $\sqrt{s} = 8$ TeV with the ATLAS detector,” *Phys. Lett. B*, vol. 753, p. 552,
190 2016. DOI: 10.1016/j.physletb.2015.12.048. arXiv: 1509.07844 [hep-ex].

- 191 [60] ATLAS Collaboration, “Measurement of the zz production cross section
192 in proton-proton collisions at $\sqrt{s} = 8$ TeV using the $ZZ \rightarrow \ell^-\ell^+\ell'^-\ell'^+$ and
193 $ZZ \rightarrow \ell^-\ell^+\nu\bar{\nu}$ channels with the ATLAS detector,” *JHEP*, vol. 01, p. 099,
194 2017. DOI: 10.1007/JHEP01(2017)099. arXiv: 1610.07585 [hep-ex].
- 195 [61] CMS Collaboration, “Measurement of the $pp \rightarrow ZZ$ production cross section,
196 $Z \rightarrow 4\ell$ branching fraction and constraints on anomalous triple gauge couplings
197 at $\sqrt{s} = 13$ TeV,” 2017. <https://cds.cern.ch/record/2256100>.
- 198 [62] ATLAS Collaboration, “Evidence for electroweak production of $W^\pm W^\pm jj$ in
199 pp collisions at $\sqrt{s} = 8$ TeV with the ATLAS detector,” *Phys. Rev. Lett.*, vol.
200 113, no. 14, p. 141803, 2014. DOI: 10.1103/PhysRevLett.113.141803. arXiv:
201 1405.6241 [hep-ex].
- 202 [63] CMS Collaboration, “Study of vector boson scattering and search for new
203 physics in events with two same-sign leptons and two jets,” *Phys. Rev. Lett.*,
204 vol. 114, no. 5, p. 051801, 2015. DOI: 10.1103/PhysRevLett.114.051801.
205 arXiv: 1410.6315 [hep-ex].
- 206 [64] CMS Collaboration, “Measurement of the cross section for electroweak pro-
207 duction of $Z\gamma$ in association with two jets and constraints on anomalous qua-
208 ratic gauge couplings in proton–proton collisions at $\sqrt{s} = 8$ TeV,” *Phys. Lett.*
209 *B*, vol. 770, p. 380, 2017. DOI: 10.1016/j.physletb.2017.04.071. arXiv:
210 1702.03025 [hep-ex].
- 211 [65] ATLAS Collaboration, “Studies of $Z\gamma$ production in association with a high-
212 mass dijet system in pp collisions at $\sqrt{s} = 8$ TeV with the ATLAS detector,”
213 *JHEP*, vol. 07, p. 107, 2017. DOI: 10.1007/JHEP07(2017)107. arXiv: 1705.
214 01966 [hep-ex].
- 215 [66] CMS Collaboration, “Measurement of electroweak-induced production of
216 $W\gamma$ with two jets in pp collisions at $\sqrt{s} = 8$ TeV and constraints on anomalous
217 quartic gauge couplings,” *JHEP*, vol. 06, p. 106, 2017. DOI: 10.1007/
218 JHEP06(2017)106. arXiv: 1612.09256 [hep-ex].
- 219 [67] CMS Collaboration, “Evidence for exclusive $\gamma\gamma \rightarrow W^+W^-$ production and
220 constraints on anomalous quartic gauge couplings in pp collisions at $\sqrt{s} = 7$
221 and 8 TeV,” *JHEP*, vol. 08, p. 119, 2016. DOI: 10.1007/JHEP08(2016)119.
222 arXiv: 1604.04464 [hep-ex].
- 223 [68] ATLAS Collaboration, “Measurement of exclusive $\gamma\gamma \rightarrow W^+W^-$ production
224 and search for exclusive Higgs boson production in pp collisions at $\sqrt{s} = 8$ TeV

- 225 using the ATLAS detector," *Phys. Rev. D*, vol. 94, no. 3, p. 032011, 2016. DOI:
226 10.1103/PhysRevD.94.032011. arXiv: 1607.03745 [hep-ex].
- 227 [69] CMS Collaboration Collaboration, "Observation of electroweak production
228 of same-sign w boson pairs in the two jet and two same-sign lepton final state
229 in proton-proton collisions at 13 TeV," CERN, Geneva, Tech. Rep. CMS-PAS-
230 SMP-17-004, 2017. <https://cds.cern.ch/record/2264525>.
- 231 [70] ALEPH Collaboration, "Study of the four fermion final state at the z reso-
232 nance," *Z. Phys. C*, vol. 66, p. 3, 1995. DOI: 10.1007/BF01496576.
- 233 [71] CMS Collaboration, "Observation of z decays to four leptons with the
234 CMS detector at the LHC," *JHEP*, vol. 12, p. 034, 2012. DOI: 10.1007/
235 JHEP12(2012)034. arXiv: 1210.3844 [hep-ex].
- 236 [72] ATLAS Collaboration, "Measurements of four-lepton production at the z
237 resonance in pp collisions at $\sqrt{s} = 7$ and 8 TeV with ATLAS," *Phys. Rev. Lett.*,
238 vol. 112, no. 23, p. 231806, 2014. DOI: 10.1103/PhysRevLett.112.231806.
239 arXiv: 1403.5657 [hep-ex].
- 240 [73] LHC Higgs Cross Section Working Group Collaboration, "Handbook of LHC
241 Higgs cross sections: 4. deciphering the nature of the Higgs sector," 2016. DOI:
242 10.23731/CYRM-2017-002. arXiv: 1610.07922 [hep-ph].
- 243 [74] OPAL Collaboration, DELPHI Collaboration, LEP Working Group for Higgs
244 boson searches, ALEPH Collaboration, L3 Collaboration, "Search for the stan-
245 dard model Higgs boson at LEP," *Phys. Lett. B*, vol. 565, p. 61, 2003. DOI:
246 10.1016/S0370-2693(03)00614-2. arXiv: hep-ex/0306033 [hep-ex].
- 247 [75] DELPHI Collaboration, OPAL Collaboration, ALEPH Collaboration, LEP
248 Electroweak Working Group, L3 Collaboration, "A combination of prelimi-
249 nary electroweak measurements and constraints on the standard model," 2006.
250 arXiv: hep-ex/0612034 [hep-ex].
- 251 [76] CDF Collaboration, D0 Collaboration, "Higgs boson studies at the Teva-
252 tron," *Phys. Rev. D*, vol. 88, no. 5, p. 052014, 2013. DOI: 10.1103/PhysRevD.
253 88.052014. arXiv: 1303.6346 [hep-ex].
- 254 [77] Tevatron Electroweak Working Group, CDF Collaboration, DELPHI Collab-
255 oration, SLD Electroweak and Heavy Flavour Groups, ALEPH Collaboration,
256 LEP Electroweak Working Group, SLD Collaboration, OPAL Collaboration,
257 D0 Collaboration, L3 Collaboration, "Precision electroweak measurements and
258 constraints on the standard model," 2010. arXiv: 1012.2367 [hep-ex].

- 259 [78] CMS Collaboration, “Observation of a new boson at a mass of 125 GeV with
260 the CMS experiment at the LHC,” *Phys. Lett. B*, vol. 716, p. 30, 2012. DOI:
261 10.1016/j.physletb.2012.08.021. arXiv: 1207.7235 [hep-ex].
- 262 [79] ATLAS Collaboration, “Observation of a new particle in the search for the
263 standard model Higgs boson with the ATLAS detector at the LHC,” *Phys.*
264 *Lett. B*, vol. 716, p. 1, 2012. DOI: 10.1016/j.physletb.2012.08.020. arXiv:
265 1207.7214 [hep-ex].
- 266 [80] ATLAS Collaboration, CMS Collaboration, “Combined measurement of the
267 Higgs boson mass in pp collisions at $\sqrt{s} = 7$ and 8 TeV with the ATLAS and
268 CMS experiments,” *Phys. Rev. Lett.*, vol. 114, p. 191803, 2015. DOI: 10.1103/
269 PhysRevLett.114.191803. arXiv: 1503.07589 [hep-ex].
- 270 [81] ATLAS Collaboration, CMS Collaboration, “Measurements of the Higgs
271 boson production and decay rates and constraints on its couplings from a
272 combined ATLAS and CMS analysis of the LHC pp collision data at $\sqrt{s} = 7$
273 and 8 TeV,” *JHEP*, vol. 08, p. 045, 2016. DOI: 10.1007/JHEP08(2016)045.
274 arXiv: 1606.02266 [hep-ex].
- 275 [82] I. Ots, H. Uibo, H. Liivat, R. Saar, and R. K. Loide, “Possible anomalous ZZ γ
276 and Z $\gamma\gamma$ couplings and z boson spin orientation in $e^+e^- \rightarrow Z\gamma$,” *Nucl. Phys.*,
277 vol. B702, pp. 346–356, 2004. DOI: 10.1016/j.nuclphysb.2004.09.019.
- 278 [83] DELPHI Collaboration, “Study of triple-gauge-boson couplings zzz, ZZ γ and
279 Z $\gamma\gamma$ at LEP,” *Eur. Phys. J. C*, vol. 51, p. 525, 2007. DOI: 10.1140/epjc/s10052-007-0345-0. arXiv: 0706.2741 [hep-ex].
- 281 [84] CDF Collaboration, D0 Collaboration, “Diboson physics at the Tevatron,”
282 *EPJ Web Conf.*, vol. 28, p. 06001, 2012. DOI: 10.1051/epjconf/20122806001.
283 arXiv: 1201.4771 [hep-ex].
- 284 [85] D0 Collaboration, “Search for zz and Z γ^* production in p \bar{p} collisions at
285 $\sqrt{s} = 1.96$ TeV and limits on anomalous ZZZ and ZZ γ^* couplings,” *Phys. Rev.*
286 *Lett.*, vol. 100, p. 131801, 2008. DOI: 10.1103/PhysRevLett.100.131801.
287 arXiv: 0712.0599 [hep-ex].
- 288 [86] ATLAS Collaboration, “Measurement of the zz production cross section
289 and limits on anomalous neutral triple gauge couplings in proton-proton col-
290 lisions at $\sqrt{s} = 7$ TeV with the ATLAS detector,” *Phys. Rev. Lett.*, vol. 108,
291 p. 041804, 2012. DOI: 10.1103/PhysRevLett.108.041804. arXiv: 1110.5016
292 [hep-ex].

- 293 [87] ATLAS Collaboration, “Measurement of the zz production cross section in
294 pp collisions at $\sqrt{s} = 13$ TeV with the ATLAS detector,” *Phys. Rev. Lett.*, vol.
295 116, no. 10, p. 101801, 2016. DOI: 10.1103/PhysRevLett.116.101801. arXiv:
296 1512.05314 [hep-ex].
- 297 [88] L. Evans and P. Bryant, “LHC machine,” *JINST*, vol. 3, S08001, 2008. DOI:
298 10.1088/1748-0221/3/08/S08001.
- 299 [89] O. Brüning, H. Burkhardt, and S. Myers, “The Large Hadron Collider,” *Prog.
300 Part. Nucl. Phys.*, vol. 67, no. 3, p. 7054, 2012, ISSN: 0146-6410. DOI: <https://doi.org/10.1016/j.ppnp.2012.03.001>. <http://www.sciencedirect.com/science/article/pii/S0146641012000695>.
- 303 [90] CMS Collaboration, “The CMS experiment at the CERN LHC,” *JINST*, vol.
304 3, S08004, 2008. DOI: 10.1088/1748-0221/3/08/S08004.
- 305 [91] C. Lefèvre, “The CERN accelerator complex. complexe des accélérateurs du
306 CERN,” Dec. 2008, <https://cds.cern.ch/record/1260465>.
- 307 [92] ATLAS Collaboration, “The ATLAS experiment at the CERN Large Hadron
308 Collider,” *JINST*, vol. 3, S08003, 2008. DOI: 10.1088/1748-0221/3/08/
309 S08003.
- 310 [93] LHCb Collaboration, “The LHCb detector at the LHC,” *JINST*, vol. 3,
311 S08005, 2008. DOI: 10.1088/1748-0221/3/08/S08005.
- 312 [94] ALICE Collaboration, “The ALICE experiment at the CERN LHC,” *JINST*,
313 vol. 3, S08002, 2008. DOI: 10.1088/1748-0221/3/08/S08002.
- 314 [95] TOTEM Collaboration, “The TOTEM experiment at the CERN Large
315 Hadron Collider,” *JINST*, vol. 3, S08007, 2008. DOI: 10.1088/1748-0221/3/
316 08/S08007.
- 317 [96] LHCf Collaboration, “The LHCf detector at the CERN Large Hadron Col-
318 linder,” *JINST*, vol. 3, S08006, 2008. DOI: 10.1088/1748-0221/3/08/S08006.
- 319 [97] MoEDAL Collaboration, “The physics programme of the MoEDAL exper-
320 iment at the LHC,” *Int. J. Mod. Phys.*, vol. A29, p. 1430050, 2014. DOI:
321 10.1142/S0217751X14300506. arXiv: 1405.7662 [hep-ph].
- 322 [98] M. Bajko *et al.*, “Report of the task force on the incident of 19th September
323 2008 at the LHC,” CERN, Geneva, Tech. Rep. LHC-PROJECT-Report-1168.

- 324 CERN-LHC-PROJECT-Report-1168, Mar. 2009. <http://cds.cern.ch/record/1168025>.
- 325
- 326 [99] M. Lamont, “Status of the LHC,” *Journal of Physics: Conference Series*,
327 vol. 455, no. 1, p. 012001, 2013. [http://stacks.iop.org/1742-6596/455/
328 i=1/a=012001](http://stacks.iop.org/1742-6596/455/i=1/a=012001).
- 329 [100] Y. Papaphilippou, H. Bartosik, G. Rumolo, and D. Manglunki, “Operational
330 beams for the LHC,” 2014. arXiv: [1412.7857](https://arxiv.org/abs/1412.7857) [physics.acc-ph].
- 331 [101] F. Bordry and C. Pralavorio, “LHC smashes targets for 2016 run,” Nov.
332 2016. <http://cds.cern.ch/record/2235979>.
- 333 [102] T. Sakuma and T. McCauley, “Detector and event visualization with Sketch-
334 Up at the CMS experiment,” CERN, Geneva, Tech. Rep. CMS-CR-2013-379,
335 Oct. 2013. arXiv: [1311.4942](https://arxiv.org/abs/1311.4942). <https://cds.cern.ch/record/1626816>.
- 336 [103] CMS Collaboration, “The magnet project: technical design report,” 1997.
337 <https://cds.cern.ch/record/331056>.
- 338 [104] CMS Collaboration, “The CMS tracker system project: technical design
339 report,” 1997. <http://cds.cern.ch/record/368412>.
- 340 [105] B. Isildak, “Measurement of the differential dijet production cross section
341 in proton-proton collisions at $\sqrt{s} = 7 \text{ TeV}$,” PhD thesis, Bogazici U., 2011.
342 arXiv: [1308.6064](https://arxiv.org/abs/1308.6064) [hep-ex]. [https://inspirehep.net/record/1251416/
343 files/arXiv:1308.6064.pdf](https://inspirehep.net/record/1251416/files/arXiv:1308.6064.pdf).
- 344 [106] “The CMS muon project: technical design report,” 1997. <http://cds.cern.ch/record/343814>.
- 345
- 346 [107] CMS Collaboration, “The CMS muon system in Run2: preparation, status
347 and first results,” *PoS*, vol. EPS-HEP2015, p. 237, 2015. arXiv: [1510.05424](https://arxiv.org/abs/1510.05424)
348 [physics.ins-det].
- 349 [108] CMS Collaboration, “CMS technical design report for the level-1 trigger up-
350 grade,” Tech. Rep. CERN-LHCC-2013-011. CMS-TDR-12, Jun. 2013. <https://cds.cern.ch/record/1556311>.
- 351
- 352 [109] P. R. K. Chumney, S. Dasu, J. Lackey, M. Jaworski, P. Robl, and W. H.
353 Smith, “Level-1 regional calorimeter trigger system for CMS,” *EConf*, vol.
354 C0303241, THHT003, 2003. arXiv: [hep-ex/0305047](https://arxiv.org/abs/hep-ex/0305047) [hep-ex].

- 355 [110] B. Kreis and others, “Run 2 upgrades to the CMS level-1 calorimeter trigger,”
356 *JINST*, vol. 11, no. 01, p. C01051, 2016. DOI: 10.1088/1748-0221/11/01/
357 C01051. arXiv: 1511.05855 [physics.ins-det].
- 358 [111] A. Svetek, M. Blake, M. Cepeda Hermida, S. Dasu, L. Dodd, R. Fobes, B.
359 Gomber, T. Gorski, Z. Guo, P. Klabbers, A. Levine, I. Ojalvo, T. Ruggles, N.
360 Smith, W. Smith, J. Tikalsky, M. Vicente, and N. Woods, “The calorimeter
361 trigger processor card: the next generation of high speed algorithmic data
362 processing at CMS,” *JINST*, vol. 11, p. C02011, 2016. DOI: 10.1088/1748-
363 0221/11/02/C02011.
- 364 [112] J. Ero *et al.*, “The CMS drift tube trigger track finder,” *JINST*, vol. 3,
365 P08006, 2008. DOI: 10.1088/1748-0221/3/08/P08006.
- 366 [113] D. Acosta, A. Atamanchuk, V. Golovtsov, A. Madorsky, B. Razmyslovich,
367 B. Scurlock, and S. Wang, “The track-finding processor for the level-1 trigger
368 of the CMS endcap muon system,” 1999.
- 369 [114] J. Ero *et al.*, “The CMS level-1 trigger barrel track finder,” *JINST*, vol. 11,
370 no. 03, p. C03038, 2016. DOI: 10.1088/1748-0221/11/03/C03038.
- 371 [115] W. M. Zabolotny and A. Byszuk, “Algorithm and implementation of muon
372 trigger and data transmission system for barrel-endcap overlap region of the
373 CMS detector,” *JINST*, vol. 11, no. 03, p. C03004, 2016. DOI: 10.1088/1748-
374 0221/11/03/C03004.
- 375 [116] H. Sakulin and A. Taurok, “The level-1 global muon trigger for the CMS ex-
376 periment,” CERN, Geneva, Tech. Rep. CMS-CR-2003-040, Oct. 2003. <https://cds.cern.ch/record/687846>.
- 377 [117] M. Jeitler, J. Lingemann, D. Rabady, H. Sakulin, and A. Stahl, “Upgrade
378 of the CMS global muon trigger,” *IEEE Trans. Nucl. Sci.*, vol. 62, no. 3,
379 pp. 1104–1109, 2015. DOI: 10.1109/TNS.2015.2435060.
- 381 [118] M. Jeitler *et al.*, “The level-1 global trigger for the CMS experiment at LHC,”
382 *JINST*, vol. 2, P01006, 2007. DOI: 10.1088/1748-0221/2/01/P01006.
- 383 [119] J. Wittmann, B. Arnold, H. Bergauer, M. Jeitler, T. Matsushita, D. Rabady,
384 B. Rahbaran, and C.-E. Wulz, “The upgrade of the CMS global trigger,”
385 *JINST*, vol. 11, no. 02, p. C02029, 2016. <http://stacks.iop.org/1748-0221/11/i=02/a=C02029>.

- 387 [120] CMS Collaboration, “The CMS high level trigger,” *Eur. Phys. J. C*, vol. 46,
388 p. 605, 2006. DOI: 10.1140/epjc/s2006-02495-8. arXiv: hep-ex/0512077
389 [hep-ex].
- 390 [121] S. Van der Meer, “Calibration of the effective beam height in the ISR,” 1968.
- 391 [122] CMS Collaboration, “Beams scan based absolute normalization of the CMS
392 luminosity measurement. CMS 2010 luminosity determination,” 2011. <https://cds.cern.ch/record/1357856>.
- 394 [123] CMS Collaboration, “CMS luminosity measurement for the 2015 data-taking
395 period,” CERN, Geneva, Tech. Rep. CMS-PAS-LUM-15-001, 2017. <http://cds.cern.ch/record/2138682>.
- 397 [124] CMS Collaboration Collaboration, “CMS luminosity measurements for the
398 2016 data taking period,” CERN, Geneva, Tech. Rep. CMS-PAS-LUM-17-001,
399 2017. <http://cds.cern.ch/record/2257069>.
- 400 [125] N. Metropolis and S. Ulam, “The Monte Carlo method,” *Journal of the
401 American Statistical Association*, vol. 44, p. 335, 1949. DOI: 10.2307/2280232.
402 <http://www.jstor.org/stable/2280232>.
- 403 [126] M. Matsumoto and T. Nishimura, “Mersenne Twister: A 623-dimensionally
404 equidistributed uniform pseudo-random number generator,” *ACM Trans.
405 Model. Comput. Simul.*, vol. 8, p. 3, 1998. DOI: 10.1145/272991.272995.
406 <http://doi.acm.org/10.1145/272991.272995>.
- 407 [127] J. Alwall, R. Frederix, S. Frixione, V. Hirschi, F. Maltoni, O. Mattelaer,
408 H.-S. Shao, T. Stelzer, P. Torrielli, and M. Zaro, “The automated computation
409 of tree-level and next-to-leading order differential cross sections, and their
410 matching to parton shower simulations,” *JHEP*, vol. 07, p. 079, 2014. DOI:
411 10.1007/JHEP07(2014)079. arXiv: 1405.0301 [hep-ph].
- 412 [128] P. Nason, “A new method for combining NLO QCD with shower monte carlo
413 algorithms,” *JHEP*, vol. 11, p. 040, 2004. DOI: 10.1088/1126-6708/2004/
414 11/040. arXiv: hep-ph/0409146 [hep-ph].
- 415 [129] S. Frixione, P. Nason, and C. Oleari, “Matching NLO QCD computations
416 with parton shower simulations: the POWHEG method,” *JHEP*, vol. 11, p. 070,
417 2007. DOI: 10.1088/1126-6708/2007/11/070. arXiv: 0709.2092 [hep-ph].
- 418 [130] S. Alioli, P. Nason, C. Oleari, and E. Re, “A general framework for im-
419 plementing NLO calculations in shower Monte Carlo programs: the POWHEG

- 420 BOX,” *JHEP*, vol. 06, p. 043, 2010. DOI: [10.1007/JHEP06\(2010\)043](https://doi.org/10.1007/JHEP06(2010)043). arXiv: 1002.2581 [hep-ph].
- 421
- 422 [131] T. Gleisberg, S. Hoeche, F. Krauss, M. Schonherr, S. Schumann, F. Siegert, and J. Winter, “Event generation with SHERPA 1.1,” *JHEP*, vol. 02, p. 007, 2009. DOI: [10.1088/1126-6708/2009/02/007](https://doi.org/10.1088/1126-6708/2009/02/007). arXiv: 0811.4622 [hep-ph].
- 423
- 424
- 425 [132] J. M. Campbell, R. K. Ellis, and C. Williams, “Vector boson pair production at the LHC,” *JHEP*, vol. 07, p. 018, 2011. DOI: [10.1007/JHEP07\(2011\)018](https://doi.org/10.1007/JHEP07(2011)018). arXiv: 1105.0020 [hep-ph].
- 426
- 427
- 428 [133] J. M. Campbell, R. K. Ellis, and W. T. Giele, “A multi-threaded version of MCFM,” *Eur. Phys. J. C*, vol. 75, p. 246, 2015. DOI: [10.1140/epjc/s10052-015-3461-2](https://doi.org/10.1140/epjc/s10052-015-3461-2). arXiv: 1503.06182 [physics.comp-ph].
- 429
- 430
- 431 [134] R. Boughezal, J. M. Campbell, R. K. Ellis, C. Focke, W. Giele, X. Liu, F. Petriello, and C. Williams, “Color singlet production at NNLO in MCFM,” *Eur. Phys. J. C*, vol. 77, p. 7, 2017. DOI: [10.1140/epjc/s10052-016-4558-y](https://doi.org/10.1140/epjc/s10052-016-4558-y). arXiv: 1605.08011 [hep-ph].
- 432
- 433
- 434
- 435 [135] G. P. Lepage, “A new algorithm for adaptive multidimensional integration,” *J. Comput. Phys.*, vol. 27, p. 192, 1978. DOI: [10.1016/0021-9991\(78\)90004-9](https://doi.org/10.1016/0021-9991(78)90004-9).
- 436
- 437
- 438 [136] R. Frühwirth, “Application of Kalman filtering to track and vertex fitting,” *Nucl. Instrum. Meth. A*, vol. 262, p. 444, 1987. DOI: [10.1016/0168-9002\(87\)90887-4](https://doi.org/10.1016/0168-9002(87)90887-4).
- 439
- 440
- 441 [137] P. Billoir and S. Qian, “Simultaneous pattern recognition and track fitting by the Kalman filtering method,” *Nucl. Instrum. Meth. A*, vol. 294, p. 219, 1990. DOI: [10.1016/0168-9002\(90\)91835-Y](https://doi.org/10.1016/0168-9002(90)91835-Y).
- 442
- 443
- 444 [138] W. Adam, B. Mangano, T. Speer, and T. Todorov, “Track reconstruction in the CMS tracker,” 2005.
- 445
- 446 [139] CMS Collaboration, “Description and performance of track and primary-vertex reconstruction with the CMS tracker,” *JINST*, vol. 9, no. 10, P10009, 2014. DOI: [10.1088/1748-0221/9/10/P10009](https://doi.org/10.1088/1748-0221/9/10/P10009). arXiv: 1405.6569 [physics.ins-det].
- 447
- 448
- 449
- 450 [140] W. Adam, R. Frühwirth, A. Strandlie, and T. Todor, “Reconstruction of electrons with the Gaussian-sum filter in the CMS tracker at the LHC,” 2005.
- 451

- 452 [141] T. Speer, K. Prokofiev, R. Fruhwirth, W. Waltenberger, and P. Vanlaer,
453 “Vertex fitting in the CMS tracker,” 2006.
- 454 [142] K. Rose, “Deterministic annealing for clustering, compression, classification,
455 regression, and related optimization problems,” *Proceedings of the IEEE*, vol.
456 86, no. 11, p. 2210, Nov. 1998, ISSN: 0018-9219. DOI: 10.1109/5.726788.
- 457 [143] CMS Collaboration, “Commissioning of the particle-flow event reconstruction
458 with the first LHC collisions recorded in the CMS detector,” Tech. Rep. CMS-
459 PAS-PFT-10-001, 2010. <https://cds.cern.ch/record/1247373>.
- 460 [144] CMS Collaboration, “Particle-flow reconstruction and global event descrip-
461 tion with the CMS detector,” 2017. arXiv: 1706.04965 [physics.ins-det].
- 462 [145] CMS Collaboration, “Performance of CMS muon reconstruction in pp colli-
463 sion events at $\sqrt{s} = 7 \text{ TeV}$,” *JINST*, vol. 7, P10002, 2012. DOI: 10.1088/1748-
464 0221/7/10/P10002. arXiv: 1206.4071 [physics.ins-det].
- 465 [146] S. Baffioni, C. Charlot, F. Ferri, D. Futyan, P. Meridiani, I. Puljak, C. Rovelli,
466 R. Salerno, and Y. Sirois, “Electron reconstruction in CMS,” *Eur. Phys. J. C*,
467 vol. 49, p. 1099, 2007. DOI: 10.1140/epjc/s10052-006-0175-5.
- 468 [147] CMS Collaboration, “Performance of photon reconstruction and identifi-
469 cation with the CMS detector in proton-proton collisions at $\sqrt{s} = 8 \text{ TeV}$,”
470 *JINST*, vol. 10, no. 08, P08010, 2015. DOI: 10.1088/1748-0221/10/08/
471 P08010. arXiv: 1502.02702 [physics.ins-det].
- 472 [148] G. P. Salam and G. Soyez, “A practical seedless infrared-safe cone jet algo-
473 rithm,” *JHEP*, vol. 05, p. 086, 2007. DOI: 10.1088/1126-6708/2007/05/086.
474 arXiv: 0704.0292 [hep-ph].
- 475 [149] G. P. Salam, “Towards jetography,” *Eur. Phys. J. C*, vol. 67, p. 637, 2010.
476 DOI: 10.1140/epjc/s10052-010-1314-6. arXiv: 0906.1833 [hep-ph].
- 477 [150] M. Cacciari, G. P. Salam, and G. Soyez, “The anti- k_T jet clustering algo-
478 rithm,” *JHEP*, vol. 04, p. 063, 2008. DOI: 10.1088/1126-6708/2008/04/063.
479 arXiv: 0802.1189 [hep-ph].
- 480 [151] M. Cacciari, G. P. Salam, and G. Soyez, “FastJet user manual,” *Eur. Phys.
481 J. C*, vol. 72, p. 1896, 2012. DOI: 10.1140/epjc/s10052-012-1896-2. arXiv:
482 1111.6097 [hep-ph].
- 483 [152] CMS Collaboration, “Study of pileup removal algorithms for jets,” 2014.

- 484 [153] CMS Collaboration, “Jet energy scale and resolution in the CMS experiment
485 in pp collisions at 8 TeV,” *JINST*, vol. 12, no. 02, P02014, 2017. DOI: 10.1088/
486 1748-0221/12/02/P02014. arXiv: 1607.03663 [hep-ex].
- 487 [154] M. Cacciari, G. P. Salam, and G. Soyez, “The catchment area of jets,”
488 *JHEP*, vol. 04, p. 005, 2008. DOI: 10.1088/1126-6708/2008/04/005. arXiv:
489 0802.1188 [hep-ph].
- 490 [155] M. Cacciari and G. P. Salam, “Pileup subtraction using jet areas,” *Phys.*
491 *Lett. B*, vol. 659, p. 119, 2008. DOI: 10.1016/j.physletb.2007.09.077.
492 arXiv: 0707.1378 [hep-ph].
- 493 [156] CMS Collaboration, “Determination of jet energy calibration and transverse
494 momentum resolution in CMS,” *JINST*, vol. 6, P11002, 2011. DOI: 10.1088/
495 1748-0221/6/11/P11002. arXiv: 1107.4277 [physics.ins-det].
- 496 [157] CMS Collaboration, “Missing transverse energy performance of the CMS
497 detector,” *JINST*, vol. 6, P09001, 2011. DOI: 10.1088/1748-0221/6/09/
498 P09001. arXiv: 1106.5048 [physics.ins-det].
- 499 [158] CMS Collaboration, “Performance of the CMS missing transverse momen-
500 tum reconstruction in pp data at $\sqrt{s} = 8\text{TeV}$,” *JINST*, vol. 10, no. 02,
501 P02006, 2015. DOI: 10.1088/1748-0221/10/02/P02006. arXiv: 1411.0511
502 [physics.ins-det].
- 503 [159] CMS Collaboration, “Performance of missing energy reconstruction in 13 TeV
504 pp collision data using the CMS detector,” CERN, Geneva, Tech. Rep. CMS-
505 PAS-JME-16-004, 2016. <http://cds.cern.ch/record/2205284>.
- 506 [160] CMS Collaboration, “Electron reconstruction and identification at $\sqrt{s} =$
507 7 TeV,” CERN, Geneva, Tech. Rep. CMS-PAS-EGM-10-004, 2010. <https://cds.cern.ch/record/1299116>.
- 509 [161] CMS Collaboration, “Performance of electron reconstruction and selection
510 with the CMS detector in proton-proton collisions at $\sqrt{s} = 8\text{TeV}$,” *JINST*,
511 vol. 10, no. 06, P06005, 2015. DOI: 10.1088/1748-0221/10/06/P06005.
512 arXiv: 1502.02701 [physics.ins-det].
- 513 [162] CMS Collaboration, “Measurement of the inclusive w and z production cross
514 sections in pp collisions at $\sqrt{s} = 7\text{TeV}$,” *JHEP*, vol. 10, p. 132, 2011. DOI:
515 10.1007/JHEP10(2011)132. arXiv: 1107.4789 [hep-ex].

- 516 [163] CMS Collaboration, “Measurement of the properties of a Higgs boson in the
517 four-lepton final state,” *Phys. Rev. D*, vol. 89, no. 9, p. 092007, 2014. DOI:
518 10.1103/PhysRevD.89.092007. arXiv: 1312.5353 [hep-ex].
- 519 [164] J. Butterworth *et al.*, “PDF4LHC recommendations for LHC Run II,” *J.
520 Phys. G*, vol. 43, p. 023001, 2016. DOI: 10.1088/0954-3899/43/2/023001.
521 arXiv: 1510.03865 [hep-ph].
- 522 [165] G. Bohm and G. Zech, *Introduction to statistics and data analysis for physi-
523 cists*. DESY, 2010, ISBN: 9783935702416. <https://books.google.ch/books?id=aQBHcgAACAAJ>.
- 525 [166] G. D’Agostini, “A multidimensional unfolding method based on Bayes’ the-
526 oreom,” *Nucl. Instrum. Meth. A*, vol. 362, p. 487, 1995. DOI: 10.1016/0168-
527 9002(95)00274-X.
- 528 [167] A. P. Dempster, N. M. Laird, and D. B. Rubin, “Maximum likelihood from
529 incomplete data via the EM algorithm,” *J. R. Stat. Soc. B*, vol. 39, p. 1, 1977,
530 ISSN: 00359246. <http://www.jstor.org/stable/2984875>.
- 531 [168] L. B. Lucy, “An iterative technique for the rectification of observed distri-
532 butions,” *Astron. J.*, vol. 79, p. 745, Jun. 1974. DOI: 10.1086/111605.
- 533 [169] W. H. Richardson, “Bayesian-based iterative method of image restoration,”
534 *J. Opt. Soc. Am.*, vol. 62, p. 55, Jan. 1972. DOI: 10.1364/JOSA.62.000055.
535 <http://www.osapublishing.org/abstract.cfm?URI=josa-62-1-55>.
- 536 [170] L. A. Shepp and Y. Vardi, “Maximum likelihood reconstruction for emission
537 tomography,” *IEEE Transactions on Medical Imaging*, vol. 1, no. 2, p. 113,
538 Oct. 1982, ISSN: 0278-0062. DOI: 10.1109/TMI.1982.4307558.
- 539 [171] T. Adye, “Unfolding algorithms and tests using RooUnfold,” in *Proceedings,
540 PHYSTAT 2011 Workshop on Statistical Issues Related to Discovery Claims
541 in Search Experiments and Unfolding*, CERN, Geneva, Switzerland 17–20 Jan-
542 uary 2011, CERN, Geneva: CERN, 2011, p. 313. DOI: 10.5170/CERN-2011-
543 006.313. arXiv: 1105.1160 [physics.data-an]. <https://inspirehep.net/record/898599/files/arXiv:1105.1160.pdf>.
- 545 [172] Y. Vardi, “Empirical distributions in selection bias models,” *Ann. Statist.*,
546 vol. 13, p. 178, Mar. 1985. DOI: 10.1214/aos/1176346585. <http://dx.doi.org/10.1214/aos/1176346585>.

- 548 [173] F. Pedregosa, G. Varoquaux, A. Gramfort, V. Michel, B. Thirion, O. Grisel,
549 M. Blondel, P. Prettenhofer, R. Weiss, V. Dubourg, J. Vanderplas, A. Pas-
550 sos, D. Cournapeau, M. Brucher, M. Perrot, and E. Duchesnay, “Scikit-learn:
551 Machine learning in Python,” *J. Mach. Learn. Res.*, vol. 12, p. 2825, 2011.
- 552 [174] CMS Collaboration Collaboration, “Performance of quark/gluon discrimina-
553 tion in 8 TeV pp data,” CERN, Geneva, Tech. Rep. CMS-PAS-JME-13-002,
554 2013. <https://cds.cern.ch/record/1599732>.
- 555 [175] G. Cowan, K. Cranmer, E. Gross, and O. Vitells, “Asymptotic formulae for
556 likelihood-based tests of new physics,” *Eur. Phys. J. C*, vol. 71, p. 1554, 2011,
557 [Erratum: DOI: 10.1140/epjc/s10052-013-2501-z]. DOI: 10.1140/epjc/
558 s10052-011-1554-0. arXiv: 1007.1727 [physics.data-an].
- 559 [176] CMS Collaboration and ATLAS Collaboration, “Combination of results from
560 the ATLAS and CMS experiments on anomalous triple gauge couplings in zz
561 production from pp collisions at a centre-of-mass energy of 7 TeV at the LHC,”
562 CERN, Geneva, Tech. Rep. CMS-PAS-SMP-15-001. ATLAS-CONF-2016-036,
563 2016. <https://cds.cern.ch/record/2202807>.
- 564 [177] CMS Collaboration, “Measurement of the zz production cross section in
565 $\ell\ell\ell'\ell'$ decays in pp collisions at $\sqrt{s} = 13$ TeV,” 2015. [https://cds.cern.ch/](https://cds.cern.ch/record/2114822)
566 record/2114822.
- 567 [178] CMS Collaboration, “Measurement of the zz production cross section and
568 $Z \rightarrow \ell^+\ell^-\ell'^+\ell'^-$ branching fraction in pp collisions at $\sqrt{s} = 13$ TeV,” *Phys.*
569 *Lett. B*, vol. 763, p. 280, 2016. DOI: 10.1016/j.physletb.2016.10.054.
570 arXiv: 1607.08834 [hep-ex].
- 571 [179] CMS Collaboration, “Measurements of differential cross sections and search
572 for the electroweak production of two z bosons produced in association with
573 jets,” 2017. <https://cds.cern.ch/record/2264556>.
- 574 [180] CMS Collaboration, “Studies of Higgs boson production in the four-lepton
575 final state at $\sqrt{s} = 13$ TeV,” 2016. <https://cds.cern.ch/record/2139978>.
- 576 [181] CMS Collaboration, “Measurements of properties of the Higgs boson and
577 search for an additional resonance in the four-lepton final state at $\sqrt{s} =$
578 13 TeV,” 2016. <https://cds.cern.ch/record/2204926>.
- 579 [182] CMS Collaboration, “Measurements of properties of the Higgs boson decaying
580 into the four-lepton final state in pp collisions at $\sqrt{s} = 13$ TeV,” 2017. arXiv:
581 1706.09936 [hep-ex].

- 582 [183] R. Gavin, Y. Li, F. Petriello, and S. Quackenbush, “FEWZ 2.0: a code
583 for hadronic z production at next-to-next-to-leading order,” *Comput. Phys.*
584 *Commun.*, vol. 182, p. 2388, 2011. DOI: 10.1016/j.cpc.2011.06.008. arXiv:
585 1011.3540 [hep-ph].
- 586 [184] K. Arnold *et al.*, “VBFNLO: a parton level Monte Carlo for processes with
587 electroweak bosons,” *Comput. Phys. Commun.*, vol. 180, pp. 1661–1670, 2009.
588 DOI: 10.1016/j.cpc.2009.03.006. arXiv: 0811.4559 [hep-ph].